



저작자표시-비영리-변경금지 2.0 대한민국

이용자는 아래의 조건을 따르는 경우에 한하여 자유롭게

- 이 저작물을 복제, 배포, 전송, 전시, 공연 및 방송할 수 있습니다.

다음과 같은 조건을 따라야 합니다:



저작자표시. 귀하는 원저작자를 표시하여야 합니다.



비영리. 귀하는 이 저작물을 영리 목적으로 이용할 수 없습니다.



변경금지. 귀하는 이 저작물을 개작, 변형 또는 가공할 수 없습니다.

- 귀하는, 이 저작물의 재이용이나 배포의 경우, 이 저작물에 적용된 이용허락조건을 명확하게 나타내어야 합니다.
- 저작권자로부터 별도의 허가를 받으면 이러한 조건들은 적용되지 않습니다.

저작권법에 따른 이용자의 권리는 위의 내용에 의하여 영향을 받지 않습니다.

이것은 [이용허락규약\(Legal Code\)](#)을 이해하기 쉽게 요약한 것입니다.

[Disclaimer](#)

Dissertation for Doctoral Degree of Engineering

Advanced Electro-Optic and Biomimetic
Devices Based on Functional Polymers

기능성 고분자 기반 차세대 전기광학 소자
및 생체모방 응용에 관한 연구

by

Jun-Hee Na

August 2012

Department of Electrical Engineering and Computer Science
College of Engineering
Seoul National University

Advanced Electro-Optic and Biomimetic
Devices Based on Functional Polymers

기능성 고분자 기반 차세대 전기광학 소자
및 생체모방 응용에 관한 연구

지도교수 이신두

이 본문을 공학박사 학위논문으로 제출함

2012년 6월

서울대학교 대학원

전기 컴퓨터 공학부

나 준 희

나 준 희의 공학박사 학위논문을 인준함

2012년 6월

위원장 이병호 (인)

부위원장 이신두 (인)

위원 홍용택 (인)

위원 최종선 (인)

위원 최윤석 (인)

Abstract

A lot of polymeric materials and their devices have been the center of intense scientific and engineering research for many years because of fundamental success of molecular engineering in creating a new class of materials with appropriate physical and optical properties and easily controllable by an surface treatment or geometrical modulation. Polymeric materials offer far greater design flexibility and processing simplicity than current inorganic materials. Moreover, a significant advantage of macromolecular systems concerns the ability of combining various functional groups and fragments, as well as the ability of polymers to form stable films, fibers, and coatings that can be readily applied onto various substrates (metals, plastics, and ceramics) by simple methods such as spin coating, dipping, lamination, etc. In this thesis, electro-optic device based on polymeric materials with ordered interfaces produced by the surface treatments are studied in the viewpoints of the scientific researches and devices applications. The surface-induced ordering effects of the polymer based electro-optic device are numerically and experimentally investigated. Also, the novel concepts of the artificial human iris and their application proposed and practically demonstrated.

First of all, we demonstrate novel electro-optic device based on liquid crystals (LCs). In chapter 3.1, we examine the fully bound ferroelectric

liquid crystals in vertically aligned configuration and find a deformation of smectic layer in the confined geometry. Using a proposed model of propagation of smectic layer tilting and molecular ordering in the topographic confined geometry, we shown that topographic confinement occurs orthogonal anchoring forces and it is cause of structural deformation in the smectic layer. Also, numerical simulations performed using a layer compression and dilation theory within the molecular tilt angle formalism. This concept of using the smectic layer deformation phenomena should be directly applicable for electro-optic devices with high subthreshold slope and low driving voltage. Moreover in chapter 3.2, a symmetric-viewing inverse-twisted-nematic (ITN) liquid crystal display (LCD) with alternating alignment layers was developed using a stamping-assisted rubbing (SAR) technique. The LC cell in the ITN geometry with two orthogonally rubbed alignment layers showed symmetric-viewing characteristics with fourfold symmetry. The SAR technique was shown to be a mask-free alignment method of producing multidomains for symmetric-viewing LCDs. And a convertible lenticular LC lens architecture is demonstrated using an index-matched planarization layer on a periodically undulated electrode for the homogeneous alignment of an LC in chapter 3.3. It is found that the in-plane component of the electric field by the undulated electrode plays a primary role in the flat-to-lens effect while the out-of-plane component contributes to the anchoring enhancement of the LC molecules in the surface layer. Our LC device having an index-matched planarization layer on the undulated electrode is capable of achieving the electrical tunability from the flat surface to the lenticular lens suitable for 2D/3D convertible displays.

Next, biomimetic application of artificial iris was demonstrated in chap-

ter 4. We present a new concept of artificial iris that provides a self-regulation of light intensity without peripheral devices. Spoke pattern formation like radial muscles of human eye where a liquid crystalline polymer is used as an anisotropic (radially) patterned material. In addition, this biomimetic artificial iris is anatomically as well as functionally close to human eyes with unique regulation mechanism. The amount of light to retina, associated with photoreaction, is reversibly controlled through molecular bond reformation with irradiation of light source. This concept show promise applicability of prosthetic iris implantation or humanoid robotics.

In conclusion, throughout this thesis, functional polymer which is a matter of concern in electro-optic and biomimetic application was solved by adopting various surface treatment technique. Especially, micro wrinkling pattern formation is expected to have significant impact on micro patterning technique and surface modification areas. Moreover, researches on the new functional polymers and new device geometries are highly expected to provide a foundation for realizing the electro-optic device applications.

Keywords: functional polymers, liquid crystals, surface wrinkling, confined ferroelectric liquid crystal, stamping assisted rubbing, liquid crystal lens, artificial iris.

Student number: 2008-30873

Contents

Abstract	i
Contents	iv
List of Figures	vii
List of Tables	xvii
1 Introduction	1
1.1 Functional Polymers	2
1.1.1 Liquid crystalline polymers	2
1.1.2 Shape-transformable polymers	12
1.1.3 Fluorinated polymers	15
1.2 Patterning Techniques for Polymeric Materials	18
1.2.1 Conventional methods	18
1.2.2 Soft-lithographic techniques	21
1.3 Outline of Thesis	24
2 Pattern Formations of Liquid Crystalline Polymer	26
2.1 Polymerization of Liquid Crystalline Polymer	28
2.2 Anisotropic Wrinkling Patterns Through the Plasma Treatment	30

2.2.1	Unidirectional wrinkling patterns on rubbed surfaces	33
2.2.2	Selective wrinkling patterns on alternating surfaces	38
2.3	Symmetric Wrinkling Pattern Through UV Irradiation	47
2.3.1	Key factors of the wrinkle formation	48
2.3.2	Control of wrinkling patterns by the surface wettability	49
3	Advanced Electro-optic Device Applications	57
3.1	Ferroelectric Electro-optic Device with Microchannel Structures	58
3.1.1	Introduction	58
3.1.2	Fabrication of microchannel structure	59
3.1.3	Theoretical description and modeling	63
3.1.4	Electro-optic properties	68
3.1.5	Summary	70
3.2	Symmetric-viewing Liquid Crystal Display with Alternating Alignment Layers	72
3.2.1	Introduction	72
3.2.2	Schematic and operation principles	73
3.2.3	Fabrication process of alternating alignment layers	74
3.2.4	Electro-optic properties	76
3.2.5	Summary	80
3.3	2D/3D Convertible Display with In-cell Undulated Electrode	81
3.3.1	Introduction	81
3.3.2	Schematic and operation principles	82
3.3.3	Fabrication process of convertible lenticular LC lens	84
3.3.4	Electro-optic properties	87
3.3.5	Summary	94

4	Biomimetic Application	95
4.1	Concept of Artificial Iris	95
4.2	Photoreaction Process of Photochromic Dyes	98
4.3	Fabrication Process of Spoke Pattern Formations	101
4.4	Self-Regulation of Light Intensity	104
4.5	Summary	108
5	Concluding Remarks	109
	Bibliography	112
	Publications	122

List of Figures

1.1	Molecular arrangement of nematic (N), smectic A (SmA), and smectic C (SmC) phases.	4
1.2	Twist of the director in the SmC* phase.	8
1.3	Schematic representations of macromolecules of LC polymers with rod- and disk-shaped mesogenic groups.	11
2.1	Schematic diagrams ((a) and (b)) and optical microscopic images ((c) and (d)) show the before and after polymerization of LCP film using UV irradiation, respectively.	29
2.2	Schematic diagrams show the postulated steps of wrinkle formation.	31
2.3	Cured LCP with plasma treatment: (a)Surface topology and (b) microscopic image under crossed polarizers.	32
2.4	Schematic diagrams of the anisotropic wrinkling process with unidirectional rubbing technique. Here, d and d' represented the thickness of LCP, respectively. And w and p are width and period of wrinkle pattern, respectively.	34

2.5	Chemical constitution of RMS03-001C: (a) 4-(6-acryloyloxyhexyloxy)-benzoic acid (4-cyanophenyl ester), (b) 4-(3-acryloyloxypropyloxy)-benzoic acid 2-methyl-1,4-phenylene ester, (c) 4-(6-acryloyloxyhexyloxy)-benzoic acid-(4-methoxyphenylester), and (d) 2-methyl-1,4-phenylene-bis[4-(6-acyloyloxyhexyloxy)benzoate].	35
2.6	Optical microscopy images of the wrinkles induced by the plasma treatment of LCP film. LCP films prepared on alignment layer of rubbing (drum) speed of (a) 200, (b) 1000, and (c) 3000 rpm. Each insets show the image of FFT depending on the wrinkle morphology. (d)-(f) show the AFM images as a function of rubbing drum speed of 200, 1000, and 3000 rpm, respectively.	36
2.7	(a)-(c) Optical and (d)-(f) AFM images of the anisotropic wrinkle pattern with different RMS film thickness. The changes in thickness and period show the effect of film thickness on the morphology of anisotropic wrinkle. Each insets of (b) and (c) show the diffraction pattern image depending on the period of wrinkle.	37
2.8	Influence of the LCP film thickness on the geometric dimension of wrinkle. The morphological changes as a function of the LCP film thickness.	39
2.9	Schematic illustration of the procedure for transfer printing based on the work of adhesion.	40

2.10 SAR technique for achieving the bidirectional alignment of LCP layer: a stamping process involving transferring the commanding layer of a fluorinated polymer onto the first rubbed alignment layer, the substrate with the commanding layer on top of the first alignment layer, the second rubbing process on the first alignment regions that are not covered with the commanding layer, the fabricated bidirectional alignment layer which the rubbing directions are perpendicular to each other.	42
2.11 Microscopic images of the bidirectional alignment of LCP layer: (1) first alignment region, (3) second alignment region that are not covered with the commanding layer, and (2) region of between first and second alignment region.	43
2.12 Influence of the second rubbing condition on the first rubbed substrate. AFM images of (a) homogeneous alignment layer and (b) homeotropic alignment layer with different rubbing condition. (c) The angle of wrinkles changes as a function of second rubbing conditions.	44
2.13 Variety of alternative patterns via surface wrinkling. (a)-(c) Optical microscopy images of various wrinkling patterns produced on 700 nm thick LCP layer with SAR technique (the scale bar is 100 μm).	45

2.14	Schematic diagrams show the postulated steps of wrinkle formation using UV irradiation: (a) uniform surface before UV irradiation, (b) wrinkled surface after UV irradiation. Microscopic images of right side show the surface topography (the scale bar is 50 μm).	47
2.15	Microscopic images of the growth of a wrinkled surface obtained after UV exposure. (a) high (100 mW/cm^2) and (b) low (5 mW/cm^2) power UV. Here, the scale bar is 100 μm .	48
2.16	Irradiation conditions (UV exposure time and intensity) for wrinkling formation.	49
2.17	Schematic illustration of each step of the fabrication process of symmetric wrinkling using UV assisted inscription technique.	50
2.18	Optical micrographs of thick (thickness= 1.5 μm) wrinkled film according to the UV irradiation time ((a) 1 min and (b) 5 min) and (c) molecular trajectory in a two-dimensional ordered LC associated with disclinations of $s=\pm 1/2$.	52
2.19	Optical micrographs of wrinkles according to the occupation width of the LCP.	53
2.20	Numbers of disclination line was varied with the width of wetting region. The critical width of the wetting region is denoted by W_c , at which a transition occurs.	54
2.21	Optical micrographs of circular wrinkles according to the radius of occupation region.	55
2.22	Optical micrographs of variety wrinkling pattern under crossed polarizers.	56

3.1	Schematic diagram of the confined FLC cell with a channel structure of PDMS. Here, w and h denote the width and height of the channel structure, respectively. The FLC in the rectangular channel is injected by capillary action.	60
3.2	(a) Microscopic image of confined FLC cell under crossed polarizers. (b) The cross section of the PDMS channel structure. (c) Profile of light intensity along the x . Here, A and P represent the direction of analyzer and polarizer, respectively.	61
3.3	Schematic diagram of the propagation model of smectic layer deformation in the confined geometry.	63
3.4	Variation of the layer tilt and molecular tilt angle with numerical factor of $D^2=1000$	63
3.5	The transmission profiles according to the channel width. . .	64
3.6	Profiles of molecular twist (ϕ) depend on the confined structure.	66
3.7	Variation of the transmission under a bipolar electric field of square wave form at 240 Hz as a function of channel width. .	67
3.8	(a) Schematic diagram of confined VA-DHFLC cell. (b) The transmitted intensity under a bipolar electric field of square wave form at 240 Hz. The inset microphotographs, taken under crossed polarizers, correspond to the 0 and 7 V/ μm . .	68
3.9	The threshold electric field as a function of the confined channel width.	70

3.10 Schematic diagram and operation principle of the 4D ITN-LC cell: the alternating rubbing directions and the LC alignment (a) under no applied voltage (a dark state) and (b) in the presence of an applied voltage (a bright state) and the directions of the LC molecules (c) in the dark state and (d) in the bright state.	74
3.11 SAR technique for achieving the alternating alignment of LC: a stamping process involving transferring the protective layer of a fluorinated acrylate polymer onto the first rubbed alignment layer, the substrate with the protective layer on top of the first alignment layer, the second rubbing process on the first alignment regions that are not covered with the protective layer, the fabricated bidirectional alignment layer, and two substrates assembled such that the rubbing directions are perpendicular to each other.	75
3.12 Microscopic textures of the 4D ITN-LC cell with two alternating alignment layers observed under crossed polarizers at different voltages: (a) 0V; (b) 2V; (c) 3V; and (d) 5V.	77
3.13 EO characteristics of the 4D ITN-LC cell: (a)EO transmittance and (b) dynamic response as a function of the applied voltage in the square-wave form. The rising and falling times ($\tau_r = 28$ ms and $\tau_f = 25$ ms) were measured at 4V. The dark and gray curves represent the dynamic response and the applied voltage, respectively.	79
3.14 Iso-contrast contours: (a) a conventional ITN-LC cell and (b) the 4D ITN-LC cell with two alternating alignment layers.	80

3.15	The schematic diagram of convertible lenticular LC lens structure with a undulated electrode, giving the lenticular lens effect, in a planar configuration. Here, R_T and R_B denote the rubbing direction on the top substrate and that on the bottom substrate, respectively.	83
3.16	Schematic diagrams showing the operational principles of our lenticular LC lens: the optical states under (a) no applied voltage and (b) an applied voltage. Here, w and h denote the width and height of a lenticular cast, respectively. The cell gap is d	84
3.17	The fabrication process for the undulated electrodes: (a) an imprinting process of producing periodic lenticular casts of a UV curable polymer (NOA65) on a glass substrate, (b) ITO electrode deposition onto the lenticular patterns of NOA65, (c) coating of the PM (NOA65) on the undulated electrodes for planarization, and (d) the fabricated substrate with the buried electrode.	85
3.18	(a) The SEM image of an undulated electrode, (b) the microscopic image of the substrate with the undulated electrode, and the insets in (a) and (b) correspond to the surface profiles before and after planarization. Here, w denotes period of lenticular cast on the bottom substrate.	86
3.19	The microscopic textures of the lenticular LC cell observed when the crossed polarizers (A and P) make an angle of (a) 45° and (b) 0° with respect to the rubbing direction (R). Here, A and P denote the crossed polarizers.	87

3.20	The microscopic textures showing the GRIN effect of our lenticular LC cell under crossed polarizers at several different bipolar voltages at 1 kHz in square wave form. The symbols of P and A are the polarization directions of the polarizer and the analyzer, respectively.	88
3.21	The tunable focusing capability of the lenticular LC lens: (a) the schematic diagram of the experiment using an array of circular patterns as an input image and the microscopic images of the circular patterns observed through the lenticular LC array at an applied voltage of (b) 0 V, (c) 5 V, and (d) 10 V, respectively.	89
3.22	The tunable focusing capability of the lenticular LC lens: (a) an optical setup for measuring the ray focusing properties of our lenticular LC lens and the CCD images of a collimated laser beam in the focal plane at an applied voltage of (b) 0 V, (c) 5 V, and 10 V, respectively.	90
3.23	Numerical simulations of (a) the equipotential lines, (b) the spatial variations of the effective refractive index at 5 V and 10 V with E_y (solid lines) and without E_y (dashed lines). . .	91
3.24	The focal length variations of our lenticular LC array with the applied voltage. The experimental results were represented the circles. The solid and dashed lines denote the calculated focal lengths with and without the contribution of E_y , respectively.	93

4.1	Anatomical comparisons between a real human eye and proposed artificial eye described from the plane view. (a) An optical micrograph of real human eye. (b) An operation principle of human eye. Human eye change the aperture so that regulate the amount of light incident to the retina. Here, radius of pupil is r_d at the dark state and one is r_b at the bright state, this state can be changed, reversibly. (c) An optical micrograph of proposed artificial eye. The artificial eye consists of pupil part and iris part as real human eye. (d) The iris part of artificial eye can be self-regulation of the transmittance by photoreaction and radius of pupil r_0 is fixed.	97
4.2	The UV/visible absorption spectra of the photo-reactive dyes for transmittance tuning. (a)-(c) The absorption properties of three different dye doped PMMA films with amount of incident light.	99
4.3	The UV/visible absorption spectra of the photo-reactive dyes for transmittance tuning. (a) The absorbance and (b) optical images of the blended dye composed of dye1, dye2, and dye3 in PMMA at 6 % by weight.	100
4.4	The normalized transmittance $((T - T_0)/\Delta T)$ of human eye and proposed material for artificial iris (blended dye doped PMMA film).	101
4.5	Schematic illustration of each step of the fabrication process of proposed artificial iris using UV inscription.	102

4.6	(a) The condition of the UV intensity and exposure time for the wrinkling pattern formation. The critical intensity and exposure time of UV is denoted by region of red color at which a wrinkling pattern formation. Microscopic images of right side correspond to (b) the wrinkled surface and (c) the uniform surface. The scale bar is $30 \mu\text{ m}$	103
4.7	The experimental setup to measure the transmittance of the artificial iris using a controllable UV lamp. The artificial iris sample is placed in a temperature control system.	104
4.8	The dynamic response of our artificial iris under a UV light exposure at 0.8 mW/cm^2	105
4.9	(a) Schematic diagram of fabricated artificial iris. Here, R_i and R_p represented diameter of iris and that of pupil, respectively. (b)-(e) Photographic images of artificial iris in the presence of an applied UV light of 0, 5, 30, and 60 mJ, respectively.	106
4.10	A photographic image of artificial iris fabricated on a flexible substrate.	107

List of Tables

1.1	The material constants of PDMS.	13
1.2	The material constants of NOA65.	14
1.3	The physicochemical properties of EGC-1700.	17
1.4	Comparison between photolithography and soft lithography [19].	23

Chapter 1

Introduction

Polymeric materials and their devices have been the center of intense scientific and engineering research for many years because of fundamental success of molecular engineering in creating a new class of materials with appropriate physical and optical properties and easily controllable by an surface treatment or geometrical modulation. Equally as important as the primary electro-optical properties, polymeric materials offer far greater design flexibility and processing simplicity than current inorganic materials. Moreover, a significant advantage of macromolecular systems concerns the ability of combining various functional groups and fragments, as well as the ability of polymers to form stable films, fibers, and coatings that can be readily applied onto various substrates by simple methods such as spin coating, dipping, lamination, etc. Particularly, liquid crystals (LCs) and liquid crystalline polymers (LCPs) are very useful in several key areas of electro-optic (EO) devices and biomimetic applications.

In this thesis, electro-optic device based on polymeric materials with

ordered interfaces produced by the surface treatments are studied in the viewpoints of the scientific researches and devices applications. Especially, the surface induced ordering effects of the polymeric materials on the device performances are numerically and analytically investigated. Also, the novel concepts of the artificial human iris proposed and practically demonstrated. First of all, in this chapter, the physicochemical properties of functional polymers and patterning techniques for polymeric materials are briefly introduced.

1.1 Functional Polymers

1.1.1 Liquid crystalline polymers

Polymers with a controlled molecular organization are of interest because of their unusual, but very accurately adjustable and addressable optical, electrical, and mechanical properties. An established method to produce ordered polymers is the photo-initiated polymerization of liquid crystal monomers [1, 2]. The variety in possible LC phases of low-molar-mass reactive mesogens provides diversity in the choice of the type of molecular order, all being accessible to be fixed by the polymerization process [3, 4].

First of all, we will introduce variety LC phases. LC phases are formed by many different types of molecules which differ widely in their structure. Even though the shapes of the molecules are complicated, often they are referred to as rod-like. Other shapes do exist, which are not of interest

in this thesis. The orientation of a rod like molecule can be described by introducing two local axes, one parallel to the molecule known as long axis, and one perpendicular to it known as short axis. In general the molecules tend to align parallel to each other on the average leading to a preferred direction in space.

Nematic phase

In the nematic (N) phase the long axes of molecules are aligned, on average, parallel to a particular direction which can be indicated by a global unit vector \mathbf{n} called director. In principle the direction of the \mathbf{n} vector is arbitrary in space and represents the direction of the optic axis of the system (see Fig. 1.1). The nematic phase possesses an orientational order, but no positional order in a long range is present (centers of mass of the molecules are randomly distributed throughout the medium). Only the long axis of the molecules is more or less oriented, but there is a random distribution between the heads and the tails of the molecules. The nematic phase is therefore optically uniaxial. The measure of the degree of order in nematic phase is given by the so-called order parameter

$$S = \left\langle \frac{3}{2} \cos^2 \omega - \frac{1}{2} \right\rangle, \quad (1.1)$$

where ω is the deviation angle of individual molecules from the director. For isotropic liquids $S = 0$, for perfect orientational order (solids) $S = 1$ or and LCs typically have $0.5 < S < 0.7$. The order parameter of the LC decreases as the temperature increases.

On lowering the temperature of a nematic phase, additional features of order may appear, like positional order of the molecules' centers of mass. This leads to the layered structures (smectic phases), which can in fact be

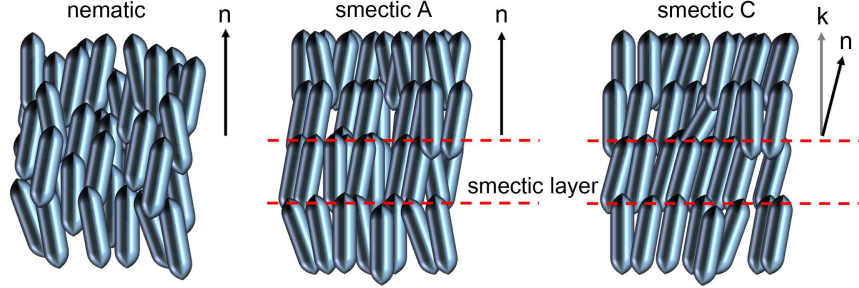


Figure 1.1: Molecular arrangement of nematic (N), smectic A (SmA), and smectic C (SmC) phases.

regarded as two dimensional liquids.

Smectic A phase

In the smectic A phase (SmA), molecules are oriented more or less parallel to each other and their position is ordered in layers, in which the layer spacing is approximately equal to the length of the molecules (see Fig. 1.1). It means that in addition to the orientational order, there exists a degree of positional order, determined by the formation of so-called smectic layers. The director in the SmA phase is normal to the smectic layers and determines the optic axis of the system. In reality, however, the layers are not strictly defined, but a plot of the density of centers of mass versus distance along an axis parallel to the director usually follows a sinusoidal variation:

$$\rho_s(x) = \rho_0 \left\{ 1 + \psi \sin \left(\frac{2\pi z}{d_0} \right) \right\} \quad (1.2)$$

where ρ_0 is the mean density and d_0 is the smectic layer spacing, which is typically a few nanometers. ψ is the smectic order parameter [5], which is the ratio of the amplitude of oscillation to the mean layer density, and hence expresses the extent to which the material is layered, typically $\psi < 1$.

Inside the layers, molecules are able to move like in liquids and there is no correlation in the position among them in adjacent layers. Smectic layers are flexible and slide over each other. Uniformity of the layers can be easily distorted but the interlayer spacing tends to be preserved. The smectic A phase, similarly to the nematic phase, is optically uniaxial.

Smectic C phase

The molecules in the smectic C phase (SmC) are still arranged in layers but, unlike in the SmA phase, they are not free to rotate around their long axis. The long axes of the molecules are tilted in a preferred direction with respect to the layer normal (see Fig. 1.1). The tilt direction of the molecules in neighboring layers is correlated. Therefore the projections of the molecules in the plane of the layers are aligned in a common direction. This is usually denoted by a unit vector \mathbf{c} , called \mathbf{c} -director. The system remains invariant for the transformation in director \mathbf{n} to $-\mathbf{n}$ but not for the \mathbf{c} director. The angle between the director and the layer normal \mathbf{k} defines the tilt angle of the material and is denoted as θ . The plane in which the tilt angle is defined, thus the plane spanned by \mathbf{k} and \mathbf{n} is usually called tilt plane. The fact that the molecules tilt away from the layer normal means that the director is confined to a conical surface of which the layer normal is the axis. In that sense the movement of the director is strictly limited to the orientations defined in space by the so-called smectic cone. Since the tilt is uniform over the whole structure, the arrangement is alternatively called synclinic order. The SmC phase is optically biaxial because there is no rotational symmetry around the director (there is a special azimuth corresponding to the layer normal).

Various LCs (especially mixtures) usually have more than one LC phase. Typically the appearance of phases as a function of the temperature is the following: (high temp.) isotropic phase - N - SmA - SmC - crystal (low temp.). The order of the phases always follows the rule that more ordered phases occur at lower temperatures than less ordered phases.

Other phases

In both SmA and SmC phases, the molecules randomly diffuse within the smectic layer. No positional order exists within each layer, so in a sense the positional order is in one dimension only. However, other smectic liquid crystal phases exist in which the molecules are somewhat ordered within the layers (bond orientational order). The molecules' centers of mass within a layer are then arranged on an oriented hexagonal net (hexatic phases). The positional order is then fully three dimensional. Various arrangements are possible, and these phases have been given names like SmB (no tilt within layers), SmI (molecules tilt towards apex of the hexagon) and SmF (molecules tilt towards side of the hexagon) [6].

Chiral smectic phases

When chiral molecules are mixed with achiral molecules in the SmC phase, the ferroelectric SmC* phase is formed. Resultant compounds have a helicoidal superstructure similarly characterized by helical pitch and its sign. In the smectic case, unlike the nematic, the dopant allows for an existence of a spontaneous polarization \mathbf{P}_S . This very important finding has been deduced from symmetry considerations, and states in a more general form that all chiral tilted smectic phases exhibit a local spontaneous polarization perpendicular to the plane spanned by \mathbf{k} and \mathbf{n} (tilt plane), thus in the

smectic layer plane. Mixing two chiral smectic compounds, the magnitude of the polarization, the magnitude and the sign of the pitch can be controlled.

In the SmC^* phase, where the molecules tilt with respect to the layer normal, the axis of the helix is along the layer normal. The director slowly rotates around the smectic cone progressively from layer to layer, preserving a constant azimuthal angle within a single layer (see Fig. 1.2). Since the helical pitch is in the order of micrometers, the director rotates around the full cone over several thousand smectic layers.

Since the polarization vector is always constrained to be in the smectic layer plane, and perpendicular to the molecule, all possible directions of \mathbf{P}_S are tangent to the basis of the smectic cone. In an undistorted field-free SmC^* sample, where the helical superstructure is able to develop, the spontaneous polarization will average to zero over one pitch, resulting in no macroscopic polarization of the system. That is why the name helielectric is more appropriate, rather than ferroelectric. Application of an electric field (perpendicular to the helix axis) will couple the polarization vector to the field direction and unwind the helix. It means that \mathbf{P}_S can be reoriented according to the direction of applied field. In 1980, Clark and Lagerwall presented a new idea of unwinding the helix by surface actions. The helix-free state obtained with this geometry exhibits ferroelectric properties by means of hysteresis behavior in a field polarity reversal. The configuration has been called surface stabilized ferroelectric liquid crystal (SSFLC) and triggered extensive investigations of SmC^* materials because of the potential for display applications.

As we mentioned above, nematic is not ferroelectric. Smectic liquid crystals have a layered arrangement of rodlike molecules. In SmA , the

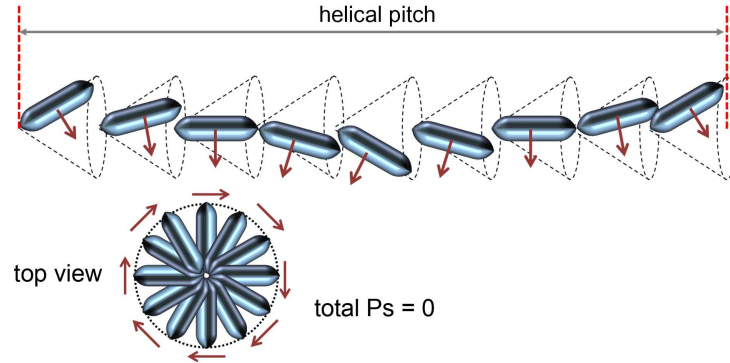


Figure 1.2: Twist of the director in the SmC* phase. Due to the resulting helical structure the polarization is canceled out on a macroscopic scale.

director and the layer normal are parallel to each other, while in SmC there is a tilt angle θ between them. If the molecules are chiral, the SmC layer has no mirror plane and it develops an permanent polarization \mathbf{P}_s in a direction perpendicular to the plane containing the layer normal and the director, and the resulting SmC* liquid crystal is often referred to as the ferroelectric phase. The chiral interaction, however, generate a helical structure about the layer normal and the polarization of a bulk medium averages out to zero. The layer polarization prefers to be aligned parallel to an external electric field and the relevant energy ($= -\mathbf{P}_s \cdot \mathbf{E}$) depends linearly on the field. Thus, the direction of the applied electric field is important unlike in the dielectric coupling (which depends on \mathbf{E}^2 exploited in the usual nematic displays. A deformed helix ferroelectric liquid crystal (DHFLC) mode has been investigated to exploit ferroelectrics in LCDs, which is described in the following.

Deformed Helix Ferroelectric Liquid Crystal Mode

The DHFLC mode is based on the material that has a helical pitch

shorter than the wavelength of visible light. The axis of the helix is perpendicular to the smectic layers. An externally applied electric field perpendicular to the helix axis deforms the helix, resulting in a rotation of the optical axis (the average direction of the molecules) away from the helix axis. The deformation is due to the interaction of the applied electric field with the molecules on the SmC cone in the direction of the field. The net polarization of the helix has the same polarity as the applied field and is zero for the undeformed helix. The transmission T of the cell between crossed polarizers is given by

$$T = T_0 \sin^2(2\alpha) \sin^2\left(\frac{\pi d \bar{\Delta}n}{\lambda}\right), \quad (1.3)$$

in which α is the angle between the optical axis and one of polarizer, d is the thickness of the LC layer, and $\bar{\Delta}n$ is the macroscopically averaged birefringence of the helical structure. The thickness of the LC layer is chosen according to $d\bar{\Delta}n = \lambda/2$. As the birefringence $\bar{\Delta}n$ of the helical structure is smaller than the molecular value Δn , the cell gap can be made larger than for an SSFLC, which corresponds to the unwound helix. With the helix axis parallel to one of the polarizers, the transmission T increases with increasing voltage, both for positive and for negative voltages. This mode of operation is called the symmetry mode. In the asymmetric mode, the crossed polarizers are rotated to give extinction when the helix is deformed by a positive or a negative voltage. The advantage of the symmetric mode is the possibility of ac driving, preventing interface charging, which would otherwise result in strong image-retention effects. The disadvantage is the somewhat lower transmission as the maximum rotation of the optical axis is limited by the cone angle, which for the present materials is smaller than 45° . Analog grayscale is easily obtained by amplitude modulation, as the

optical axis rotates gradually.

Liquid crystalline polymers

Liquid crystalline polymers (LCPs) are a kind of polymer that show liquid crystal phases in solid state. They are composed of low molecular mass LCs, which can be either rod-like or disc-like, or rod- and disc-like together in one. The constituent blocks may be of very complicated two-dimensional or three dimensional shape. Also, they may be composed of amphiphilic molecules as well. According to the way the mesogenic units are incorporated into the polymers, the LCPs can be classified as main chain LCPs in which the mesogenic units are connected in the backbone or side chain LCPs in which the mesogenic units are attached to the backbone as side pendants. The mesogenic units may be incorporated in both ways, that is, a part as the backbone and the other part as side groups attached to the backbone. This kind of LCP is called the combined LCP. The side groups may be attached to the backbone through their centers (side-on mode or laterally attached), or through their ends (end-on or terminally attached), or off-center attached (shoulderly attached). Figure 1.3 depicts some examples of LCPs. LCPs may be crosslinked to each other to form a network that retains the LC feature. The LC networks deform when a stress is applied as rubber does. They exhibit rubber elasticity. A typical example of a thermotropic LCPs is the polyesters and the mesogen substituted polysiloxane. The aromatic amide, the super strength fiber known commercially as Kevlar belongs to the lyotropic LCPs. The other important lyotropic liquid crystalline polymers are poly(γ -benzyl-L-glutamate), cellulose derivatives, the tobacco mosaic virus, etc.

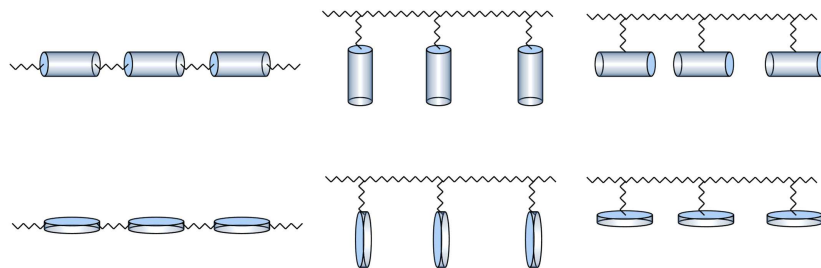


Figure 1.3: Schematic representations of macromolecules of LC polymers with rod- and disk-shaped mesogenic groups.

The presence of photochromic groups in the macromolecules of LC polymers or in the mixtures of dopants with polymers accounts for their sensitivity with respect to light or laser irradiation, which induces certain photochemical transformations. The photochromic groups play the role of effective 'switchers' capable of sharply changing their configuration and conformation upon photo-isomerization, photo-cyclization, and other reactions. Any change in shape of the photochromic guest molecules necessarily leads to the distortion of the local packing of the mesogenic groups, determining the type of the LC phase.

LC photochromic polymers occupy a special place among high-molar-mass photo-responsive materials. Note that any LC polymer shown in Fig. 1.3 may be considered as a photochromic polymer when its macromolecules contain photochromic groups. This statement concerns LC photochromic homopolymers and copolymers containing photochromic and mesogenic groups providing the development of an LC phase.

These polymers successfully combine the physicochemical properties of macromolecular compounds (with their ability to form plastics, elastomers, films, and fibers) with the mesomorphic properties of liquid crystals and

the photosensitivity of chromophores chemically or non-covalently included in LC polymers. The binary nature of photochromic LC polymers offers great advantages with respect to processing properties, photoactivity, stability of the stored information, and possible data recording on the thin polymer films. The pronounced ability of the above compounds for self-organization and formation of various ordered supramolecular structures under the action of external fields creates interest in the development of new materials with local properties controlled by optical methods. These materials could be used as new effective media for waveguides, laser disks, light-switched triggers, and optical storage devices for electronics, electro-optics, and holography [7,8].

1.1.2 Shape-transformable polymers

A lot of polymers have been widely used for nano- and micro-scale applications for surface patterning and replica molding. The replica molding technique provides a new strategy for making topologically complex structures and functional surfaces. It allows the sizes and shapes of features present on the surface of the mold to be changed in a controlled way such as mechanical compression, bending, stretching, or combination of these deformation and generates complex structures from simple, regular structures on planar surface. The highly isotropic deformation of the poly(dimethylsiloxane) (PDMS) (see Table 1.1) mold even permits patterned micro-structures to be formed with gradients in size and shape. The relief features on the PDMS mold are reconfigured by mechanical deformation, and deformed structures are replicated by casting an UV-curable

Table 1.1: The material constants of PDMS.

color	clear
dielectric constant @100 Hz	2.65
dissipation factor @100 Hz	0.0005
shore A hardness	50
viscosity	3900 cps
temperature range	-45 ~ 200 °C
thermal conductivity	0.16 W/K
volume resistivity	1.2e+14 Ωcm
curing condition	48 h @ room temperature
specific gravity @ 25°C	1.03
working time	120 min.
etc.	hydrophobic, water resistant

polymer or a thermally curable epoxy against it. The capability and feasibility of this procedure has been demonstrated in previous research [9–11]. These polymers, such as PDMS (Dow Corning) and Norland Optical Adhesive 65 (NOA65, Norland products), are mechanically robust, optically clear, chemically inert and stable and thus these polymers suitable for soft-lithography process.

PDMS stamps have been patterned usually against a master to form a relief pattern used in soft-lithography. This PDMS stamp can be used in either its current form as a relief surface for techniques such as micro-contact printing or can also be attached to an external source by tubing so that liquid may be passed through channels on its surface. In this second case,

it will often be laminated to a surface so that chemistry can be performed on that surface producing a pattern of the PDMS stamp on to the surface. Alternatively, a PDMS stamp can be laminated to a second piece of PDMS to form a contained device. It is possible to pattern PDMS with nanometer resolution. Many techniques have been developed to modify the basic setups to perform a range of tasks such as assays on small volumes. These kinds of devices are often referred to as microfluidic devices. Because of the small dimensions of these devices flow is laminar not turbulent which can lead to many useful properties.

Ultraviolet (UV)-curable polymer of NOA65 is a clear, colorless, liquid photo-curable polymer that will cure when exposed to UV light. Since it is a one part system and 100 % solids, it offers many advantages in bonding of optical materials where the bonding surface can be exposed to light and in imprinting of microstructure. The use of the NOA65 eliminates premixing, drying and heat curing operations common to other optical adhesive sys-

Table 1.2: The material constants of NOA65.

parameters	NOA65
solids	100 %
viscosity @ 25 °C	1200 cps
refractive index	1.524
modulus of elasticity (psi)	20,000
tensile strength (psi)	1,500
elongation @ failure	80 %
shore D hardness	50

tems. Curing time is remarkably fast, and is dependent upon the thickness applied and the amount of UV light energy available. The cured adhesive is very flexible and was designed to minimize strain. The NOA65 is especially suitable where the adhesive cross section would be relatively thick. The NOA65 has enough elasticity to keep strain to a minimum even when dissimilar materials with different coefficients of expansion are bonded together. Typical applications would be potting of lenses in metal mounts, bonding plastic to glass and cold blocking. The NOA65 is cured by UV light with a maximum absorption within the range of 350-380 nanometers. The energy required for full cure is 4.5 J/cm² of long wavelength UV light. The polymer has minimum oxygen inhibition, and therefore any surfaces in contact with air will be non-tacky when fully cured. For cleanup of the NOA65, acetone can be used if the cure has not progressed to far. If fully cured, methylene chloride can be used to soak assemblies apart [12].

1.1.3 Fluorinated polymers

Fluorous-solvents are perfluorinated or very highly fluorinated liquids, which are highly environmentally friendly, non-flammable and rarely toxic to humans. They also shows zero ozone depletion potential as well as low global warming potential. Moreover, the most important characteristics are that fluorous-solvents are typically immiscible with organic solvents and water, and they thus can satisfy the chemical orthogonality for processing general organic materials. Especially, fluorinated surfaces derive their characteristics from the unique molecular properties associated with the C-F bond that imparts a specific, unique chemistry and physics at inter-

faces. Their low surface tensions, low electrostatic loading, and low friction coefficient can play an essential role in microelectronics, anti-fogging and anti-fouling applications and there are promising in medical applications. It is well known that there are materials that have a lower surface tension than polytetrafluoroethylene (PTFE) [13]. These surfaces are often dominated by mainly CF_3 groups in the surface compared to the CF_2 groups of PTFE. The higher effectiveness of CF_3 compared to CF_2 groups in lowering the surface tension is attributed to the bulky F atom leading to a lower density of attractive centers per unit area at the surface [14]. Previous research established that the surface tension depends on the constituent groups and decreases in the order of CH_2 (36 mN/m) > CH_3 (30 mN/m) > CF_2 (23 mN/m) > CF_3 (15 mN/m) [15]. The properties of fluorinated surfaces depend not only on the coverage of the surface by the fluorocarbons but also on the degree of order in the surface [16]. A uniformly organized array of CF_3 groups can create a surface with a surface tension as low as 6 mN/m.

In this regards, fluorinated polymers, including EGC-1700 (3MTM Novec) and DS-1120F (Harves Co., Ltd.) are chosen for a commanding layer, which can be well dissolved in highly fluorous-solvents, to guarantee the chemical compatibility. Table 1.3 describes the general physical properties of EGC-1700. Note that this fluorinated polymer solution, EGC-1700, is comprised with fluorinated polymer which is very hydrophobic, and thus the commanding layer can be successfully applied to provide selective wettability as well. In addition, the commanding layer of the fluorous-solvent, HFE-7100, can be easily formed on a variety of substrates including a glass, a metal foil, and even a plastic substrate, due to the very low (61 °C) boiling points of fluorous-solvent, by the method of dip-coating in a uniform

Table 1.3: The physicochemical properties of EGC-1700.

properties	EGC-1700
appearance	clear, colorless or light-colored
specific gravity @ 25 °C	1.5
solvent	HFE-7100
boiling point of solvent	61 °C
surface energy of dry film	11 ~ 12 dynes/cm
dielectric constant @ 25 °C, 1 kHz	3.1
coating thickness	~ 1 μm
refractive index of dry film	1.38

thickness ranging from a few tens of nanometers to micrometer by simply varying the dip-coating speed and the solution concentration.

The use of a fluorinated polymer layer as a commanding layer is always possible provided two conditions are met. The first is that the fluorinated polymer layer can be easily patterned into fine features in a simple and cost-effective way. The other is that it can be clearly erased without any debris on a substrate. The fluorinated polymer can simply be removed by adding a fluorous-solvent even after the formation of thin films. For the patterning of commanding layers, in this thesis, two unconventional techniques, one of which is based on the optical method and the other on the soft-lithography, are devised to provide appropriate way of patterning such fluorinated polymer layer.

1.2 Patterning Techniques for Polymeric Materials

Structured thin polymer films have important applications in plastic electronics, biomedical devices, optical components, such as gratings or photonic crystals, and so on. In addition to conventional methods, such as shadow mask patterning, photolithography, and ink-jet printing, a number of bottom-up methods have been developed in recent years for making broad types of polymer patterns, such as microcontact printing, imprint lithography, soft-contact lamination, transfer patterning, phase separation, evaporative assembly, and various kinds of surface instabilities. Compared to conventional top-down methods, those bottom-up strategies share the common characteristics of natural design and facile manipulation.

1.2.1 Conventional methods

Shadow Mask Patterning with thermal deposition

Thermal sublimation in vacuum is the most common means for depositing small molecular organic thin films. This process involves the heating of the source material in a vacuum chamber, with the substrate located several centimeters distant, usually placed above the source. Thermal evaporation is widely used in the processing of inorganic semiconductor devices because of the precision with which layer thicknesses can be controlled (typically to within 0.5 nm), and the relative simplicity of the process. One partic-

ular advantage of thermal evaporation is its ability to grow an unlimited number of layers, each optimized for a different function, to complete the device structure. This flexibility in device design is an inherent feature of dry processing that is, the several material layers that are deposited to form a device structure do not physically interact because there is no solvent that might transport material and chemically attack the pre-deposited film. This compatibility between layers provides for enormous flexibility in choosing materials and structures to be used in complex, modern electronic devices. In thermal evaporation, various patterns can be easily produced by adding a shadow mask, which is usually a thin metal film with holes of desired patterns, between a source material and a substrate in a chamber. However, blurs and errors can be generated, as the size of the substrate increases or the features become smaller, by the sagging of thin metal mask due to the gravitational force, resulting in the limitation of pattern resolution over the large-area.

Ink-jet Printing

One emerging patterning strategy for solution-processed polymers is ink-jet printing. Patterns can be generated by ejecting a droplet of the solvated polymer from a micrometer-scale nozzle from a modified ink-jet printer and subsequently driving off the solvents from the droplet landed at the substrate. The ink-jet printing method enables to locally produce the parallel patterns of different classes of materials, while the entire substrate is coated with only a single material by the general solution processes including 'spin-on' or 'spray-on', and is demonstrated to fabricate full color organic light emitting diode displays. However, it is still difficult to produce precise

patterns through ink-jet printing since the pattern dimension is usually determined by the range where the polymer ink spreads out. Some kinds of preprocessing, therefore, are additionally required such as a fabrication of well structures to physically block the spread of polymer ink. Such structures might limit the freedom of designing device structures, and thus various surface treatments using plasma or UV are recently attracted much attention to locally control the surface wettability.

Photolithographic

Photolithographic techniques have been widely used in the inorganic semiconductor industry, which have the capability of high-resolution and high-throughput as well as the availability of well-established equipment and expertise. Patterning of thin films based on the photolithographic processes can be generally divided into two different methods, one of which is 'additive' and the other are 'subtractive'. In the 'additive' method, the target film is deposited onto the preformed photoresist (PR) patterns and subsequently lifted-off by removing the PR simultaneously with the residual thin films on it, leaving only the desired thin film patterns on a substrate. On the contrary, the etching process is used in the 'subtractive' method. The PR is first patterned on a pre-deposited thin film to be used as a 'etch mask'. The following etching process to erase the thin film exposed to the solvent completes the pattern generation on a substrate. Such two types of photolithographic patterning processes commonly have not been used in the fabrication of organic electronic devices mainly due to the chemical incompatibility. Organic solvents or other agents used in the photolithography might chemically attack or dissolve the pre-deposited organic films.

1.2.2 Soft-lithographic techniques

Microcontact printing (μ CP)

Micro-contact (μ CP) printing is one of the soft lithography that uses the relief patterns on a master PDMS stamp to form patterns of self-assembled monolayers of ink on the surface of a substrate through conformal contact. Its applications are wide ranging including microelectronics, surface chemistry and cell biology. The μ CP printing can be used in several different ways. The pattern generated by the printing can serve as an etch mask or it can become a patterned active area or it can define the electrodes. It can also be used to create a medium by which selective deposition is possible. Moreover, the μ CP printing has been used to advance the understanding of how cells interact with substrates. This technique has helped improve the study of cell patterning that was not possible with traditional cell culture techniques.

Imprint lithography

Imprint lithography [17] can also be used for the patterning for the fabrication of organic electronic or electro-optic devices. One distinct advantage of imprint lithography is its simplicity. The single greatest cost associated with device fabrication is the optical lithography tool used to print the circuit patterns. Also, imprint lithography is inherently a three-dimensional patterning process. Imprint molds can be fabricated with multiple layers of topography stacked vertically. Resulting imprints replicate both layers with a single imprint step, which allows device manufactures to reduce device

fabrication costs and improve product throughput. Moreover, the imprint material does not need to be finely tuned for high resolution and sensitivity. A broader range of materials with varying properties are available for use with imprint lithography. The increased material variability gives chemists the freedom to design new functional materials rather than sacrificial etch resistant polymers. A functional material may be imprinted directly to form a layer in a chip with no need for pattern transfer into underlying materials. The successful implementation of a functional imprint material would result in significant cost reductions and increased throughput by eliminating many difficult chip fabrication processing steps.

Transfer patterning

Transfer patterning [18] can be used not only for the transfer of one layer but also for multiple layers. Therefore, the method can be used to realize entire device transfer for patterns in the vicinity. In one example the multilayer structure of the organic light emitting diode including the cathode is transferred onto a patterned ITO anode on a glass substrate. Fluorinated ethylene propylene is, often, first deposited on a mold to reduce the work of adhesion at the mold interface, followed by sequential depositions of the aluminum cathode and organic multilayer stacks. Device transfer is accomplished by pressing the coated mold onto the substrate at a pressure ranging from 1 to 5 MPa at 50 °C for 5 min. After cooling to room temperature, the mold is simply removed, thereby, transferring the device structure on the protruding parts of the mold to the substrate. After the 1_{st} pixel is fabricated, the same procedure can be followed for aligning and transferring 2_{nd} and 3_{rd} pixels for RGB pixelation in organic light emitting diodes. The

Table 1.4: Comparison between photolithography and soft lithography [19].

	Photolithography	Soft-lithography
Definition of patterns	Rigid photomask	Elastomeric stamp or mold
Material that can be patterned directly	Photoresists (polymers with photosensitive additives) SAMs on Au and SiO ₂	Photoresists (μ CP, SAM) SAMs on Au, Ag, Cu, GaAs, Al, Pd, and SiO ₂ Conducting polymers Colloidal materials Sol-gel materials Organic and biological macromolecules
Surfaces and structures that can be patterned	Planar surfaces	Both planar and non-planar Both 2-D and 3-D structures
Limits to resolution	~ 20 nm	~ 30 nm (laboratory)
Minimum feature size	20 nm	30-100 nm

performance of the devices thus fabricated is equivalent to those formed in the conventional way.

1.3 Outline of Thesis

This thesis contains five chapters including **Introduction** and **Conclusion**. In **Chap. 1**, the various functional polymers will introduce such as liquid crystalline polymers (LCPs), shape-transformable polymers, and fluorinated polymers. Among them, the LCPs are given a full explanation because it has a unique optical anisotropy in solid state and the controllability of the optic axis in various geometries. In addition, the brief introduction of ferroelectric liquid crystals (FLCs) is provided in the view point of material properties. Moreover, In order to understand the issues regarding the fabrication processes, several methods in the range from the typical fabrication techniques, which have well been applied to the industry, to the unconventional patterning method mainly based on the soft-lithography are explained on the basis of respective merits and drawbacks. In **Chap. 2**, we will provide novel concepts of spontaneous pattern formation processes in LCP films through utilizing surface modifications. The LCP, incorporating the anisotropic mesogenic groups into polymer chains, is a polymer having LC state in solid state. The proposed methods enable the pattern formation of well aligned one- or two- dimensionally periodic micro-structures over the large area, without additional template or patterning steps. **Chapter 3** contains the electro-optic device applications including display and optical components. The FLC device with confined channel structure is first demonstrated. Second application is symmetric-viewing liquid crystal display with alternating alignment. And finally, we demonstrated the controllable lenticular LC lens for 2D/3D convertible display. In addition, we discussed that a certain external influence (such as, surface anchoring, electric fields, and optical fields) is used to (re)orient the LC in a certain

way. In turn, the LC then changes the light that is propagating through it. Of course, it is impossible to list all the fascinating new scientific results or breakthroughs. In **Chap. 4**, we present a new concept of biomimetic application of artificial iris that provides a self-regulation of light intensity without peripheral devices and spoke pattern formation like radial muscles of human eye where an LCP is used as an anisotropic (radially) patterned material. In addition, this biomimetic artificial iris is anatomically as well as functionally close to human eyes with unique regulation mechanism. Finally, some concluding remarks for our thesis are made in **Chap. 5**.

Chapter 2

Pattern Formations of Liquid Crystalline Polymer

Wrinkles or folds are ubiquitous in nature and often regarded as an undesirable defect [20,21]. When membranes are exposed to compressive strains, they typically respond already at rather low stresses by a so called buckling instability. The membrane deforms perpendicular to the stress direction and thus wrinkles are formed. In spite of their omnipresence, wrinkles have received comparably little attention by scientists so far. This is mainly due to the fact that buckling processes underlying wrinkle formation are instabilities that can only be described by nonlinear theories, often an analytical description is not possible which limits accessibility to specialists. However, due to the periodic nature of wrinkles, this spontaneous pattern formation is becoming increasingly attractive as a simple method to produce surface structures of micrometer scale that does not require predefined photo-masks or templates [22,23]. Moreover, these processes are interesting for their pat-

tern complexity as well as ease of formation with a dominant periodicity. The processes that underlie the formation of these spectacular patterns are usually governed by a physical instability whose evolution results in the selection of a characteristic wrinkling length scale. This length scale is often determined as the result of a compromise between two or more competing physical processes that favor structure formation on different length scales. Recently, structured surfaces are very attractive in various applications including stretchable electronics [24], photonics [25–27], wettability control [28], micro-fluidic devices [29], cell-based biosensors [30]. They also have been used to measure the mechanical properties of thin films [31] and to manufacture optical components such as diffraction gratings and optical diffusers [32]. To pattern, various techniques have been employed for the fabrication of micro- and nano-structures on solid substrates, such as colloidal lithography [33], surface relief grating [34], electro spinning [35], dip-pen lithography [36] or nano-imprinting [37]. However these methods have severe drawbacks, including high cost, the substantial inconvenience of using clean room facilities and their inability to generate complex patterns with gradients of amplitudes and tailor-made geometries.

In this chapter, we will provide novel concepts of pattern formation processes in liquid crystalline polymer (LCP) films through utilizing surface modifications such as plasma treatment and high power UV irradiation. The LCP, incorporating the anisotropic mesogenic groups into polymer chains, is a polymer having liquid crystal (LC) phase in solid state. The proposed methods enable the pattern formation of well aligned one- or two-dimensionally periodic micro-structures over large area, without additional template or patterning steps.

These methods of a plasma treatment and a high power UV irradiation for the pattern formation of LCP will be introduced in the viewpoint of the physical and mechanical properties of the patterns in the following section. Two types of patterning approaches will be explained in the **Chap. 2.1** and **Chap. 2.2**, respectively. And the properties of materials of polyimide- and fluorinated- polymer for the surface modifications will be introduced.

2.1 Polymerization of Liquid Crystalline Polymer

Before discussing the wrinkling of LCP, in this section, the chemical mechanism of polymerization in LCP film is briefly introduced. In chemical compounds, polymerization occurs via a variety of reaction mechanisms that vary in complexity due to functional groups present in reacting compounds. In more straightforward polymerization, alkenes, which are relatively stable due to bonding between carbon atoms, form polymers through relatively simple radical reactions. On the other hand, more complex reactions such as those that involve substitution at the carbonyl group require more complex synthesis due to the way in which reacting molecules polymerize.

When a LCP with reactive mesogenic group is formed as a thin film and irradiated with UV light of a wavelength to match the initiation wavelength of the photoinitiator break down to form free radicals, starting a rapid polymerization process as shown in Figs. 2.1 (a) and (b). New chemical bonds are formed as the polymerizable groups of reactive mesogens begin to link together. This causes the formation of cross-linked network of carbon-

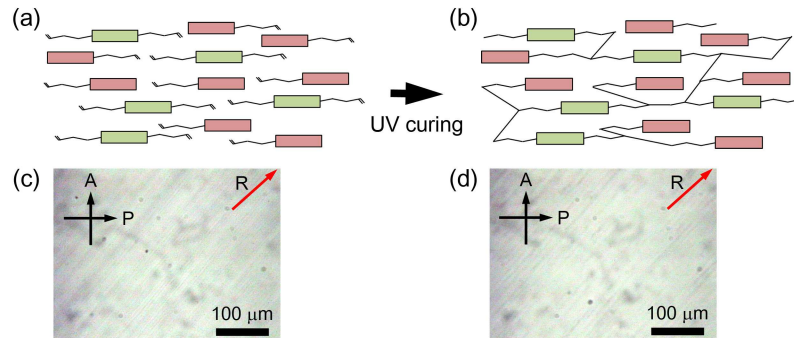


Figure 2.1: Schematic diagrams ((a) and (b)) and optical microscopic images ((c) and (d)) show the before and after polymerization of LCP film using UV irradiation, respectively.

carbon bonds. The LC core structures will remain ordered, but stop to move freely in LC phase. There is no chemical modification of LC core during the polymerization. In this way, a solid polymer film is formed with similar optical properties to those of LC phase prior to polymerization. Figures 2.1 (c) and (d) show optical microscopic images of before and after UV exposure under crossed polarizers, respectively. Here, P, A, and R represent the polarizer, the analyzer, and the rubbing direction, respectively.

For uniform LCP alignment, the polyimide (PI, AL22620, Japan Synthetic Rubber Co.) was spin-coated (3000 rpm for 30 s) on the glass substrate and thermally cured at 180 °C for 1 h. The surface of the coated PI film was subsequently rubbed by a conventional roller type rubbing machine. As shown in Fig. 2.1, the LCP film has uniform alignment regardless of polymerization.

2.2 Anisotropic Wrinkling Patterns Through the Plasma Treatment

Base on previous research [38], in the polymerization of polymers, external energy intensity, such as light and thermal, is a critically important factor of film uniformity because it is directly related the number of photons delivered. During the polymerization, lower energy density for a long time obtained uniform cured film. On the other hand, at higher energy densities, polymers had a higher coefficient of thermal expansion than at lower energy densities. So, higher energy density in a short time can cause non-uniformity of the cured surface. In this section, in order to form the non-uniform surface, the LCP film cure by using plasma exposure instead of low-dose UV light for polymerization.

Upon curing using the plasma, the liquid LCP develops a depth-wise gradient in degree of cross-linking or solidification as shown in Fig.2.2. The LCP layer starts developing a modulus. The top layer being most cured develops a modulus first and behaves like a solid skin, which is capable of supporting stresses as shown in Fig. 2.2(c). During the plasma treatment, the edges of the LCP layer appear to solidify first and thereby anchor the skin to the substrate. The strength and thickness of the skin depends on curing conditions. The skin under in-plane compressive (or tensile) stress can form wrinkles. During the polymerization, as the freely moving LCP molecules come close and cross-linking with each other, the skin shrinks or its stress-free state shrinks [39]. The stress-free state of the skin is the state that the skin would attain if it were allowed to deform freely. But the

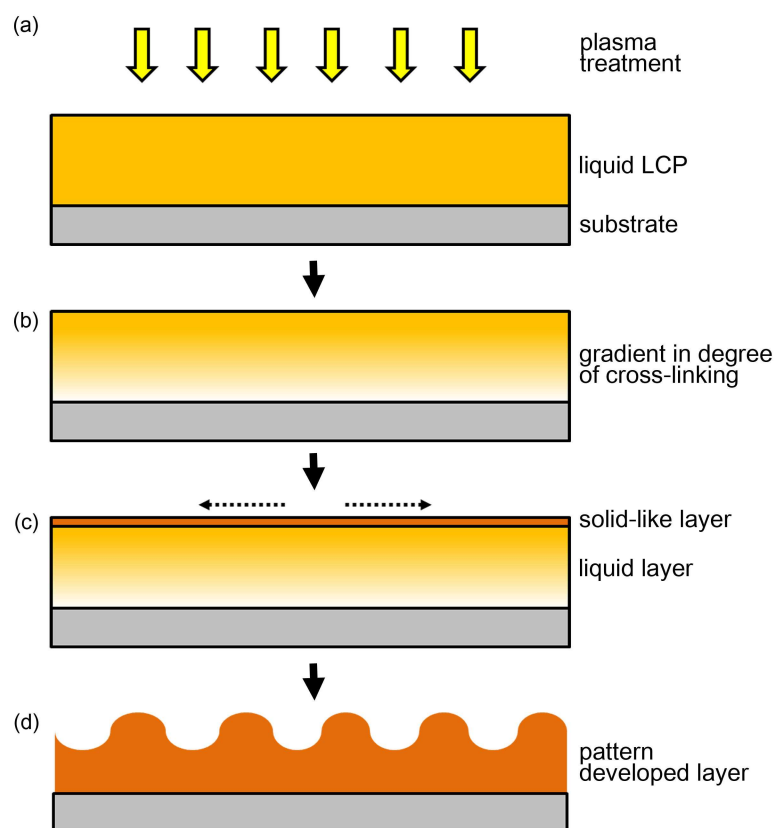


Figure 2.2: Schematic diagrams show the postulated steps of wrinkle formation.

skin is physically attached to the substrate at its edges and therefore cannot shrink freely. This frustrated shrinkage is expected to produce in-plane tensile stresses in the skin. On the other hand, the depth-wise gradient in the degree of cross-linking also results in un-reacted oligomer concentration in the opposite direction. This results in a gradient in chemical potential of the un-reacted oligomer, which is usually monotonic in its concentration that causes the oligomer to diffuse upward into the skin. Such low molecular weight diffusible oligomers are available. The skin, more specifically its

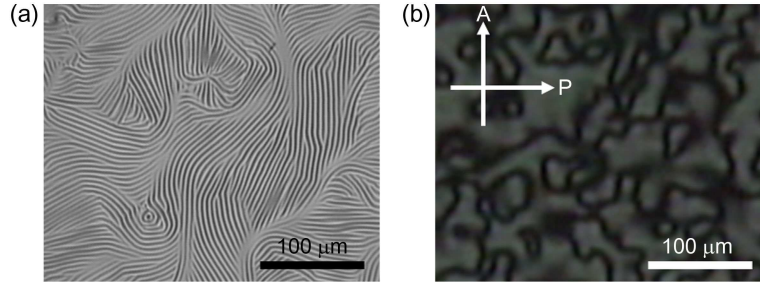


Figure 2.3: Cured LCP with plasma treatment: (a) Surface topology and (b) microscopic image under crossed polarizers.

stress-free state, swells by absorbing oligomers. The stress-free state of the skin, which was initially shrunken by reaction, gets progressively swollen by diffusing oligomers. Again, the skin being anchored to the substrate at its edges cannot swell freely and can therefore experience a compressive stress. There appears a competition between the tensile stresses resulted from shrinking of stress-free state by reaction, and compressive stresses resulted from swelling. Further diffusion of oligomer into the skin can slowly change the state of stress of the skin from tensile to compressive. It is hypothesized that the diffusing oligomer alone can generate enough in-plane compressive stress to make the plane state of the skin unstable with respect to buckling. The skin relieves stresses by out of plane deformation to produce wrinkles. Further curing solidifies the remainder of the LCP film and sets the wrinkle patterns.

Figure 2.3 shows the microscopic images of plasma treated LCP layer with wrinkled microgrooves that were observed with an optical microscope (Optiphot2-Pol, Nikon) under crossed polarizers. Since the modulus of the

curing, the LCP layer form isotropic wrinkles as shown in Fig. 2.3(a). Also, LCP molecules randomly aligned along the wrinkle pattern as shown in Fig. 2.3(b). These experimental results show that plasma treated LCP layer obtains wrinkle patterns and molecules of LCP aligned randomly.

2.2.1 Unidirectional wrinkling patterns on rubbed surfaces

As mentioned above, a variety of interesting applications takes advantage of the periodic nature provided by highly ordered wrinkling patterns, which were used as building blocks for hierarchical structures. This includes the utilization of wrinkled substrates as diffraction gratings and colloidal crystal assembly. Topographically patterned surfaces with periodicities order of micrometer are conventionally fabricated by lithography which is experimentally demanding in terms of equipment. We are proposing an alternative and simple method for the formation of anisotropic wrinkle pattern through utilizing anisotropic nature of molecularly aligned LCP. The proposed method enables the self-organized patterning of well aligned one- or two- dimensionally periodic micro-structures over the large area, in the absence of any additional template or elastomeric substrate.

Figure 2.4 depict the fabrication process of the anisotropic wrinkling. In this work, we use the LCP of reactive mesogenic solution (RMS03-001C, Merck Ltd.) which is UV curable, acrylate-based LC monomer solution for planar alignment [40]. The RMS03-001C is composed of four different acrylate-based monomer including 4-(6-Acryloyloxyhexyloxy)-benzoic acid (4-cyanophenyl ester), 4-(3-

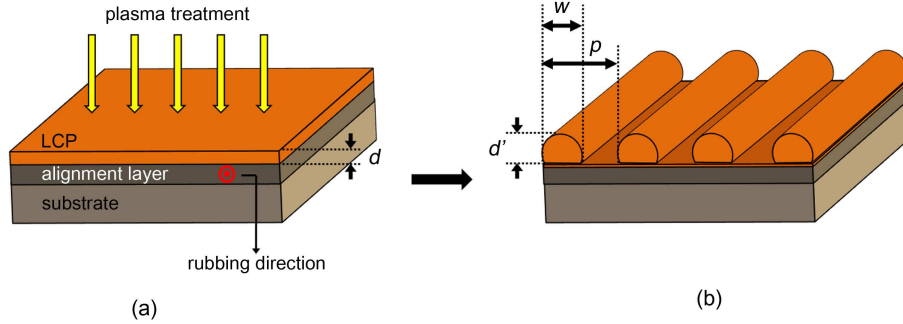


Figure 2.4: Schematic diagrams of the anisotropic wrinkling process with unidirectional rubbing technique. Here, d and d' represented the thickness of LCP, respectively. And w and p are width and period of wrinkle pattern, respectively.

Acryloyloxypropyloxy)-benzoic acid 2-methyl-1,4-phenylene ester, 4-(6-Acryloyloxyhexyloxy)-benzoic acid-(4-methoxyphenylester), and 2-methyl-1,4-phenylene-bis[4-(6-acyloyloxyhexyloxy)benzoate]. The molecular structures of RMS03-001C are illustrated in Fig. 2.5.

To align liquid LCP in a specific direction, the PI of AL22620 was spin-coated (3000 rpm for 30 s) and baked at 180 °C for 1 h. The surface of the coated PI film was subsequently rubbed by using rubbing method in a specific direction. When LCP was spin-coated (3000 rpm for 30 s) onto the rubbed PI film, the molecules of liquid LCP in contact with the PI film were aligned along the rubbing direction, and formed a unidirectional alignment state like nematic LC phase. At this step, the aligned LC state of the LCP film was confirmed by the visual inspection using crossed polarizers as shown in Fig. 2.1. Then, the sample was baked for 1 min at 60 °C so as to remove the residual solvent in liquid LCP. The LCP film thickness was

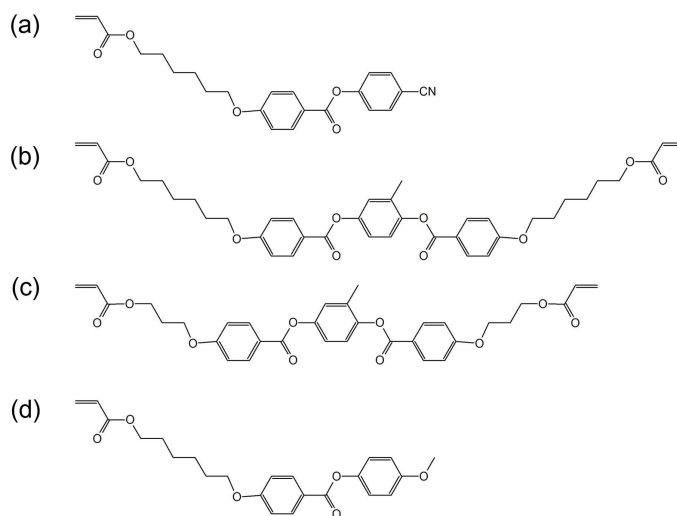


Figure 2.5: Chemical constitution of RMS03-001C: (a) 4-(6-acryloyloxyhexyloxy)-benzoic acid (4-cyanophenyl ester), (b) 4-(3-acryloyloxypropyloxy)-benzoic acid 2-methyl-1,4-phenylene ester, (c) 4-(6-acryloyloxyhexyloxy)-benzoic acid-(4-methoxyphenylester), and (d) 2-methyl-1,4-phenylene-bis[4-(6-acryloyloxyhexyloxy)benzoate].

measured by an atomic force microscopy (AFM, XE-100, Park Systems), exhibiting ~ 800 nm as the initial film thickness (*d*).

For the wrinkle formation, the prepared (uncured) LCP films were exposed to plasma environment. At this work, oxygen (O₂) was used as both carrier gas and reactive gas (at 0.1 torr). During the plasma exposure, the film of unidirectionally aligned LCP expands and the plasma induced cross-linking and oxidation occurs on the top surface. The formation of the cross-linked top skin layer can be explained by the plasma polymerization as mentioned above. As a result, the film has a bilayer constitution comprised of the polymerized hard skin layer supported on the still liquid LCP under

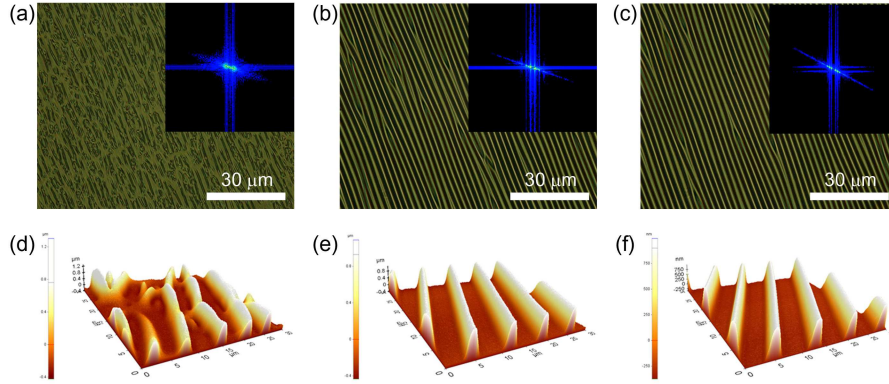


Figure 2.6: Optical microscopy images of the wrinkles induced by the plasma treatment of LCP film. LCP films prepared on alignment layer of rubbing (drum) speed of (a) 200, (b) 1000, and (c) 3000 rpm. Each insets show the image of FFT depending on the wrinkle morphology. (d)-(f) show the AFM images as a function of rubbing drum speed of 200, 1000, and 3000 rpm, respectively.

layer behaving viscoelastically. After a short (30 s) exposure to plasma, uniformly undulated patterns evolved on the LCP film surface.

Let us determine how the rubbing strength of alignment layer influences the wrinkle formation of the LCP upon the plasma treatment. We fabricated the anisotropic wrinkle formation with various rubbing condition (drum speed) of 200, 1000, and 3000 rpm. Figure 2.6 shows the rubbing condition-dependent anisotropic wrinkles as a function of the rubbing drum speed. Each inset (Fig. 2.6) show the image of fast Fourier transform (FFT) depending on the wrinkle morphology. According to the distributivity law, the FFT image obtains the strong anisotropy with increasing the rubbing (drum) speed. Note that, the FFT is used to gain information about the

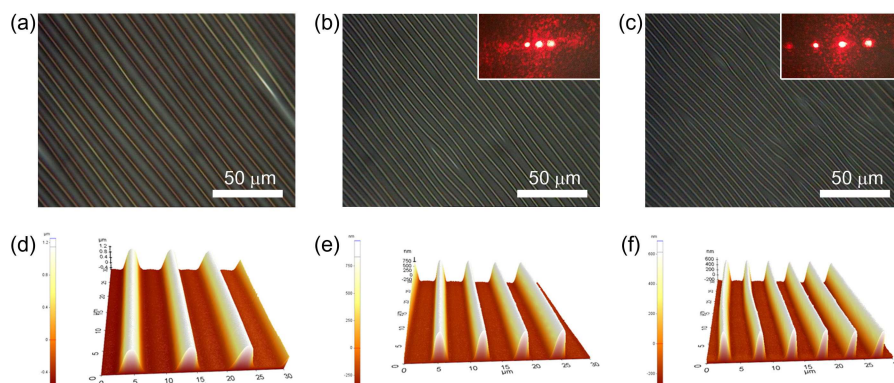


Figure 2.7: (a)-(c) Optical and (d)-(f) AFM images of the anisotropic wrinkle pattern with different RMS film thickness. The changes in thickness and period show the effect of film thickness on the morphology of anisotropic wrinkle. Each insets of (b) and (c) show the diffraction pattern image depending on the period of wrinkle.

geometric structure of the spatial domain image. The FFT is an important image processing tool which is used to decompose an image into its sin and cos components. The output of the transformation represents the image in the Fourier domain, while the input image is the spatial domain equivalent. In the Fourier domain image, each point represents a particular frequency contained in the spatial domain image. While an low speed rubbed layer has a relatively low uniformity and random molecular orientation, an high speed rubbed layer has a periodic wrinkle one-dimensionally aligned molecular orientation as shown in Fig. 2.6 (d)-(f).

Next, to examine the relationship between the thickness of coated LCP film and geometric dimension of wrinkle, plasma treatment condition (exposure time and power) was set and only the thickness of the LCP film was controlled by varying spin-coating speed from 2000 to 6000 rpm with 2000

rpm increment. Figure 2.7 shows the anisotropic wrinkle pattern with different (700, 1000, and 1500 nm) thickness of LCP film. As shown in Fig. 2.7, the topology of anisotropic wrinkle pattern can be controlled by changing the thickness of the LCP coating. The increasing film thickness (d) resulted in the formation of patterns with higher thickness (d') and larger period (p). Because, almost the same amount of strain was induced in the surface layer with the same duration of plasma exposure, and thus the thickness of the pattern with longer period tends to be larger than that with shorter period. As a consequence, the thickness of the pattern with increasing film thickness becomes larger. Each insets of Fig. 2.7(b) and (c) depict images of laser diffraction pattern. These showed the well-ordered periodicity of the anisotropic wrinkle pattern and period of wrinkles is reflected to the interval of each diffracted beam. A He-Ne laser of 632.8 nm was used as a light source for measuring the diffraction property of our wrinkled LCP sample. All the measurement were carried out at room temperature. So, well-defined wavy patterns of the anisotropic wrinkling in various film thicknesses also reflect that molecular alignment is well maintained over a sufficiently wide range of film thickness as shown in Fig. 2.8. Note that, with increasing film thickness, the sinusoidal waveform of wrinkle pattern was transformed into a rectified sinusoidal waveform due to the pinning.

2.2.2 Selective wrinkling patterns on alternating surfaces

Based on the above the results, we now describe the applicability of the selective wrinkling patterns on alternating surface. First of all, the transfer

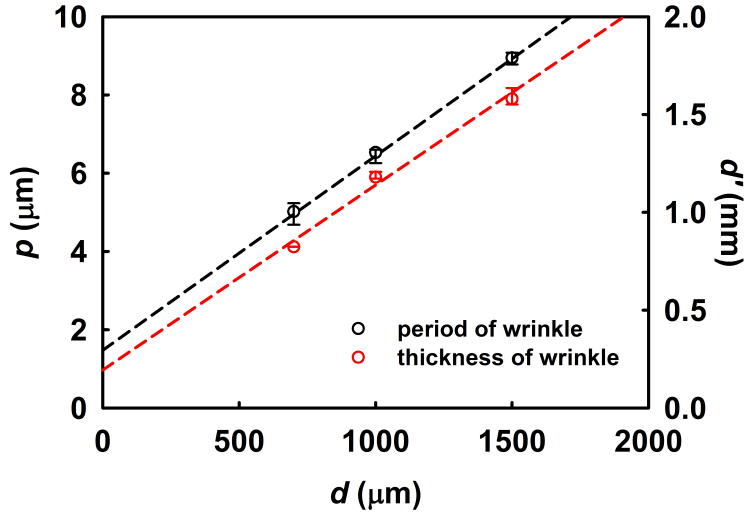


Figure 2.8: Influence of the LCP film thickness on the geometric dimension of wrinkle. The morphological changes as a function of the LCP film thickness.

printing method for alternating surface is briefly introduced. The transfer printing is one of the representative soft-lithographic techniques. From the general characteristics of soft-lithography, the transfer printing can also provide a capability of high-resolution patterning, large-area coverage, and a applicability even to curved surface. One of the attractive applications of the transfer printing is patterning of thin films to act as resists for following etch or rubbing processes [10, 41]. The transfer printing is particularly appealing to these systems since solvents used in traditional photolithographic processing can damage or degrade a bottom layer, such as alignment layer or substrate. Thus, the transfer printing method can be reasonably applied to the patterning of commanding layer in our work.

Such characteristics are essentially derived from the intrinsic nature of

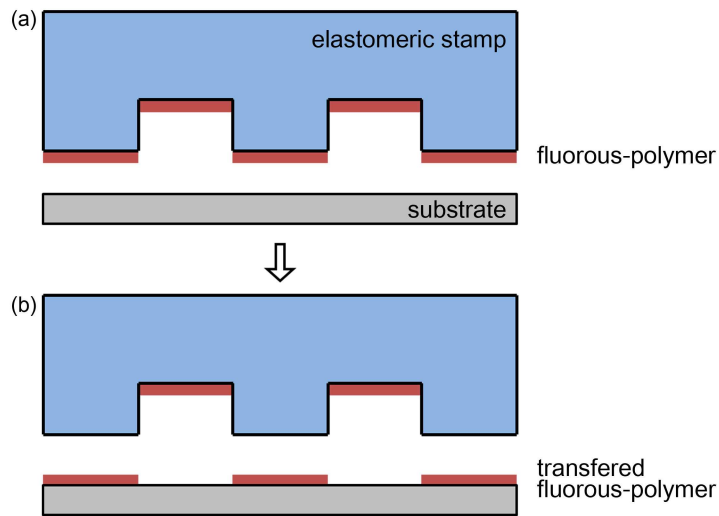


Figure 2.9: Schematic illustration of the procedure for transfer printing based on the work of adhesion.

the transfer printing which is based on the work of adhesion. Figure 2.9 shows the basic concept of transfer printing. A mold prepared for the desired pattern is coated with a film to be transferred. In our case, a fluorinated polymer thin-film was dip-coated on a predefined polydimethylsiloxane (PDMS) stamp. Note that a fluorinated polymer solution was successfully dip-coated on a surface of a PDMS stamp. PDMS is well known to be very hydrophobic, and thus most solutions can hardly be coated without any surface treatment on a surface of a stamp. However, the fluorinated polymer solution of EGC-1700 (3MTM Novec) can be clearly coated on a hydrophobic surface with very high uniformity due to the use of highly volatile fluororous-solvent of HFE-7100 (3MTM Novec). The solvent rapidly evaporated before the solution slips down from the surface of the PDMS

mold, leaving the fluorinated polymer molecules on it, and the uniform thin film of commanding layer can consequently be formed. Then, the mold is brought into contact with a substrate to transfer a fluorinated polymer film from a mold to a substrate. Without any need to apply heat or pressure, intimate contact between the fluorinated polymer thin film and the substrate is produced when the stamp is placed on a substrate. When the mold is peeled-off, the film on the protruding parts of the mold gets transferred to the substrate.

For this transfer to take place, the work of adhesion at the mold-polymer interface W_{mp} has to be smaller than that at the polymer-substrate interface W_{ps} [42, 43]. In our work, for the case of intimated contact and absence of specific chemical interaction, this work of adhesion can be approximately determined as

$$W_{mp} - W_{ps} = (\gamma_s - \gamma_m) - (\gamma_{ps} - \gamma_{mp}) \quad (2.1)$$

where, γ_m , γ_p , and γ_s are the surface energies of the mold, the fluorinated polymer film, and the substrate, respectively. The γ_{ps} and γ_{mp} are the interfacial binding energies between the fluorinated polymer film and the substrate and between the mold and the fluorinated polymer film. The first term $(\gamma_s - \gamma_m)$ can be much larger than the second term $(\gamma_{ps} - \gamma_{mp})$, since it is often the case that $\gamma_p \ll \gamma_m$ or γ_s . The difference in work of adhesion is then roughly equal to the difference in surface energies of the substrate and the PDMS mold. For most substrate including a glass or a plastic which are widely used for the electro-optic devices, the PDMS mold interface is weaker than the substrate interface. Accordingly, the fluorinated polymer film can be easily transferred from the mold to the substrate [44].

Now, we will introduce the novel fabrication method of bidirectional

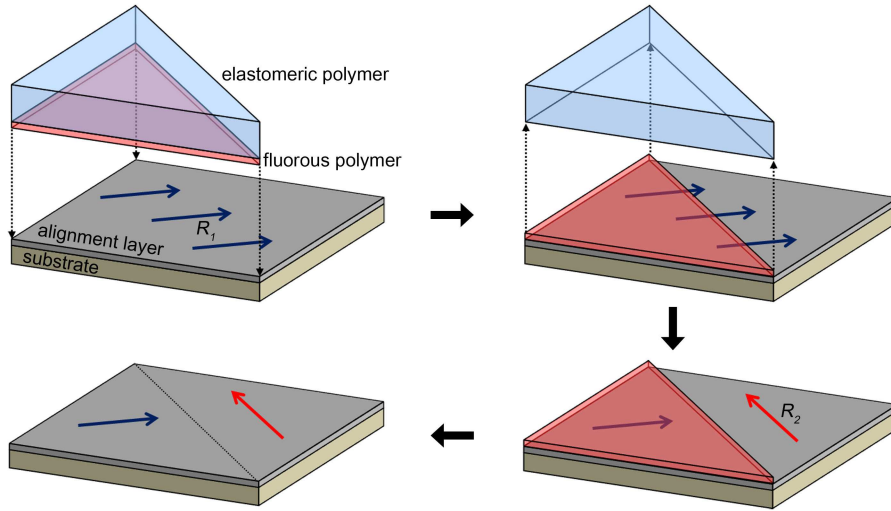


Figure 2.10: SAR technique for achieving the bidirectional alignment of LCP layer: a stamping process involving transferring the commanding layer of a fluorinated polymer onto the first rubbed alignment layer, the substrate with the commanding layer on top of the first alignment layer, the second rubbing process on the first alignment regions that are not covered with the commanding layer, the fabricated bidirectional alignment layer which the rubbing directions are perpendicular to each other.

wrinkled layer based on the stamping assisted rubbing (SAR) technique. The SAR technique for achieving bidirectional alignment is illustrated in Fig. 2.10. The alignment layer of PI (AL22620) was spin-coated on a substrate and then rubbed unidirectionally to promote homogeneous alignment. To generate bidirectional LC alignment, a commanding layer on a patterned stamping mold of PDMS was transferred onto the first rubbed PI by stamping, and was cured at room temperature. The second rubbing process was then performed on the uncovered regions with a commanding layer, along

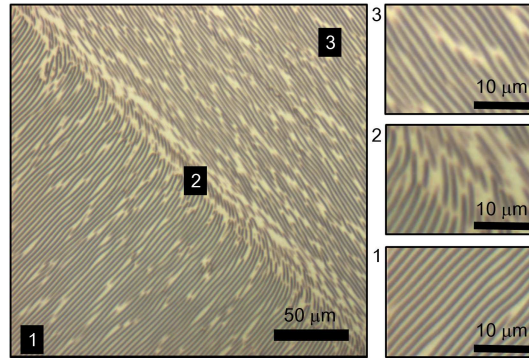


Figure 2.11: Microscopic images of the bidirectional alignment of LCP layer: (1) first alignment region, (3) second alignment region that are not covered with the commanding layer, and (2) region of between first and second alignment region.

the direction of perpendicular to the first rubbing direction. The substrate was rubbed twice to ensure the saturation of the tilt bias angle [45]. Finally, the commanding layer was dissolved in the hydrofluoroether solvent of HFE-7100, and bidirectional alignment was readily achieved. Then, LCP layer spin-coated and bidirectional wrinkles induced in the LCP layer with the plasma treatment as mentioned above.

Figure 2.11 shows microscopic images of LCP layer with bidirectional wrinkled domain by using SAR technique. Since the direction of wrinkles is determined by the rubbing, direction of wrinkles that the second alignment region (region of uncovered with the commanding layer) changed along the second rubbing direction as shown in Fig. 2.11(3). Note that, intermediate

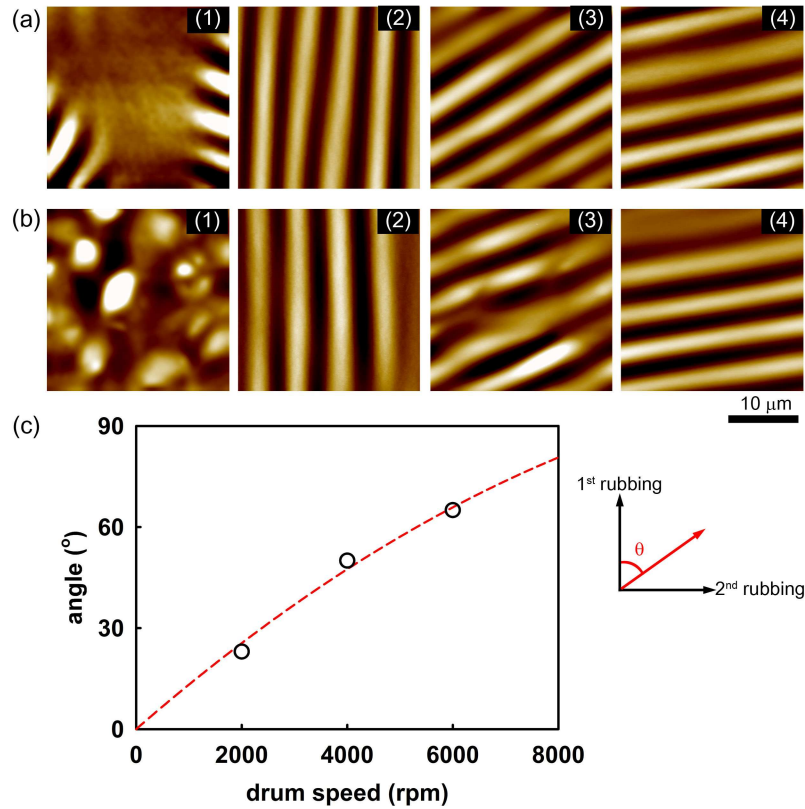


Figure 2.12: Influence of the second rubbing condition on the first rubbed substrate. AFM images of (a) homogeneous alignment layer and (b) homeotropic alignment layer with different rubbing condition. (c) The angle of wrinkles changes as a function of second rubbing conditions.

region coexist both aligning properties.

To further elucidate the mechanism of pattern formation and transition, a series of in situ studies were performed under AFM. Figures 2.12(a) and (b) show AFM images of wrinkled LCP layer on the homogeneous (AL22620) and homeotropic (AL60702, Japan Synthetic Rubber Co.) alignment layer, respectively. Also, (1)-(4) are LCP layer with different align-

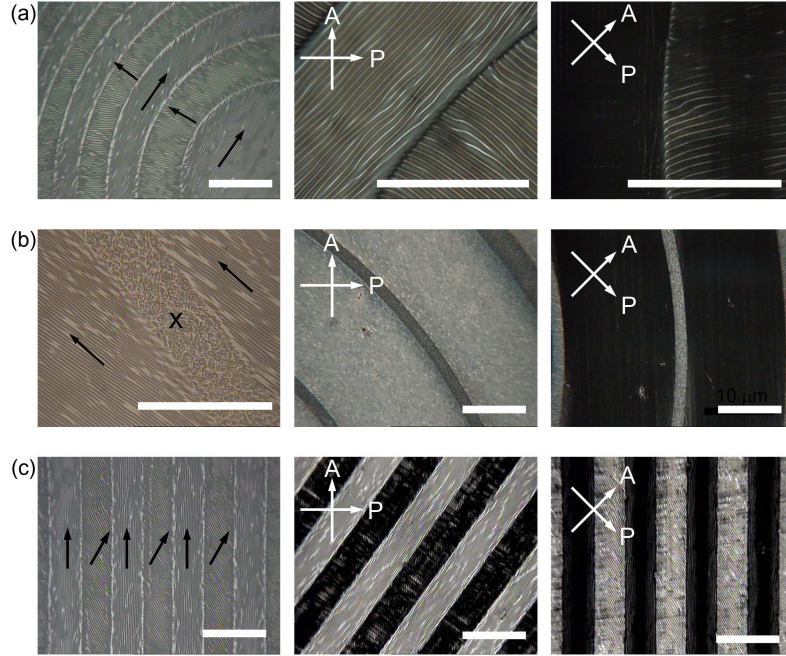


Figure 2.13: Variety of alternative patterns via surface wrinkling. (a)-(c) Optical microscopy images of various wrinkling patterns produced on 700 nm thick LCP layer with SAR technique (the scale bar is 100 μm).

ment conditions such as (1) un-rubbed, (2) 1st rubbing of 2000 rpm, (3) (2)+2nd rubbing of 4000 rpm, and (2)+2nd rubbing of 6000 rpm. When alignment layer rubbed in one direction, one dimensional wrinkles appeared along the first rubbing direction. When the second rubbing (perpendicular with the first rubbing direction) was subsequently applied to the first rubbed alignment layer before LCP coating, the final released wrinkle pattern was found gradually transition itself from 0° to 90° respect to the first rubbing direction as shown in Fig. 2.12(c).

A variety of patterns was observed by using SAR technique with dif-

ferent predefined elastomeric mold. These included concentric circles, line-by-line with alternative wrinkles are shown in Fig. 2.13. Wrinkles of these patterns aligned along the rubbing direction and the anisotropic molecular orientation of the LC phase at the surface layer is preserved in the cross-linked polymer network. Optical microscopy (Optiphot2- Pol, Nikon) under crossed polarizers was used to examine the topology of the resulting patterns.

2.3 Symmetric Wrinkling Pattern Through UV Irradiation

Based on the wrinkling patterns produced by plasma treatment, we now describe another technique of wrinkling by using UV irradiation. It is very simple and generic platform to pattern functional polymer films without vacuum process. As mentioned above, the LCP film starts developing a modulus due to the polymerization. The top layer being most cured develops a modulus first and behaves like a solid skin, which is capable of supporting stresses. The skin relieves in-plane compressive (or tensile) stresses

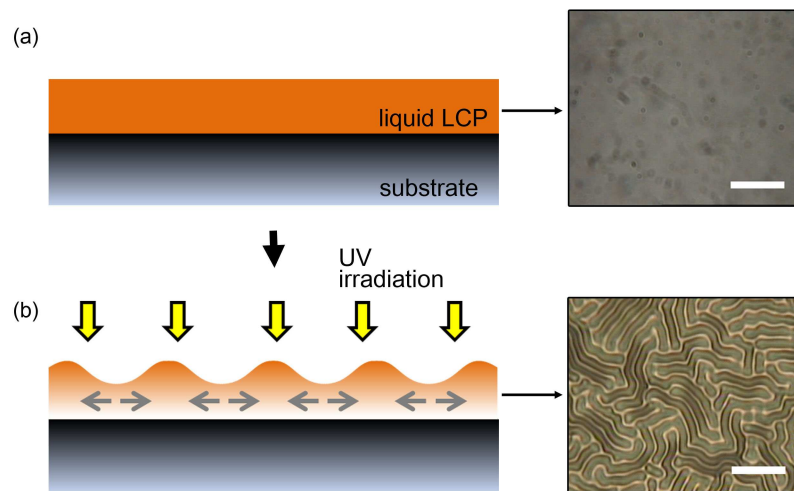


Figure 2.14: Schematic diagrams show the postulated steps of wrinkle formation using UV irradiation: (a) uniform surface before UV irradiation, (b) wrinkled surface after UV irradiation. Microscopic images of right side show the surface topography (the scale bar is $50 \mu\text{m}$).

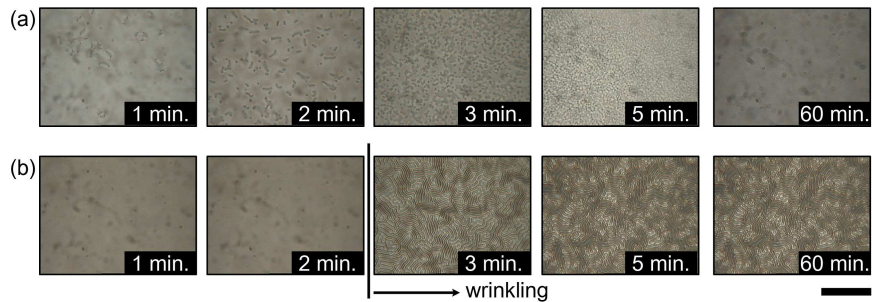


Figure 2.15: Microscopic images of the growth of a wrinkled surface obtained after UV exposure. (a) high (100 mW/cm^2) and (b) low (5 mW/cm^2) power UV. Here, the scale bar is $100 \mu\text{m}$.

by out of plane deformation to produce wrinkles through UV irradiation as shown in Fig. 2.14. In this section, symmetric wrinkling pattern of LCP film produced by using UV irradiation and selective wettability.

2.3.1 Key factors of the wrinkle formation

To investigate the relationship between the UV intensity and the wrinkle formation, LCP films were irradiated with different UV intensity. Figure 2.15 shows microscopic images of the LCP film according to the UV exposure time. As shown in Fig. 2.15(a), LCP films prolonged exposure to low intensity UV (5 mW/cm^2) cannot form wrinkles. On the other hand, when exposure to high (100 mW/cm^2) intensity UV, even a relatively small time exposure it is the formation of wrinkles. It is found that UV intensity is one of the critical factors to form surface wrinkling. Based on the above the result, Fig. 2.16 shows the condition of the UV intensity and the exposure time for the wrinkling pattern formation. The critical intensity and expo-

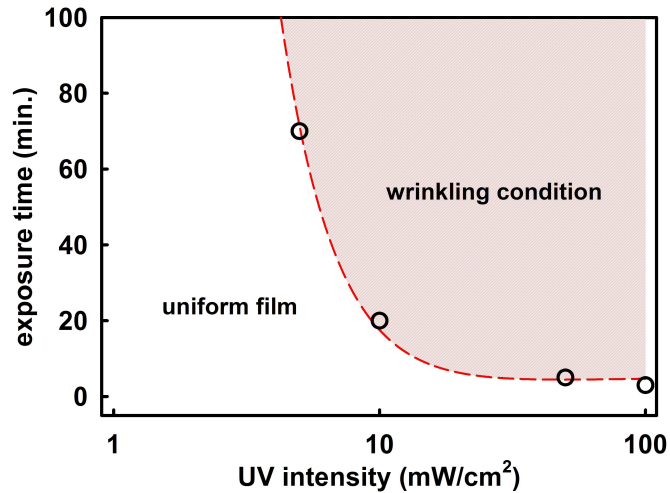


Figure 2.16: Irradiation conditions (UV exposure time and intensity) for wrinkling formation.

sure time of the UV is denoted by region of red color at which a wrinkling pattern formation. Prolonged exposure to UV even at low intensity UV that there are no wrinkles can be formed.

2.3.2 Control of wrinkling patterns by the surface wettability

As mentioned above (Fig. 2.5), a material of LCP which is used in the work has both hydrophilic and hydrophobic groups, these means that, the LCP can be aligned by using the surface wettability. We develop a simple and powerful method of fabricating wrinkled microstructure arrays through UV assisted inscription technique. Figure 2.17 shows the schematic illustration of each step of the fabrication process of aligned wrinkles using

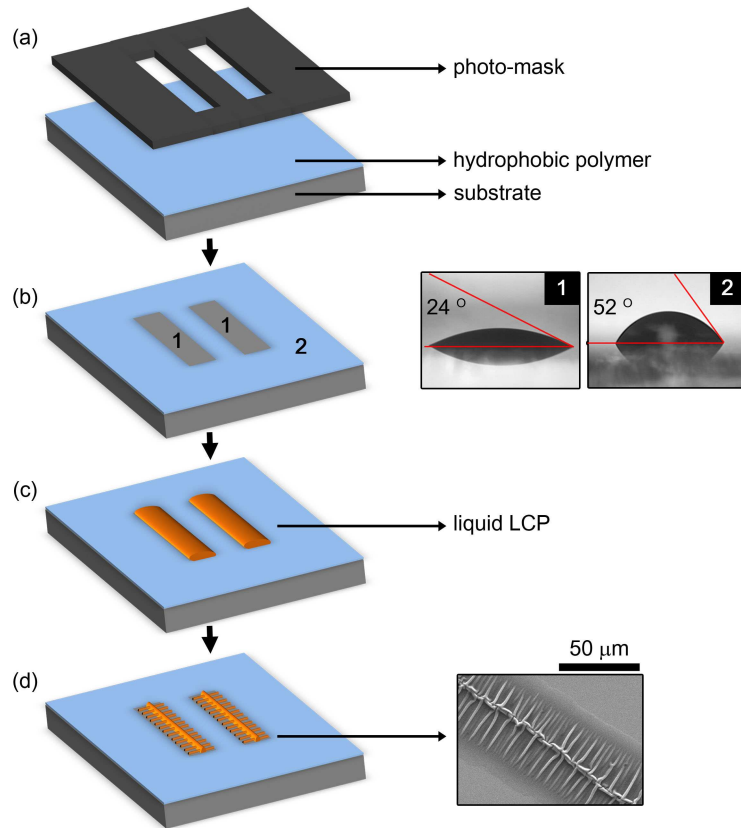


Figure 2.17: Schematic illustration of each step of the fabrication process of symmetric wrinkling using UV assisted inscription technique.

UV assisted inscription technique.

Now let us describe the detail fabrication processes of aligned wrinkles. First, hydrophobic fluorinated polymer (DS-1120, Harves Co., Ltd.), was spin-coated on a glass substrate and cured at 85 °C for 30 min, for use as a commanding layer. The thickness of the commanding layer was varied from a few tens of nanometers to a few hundred nanometers, while varying the spinning rate and the solution concentration. Here, we used the ~ 300 nm-thick commanding layer. And then, UV-inscription ablation technique

is then performed. The substrate coated with fluorinated polymer commanding layer is exposed to the UV light ($\lambda=365$ nm). The total amount of energy absorbed from the UV light should be adjusted so that it is above the threshold of the commanding layer ablation. By exposing a commanding layer to UV light through a predefined photo-mask, desired patterns can be inscribed onto a commanding layer as shown in Fig. 2.17(b). It should be noted that quartz has to be used for a photo-mask, not a soda-lime glass, so that total energy of UV light can reach the commanding layer without any loss. Such UV-inscription method may be preferred for the precise patterning in high-resolution due to the technical similarities with the typical photolithography which shows the capability of high-resolution patterning down even to sub-micrometer scale. The contact angles of the water on inscribed region and commanding layer region were measured as 24° and 52° , respectively. Then, a self-patterning of liquid LCP can be achieved through a simple method of a dip-coating by spontaneously dewetting hydrophobic regions and wetting hydrophilic regions as shown in Fig. 2.17(c). Here, liquid LCP coated with the dip-coating speed of 20 mm/min. Finally, high power UV light irradiated liquid LCP and wrinkles are formed symmetrically relative to the center line as shown in Fig. 2.17(d).

Theoretically, Frank predicted accurate director patterns around disclinations in his continuum theory based on Oseens work [46]. The detailed molecular trajectories are distinguished by disclination strength s and a value of constant parameter, c , which relates the axial position in the plane around the disclination core (polar angle θ) and the director orientation angle θ : in the simplest case, $\theta=s\theta+c$. According to this theory, one negative pattern and one positive pattern for $s=\pm 1/2$, and one negative pattern and

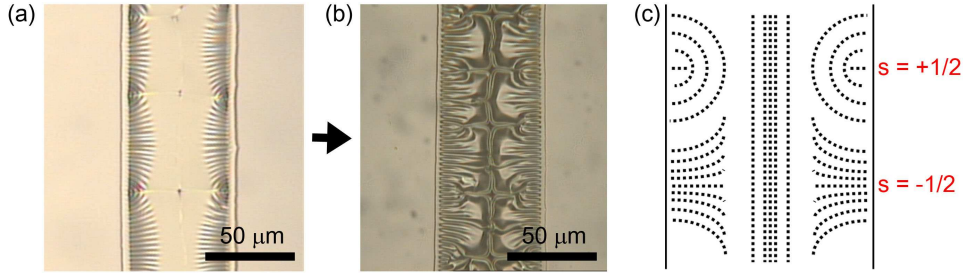


Figure 2.18: Optical micrographs of thick (thickness= $1.5 \mu\text{m}$) wrinkled film according to the UV irradiation time ((a) 1 min and (b) 5 min) and (c) molecular trajectory in a two-dimensional ordered LC associated with disclinations of $s=\pm 1/2$.

three positive patterns for $s=\pm 1$ can be expected in a two-dimensional ordered LC. Under polarizing optical microscopy, all these patterns exhibit black brushes due to optical effect, following a simple function $s = \text{brushnumber}/4$ [47–49].

Figures 2.18(a) and (b) show optical micrographs of the $1.5 \mu\text{m}$ -thick LCP film according to the UV irradiation time. Compared to the thin films as shown in Fig. 2.17(d), the thick film in Fig. 2.18(b) exhibited singularity along both side of the edge. This result indicates that integer disclinations are not stable in the thick films. One can still see the periodic wrinkles in the thick films, although they become ambiguous due to the weak effect of equilibrium instability. Figure 2.18(c) shows director pattern of molecular trajectory in line with strengths of $s=\pm 1/2$ (half-integer disclinations) in the thick films. As predicted by Frank theory, the director patterned around each singular point. Obviously, the film thickness plays a crucial role in disclination instability. This is expected since the precise nature of defects observed in the planar films will depend on the detailed balancing of distur-

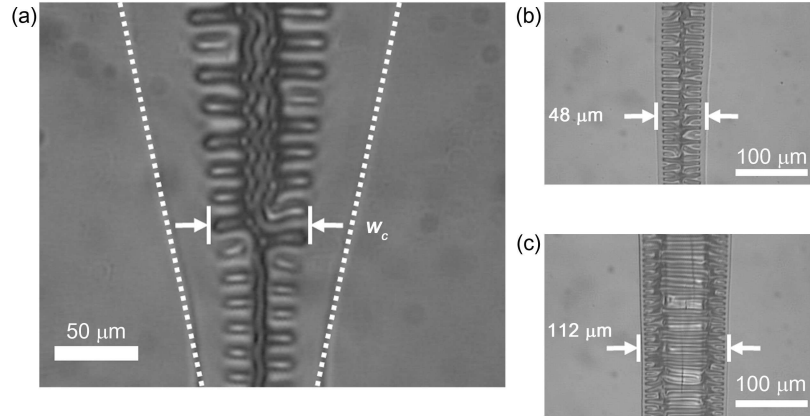


Figure 2.19: Optical micrographs of wrinkles according to the occupation width of the LCP.

tion of defects in the bulk elastic energy, and surface anchoring energy [50]. For a thin film, the surface anchoring energy due to confined environments, and the strong interaction between LC molecules and substrate, dominates over the bulk elastic energy.

LCs are characterized by a preferred orientational order, which is described by an apolar director n field. The most probable director configuration is determined by minimization of the total free energy with respect to the director field. Knowing the disclination microstructure can shed light on defect mobility, which, in turn, affects the physical properties of LCs. In confined LCs, a disclination is an orientational symmetry-breaking defect [51] as shown in Fig. 2.19, and it is defined by characteristic length, the region with uniform alignment, of an LC. As mentioned above, the LCP has both hydrophilic (Acrylic and Ester group) and hydrophobic group and thus LC molecules of the LCP prefer to be aligned perpendicular to the edge of wetting region. However, as increase distance from the edge, (pe-

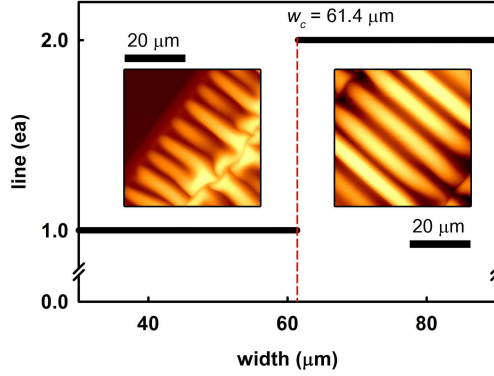


Figure 2.20: Numbers of disclination line was varied with the width of wetting region. The critical width of the wetting region is denoted by W_c , at which a transition occurs.

riodic wrinkles) orientation properties are weakened and disclination could be formed. Figure 2.19 show the symmetric wrinkles with disclination as the center according to the width of wetting region. An important point to notice here is that number of disclination line can be changed by width of wetting region as shown in Fig. 2.19(a). Here, W_c represent the critical width of wetting region. Moreover, Figs. 2.19(b) and (c) show different size of wetting region. These show examples that the disclination line can be changed by width of wetting region.

As shown in Fig. 2.20, the number of disclination line on wrinkled LCP stays fairly constant up to a certain width, W_c , after which it abruptly increases, and then keep as width increases. This is indeed indicative of a disclination transition whose region is about $60 \pm 2 \mu\text{m}$.

In case of circular patterns, the radius of the circle plays an essential role on the domain formation of a unit circle, from spoke type to 6 fold symmetry type. The images observed with a microscope indicated that

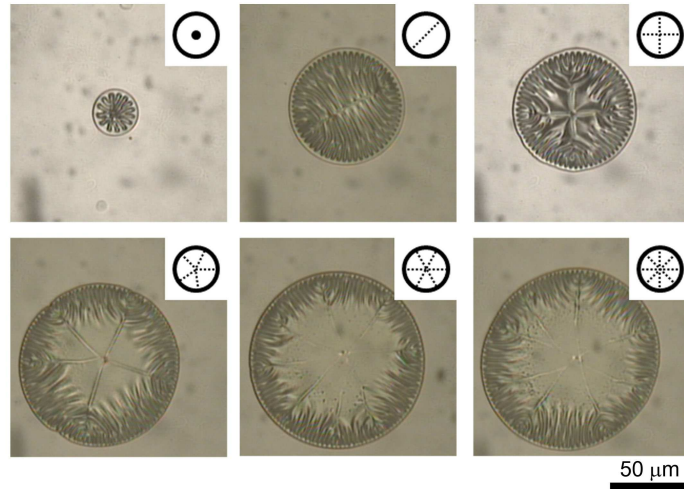


Figure 2.21: Optical micrographs of circular wrinkles according to the radius of occupation region.

according to the radius of circle, a spoke type or a 2-8 fold symmetric domain is produced through the shape of the convergence. It was observed that a circular pattern with large radius generally produces multi fold symmetry but it tends to obtain the non-uniformity of the wrinkles. It is interesting to note that under the condition of radius $> 50 \mu\text{m}$, the LCP layer near the center of circle obtain uniform surface. This can be understood from the fact that surface modulus is weakened by limitation of alignment of LC molecules of the LCP but a more close-packed structure (radius $< 50 \mu\text{m}$) prefers to be formed near the center of circle than in the edge of circle.

Based on symmetric wrinkles described above, we confirmed alignment of LC molecules of LCP by using the microscope under crossed polarizers. The first is wrinkling in line patterns (Figs. 2.22(a) and (b)) and the second is concentric pattern with wrinkles (Fig. 2.22(c)). As shown in Fig. 2.22(b), LC molecules of wrinkles are well aligned perpendicular respect to the line

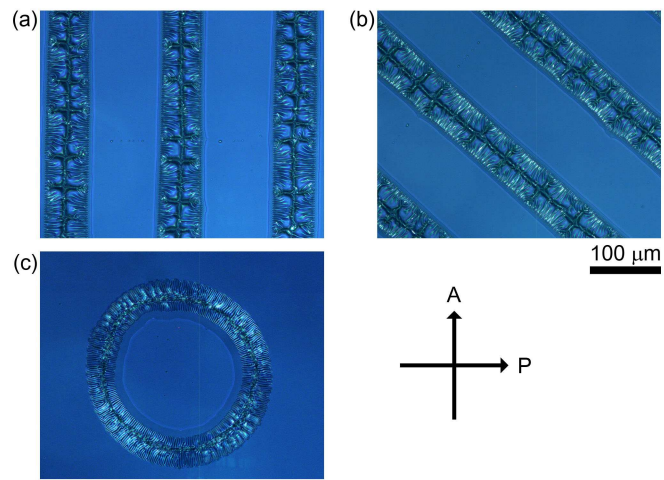


Figure 2.22: Optical micrographs of variety wrinkling pattern under crossed polarizers.

patterns. Also, concentric pattern have a radial LC alignment as shown in Fig. 2.22.

Chapter 3

Advanced Electro-optic Device Applications

Liquid crystals (LCs) are organic materials that are liquid but that show a certain degree of ordering (positional and/or orientational). With this definition, many materials can be classified as an LC, but the majority of LCs used in applications is of the nematic phase. Also, an LC technology has a major effect many areas of science and engineering, as well as device technology. Applications for this special kind of material are still being discovered and continue to provide effective solutions to many different problems. The most common application of LC technology is liquid crystal displays (LCDs). This field has grown into a multi-billion dollar industry, and many significant scientific and engineering discoveries have been made. In this chapter, we will focus on electro-optic device applications including display and optical component based on an LC. In addition, we discussed that effect of external influences, including surface anchoring, applied electric field, and optical field, is used to (re)orient of an LC in a certain way.

In turn, the LC then changes the light that is propagating through it.

3.1 Ferroelectric Electro-optic Device with Microchannel Structures

3.1.1 Introduction

Smectic liquid crystals (LCs) are an attractive subject for investigations due to their unique layered structure and variety of physical properties. The investigation of LCs behavior in thin oriented cells is interesting because the top and bottom substrates have significant influence on the macroscopic behavior of the LC in the cell [10, 52, 53]. Especially, in case of smectic LCs in the confined geometry, the competition between local surface interactions and global constraints imposed by the geometry of the self-assembled structures leads to layer deformation and the assembly of unique structures. Recently, a variety of groups are focused on the confined smectic LC on a curved space, geometrical constraints imposed by the curvature force the existence of areas where the director field cannot be defined, areas that are called topological defects [54, 55]. Because the layer deformations are considered to be anomalies in the smectic LC structure, general efforts have been directed at minimizing the deformations. However, deformed smectic layers possess unique rheological and optical characteristics, which could potentially be exploited to make novel optical devices. The prerequisite for

doing so would be the control of ordering and spatial distribution of the layer tilt, which had not been well addressed in previous studies. So, understanding and controlling orderings in confined LCs are important to many technological applications such as electro-optic (EO) devices.

Here we investigate for the first time the 3-dimensionally bound SmC* LCs (ferroelectric LCs, FLCs) in vertically aligned configuration and find a strong interplay of the confined geometry and the smectic layer deformation. Using a proposed model of propagation of smectic layer tilting and molecular ordering in the topographic confined cell structure, we show that this topographic confined geometry occur orthogonal anchoring forces and it is cause of structural instability in the smectic layer. It was found that orthogonal anchoring forces compete with each other and these play a primary role in the smectic layer deformation such as, spontaneous layer tilting and unique molecular ordering. Also, numerical simulations performed using a layer compression and dilation theory [56] within the molecular tilt angle formalism agree well with the experimental results. Moreover, using a deformed smectic layer in the confined geometry, vertically aligned deformed helix ferroelectric liquid crystal (VA-DHFLC) with low driving voltage is designed.

3.1.2 Fabrication of microchannel structure

To observe a smectic layer deformation in a confined geometry, we designed microchannels structure using replica molding technique which can easily duplicate the information, such as the geometrical shape and morphology, stored in a mater [57, 58]. Microchannels of poly(dimethylsiloxane)

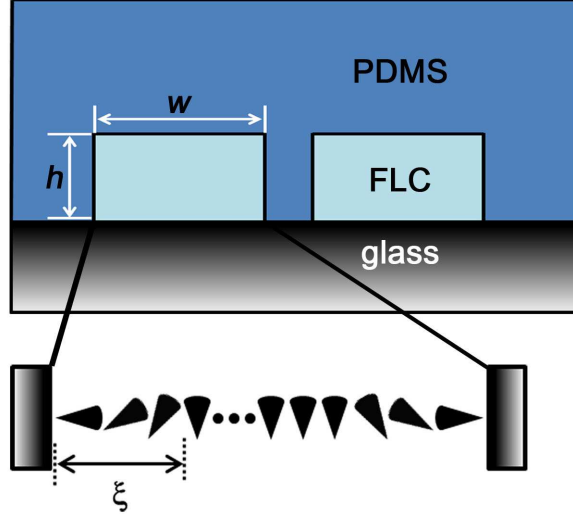


Figure 3.1: Schematic diagram of the confined FLC cell with a channel structure of PDMS. Here, w and h denote the width and height of the channel structure, respectively. The FLC in the rectangular channel is injected by capillary action.

(PDMS, Dow Corning) was poured onto the master mold, and subsequently cured at $85\text{ }^{\circ}\text{C}$ for 1 hour. The cured PDMS was then detached from the master mold and used for an upper substrate with lateral walls. Note that the PDMS material is homogeneous and capable of aligning the LC vertically [58]. The microchannels had a square cross-section and were $5\text{ }\mu\text{m}$ deep, 30 to $50\text{ }\mu\text{m}$ wide and 15 mm long. To produce a perfect tangential surface anchoring of SmC^* at the bottom substrate, a polyimide of AL00010 (Japan Synthetic Rubber Co.) was coated on the inner side of bottom substrate, followed by thermal curing at $160\text{ }^{\circ}\text{C}$ for 1 hour.

Our conceptual diagram of confined FLC cell was depicted in Fig. 3.1. A SmC^* phase material (ferroelectric liquid crystal, FLC), FLC-10855 (Rolic

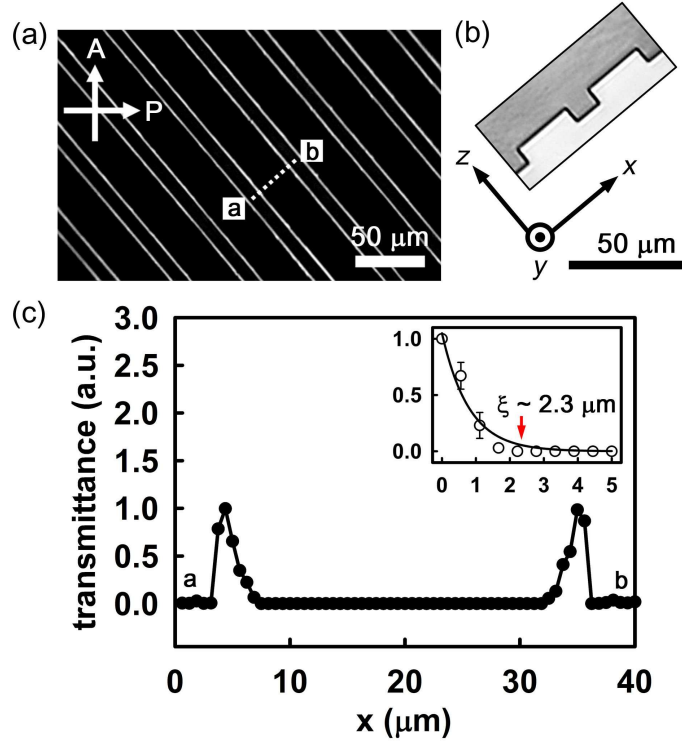


Figure 3.2: (a) Microscopic image of confined FLC cell under crossed polarizers. (b) The cross section of the PDMS channel structure. (c) Profile of light intensity along the x . Here, A and P represent the direction of analyzer and polarizer, respectively.

Technologies Ltd.), was filled into the rectangular channel with $30 \mu\text{m}$ in width (w) and $5 \mu\text{m}$ in height (h), by capillary action in the isotropic phase ($\sim 95 \text{ }^\circ\text{C}$). The spontaneous polarization, the cone angle, and the helical pitch of FLC-10855 are $P_s = 98 \text{ nC/cm}^2$, $\theta_0 = 38 \text{ }^\circ$, and $p < 0.2 \mu\text{m}$, respectively [59]. Smectic layers in a vertically aligned configuration are normally parallel to the surfaces and every smectic layer is uniformly formed by elongated molecules due to the anchorage of top and bottom substrates. However, in such a 3-dimensionally bounded FLC, the alignment of FLC

molecules is predominantly produced by the surface energy at the lateral walls as well as the substrates. This is clearly seen in the microphotographs (Optiphot2-pol, Nikon) as shown in Fig. 3.2(a). Under crossed polarizers (A and P), FLC molecules in the bulk region (the center of channels) behave as an optically isotropic medium and thus obtain the dark state. On the other hand, bright regions along the lateral walls are observed due to the presence of smectic layers deformation on a micrometer scale as homogeneous alignment. The deformation of smectic layers in a channel results from the competition with the surface anchoring of lateral walls and the bulk helical energies. As predicted above (see Fig. 3.1), we assumed that the FLC molecules prefer to be perpendicular to the walls near the lateral walls. These results can be satisfied only when the layers are tilt, preferably with a minimum elastic energy cost [60]. To explain this phenomenon, we measured the light transmission profile of the confined cell in cross section of the channel as shown in Fig. 3.2(c). The light intensity was given as a function of distance from the lateral wall ($x=0$). That is, show that FLCs near the lateral wall had a birefringence and different from the bulk regions as predicted above. This means that the surface interaction of lateral wall is preponderance than bulk helical nature in lateral wall vicinity. To describe the layer tilt in detail, we observe an enlarged profile that the light transmission decreased as the distance from the lateral wall increased as shown in the inset of Fig. 3.2(c). The characteristic length (ξ), width of the deformed layer region, of smectic layer is deduced as about $2.5 \pm 0.5 \mu\text{m}$ with the help of the measured transmittance. This length is consistent with the value of surface layer length ($\sim 2 \mu\text{m}$) in the previous work [61, 62]. Hence, the FLC molecules prefer to be anchored to the surface of lateral wall and

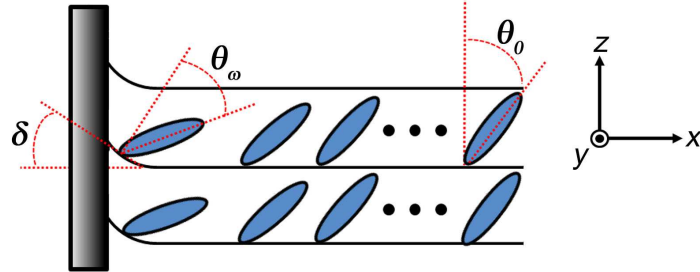


Figure 3.3: Schematic diagram of the propagation model of smectic layer deformation in the confined geometry.

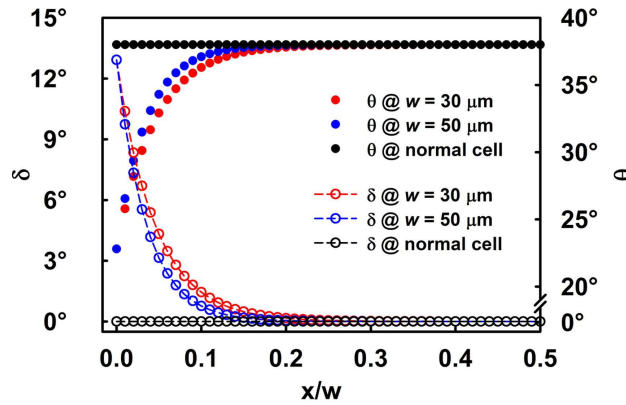


Figure 3.4: Variation of the layer tilt and molecular tilt angle with numerical factor of $D^2=1000$.

thus smectic layer tilted as shown in Fig. 3.1 for the $x < \xi$. These results indicated that smectic layers were followed well the topography of channel structure.

3.1.3 Theoretical description and modeling

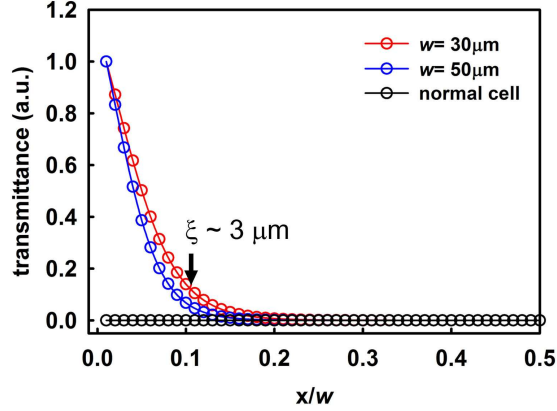


Figure 3.5: The transmission profiles according to the channel width.

Based on above results, we would like to discuss here model of propagation of smectic layer tilting and molecular alignment through the confined geometry. Using the material constants of the FLC-10855 and the geometrical parameters such as the width and height of the channels structure given above, we carried out numerical simulations of the spatial variations of the layer tilt (δ) and the molecular tilt (θ) in our confined cell by employing the layer compression and dilation theory [56,63] with modification. Figure 3.3 depicted the model of layer tilting with lateral wall having high anchoring strength. Due to the local surface anchorage of the lateral wall, the smectic layer was deformed. As a result, the θ varies along the x-axis as shown in Fig. 3.4. In the confined geometry, the θ and δ becomes modulated which reflects the interplay between orthogonal anchoring strengths near the lateral wall. On the other hand, without the confined structure (normal cell), the θ and δ remains uniform over the entire cell in a vertically aligned configuration. The θ of the deformed layer can be written as [56,63]

$$\theta = \theta_0 + (\theta_w - \theta_0) \left[\frac{1 - \cosh Q}{\sinh Q} \sinh Qx + \cosh Qx \right] - \frac{1}{2} P_s \cdot \mathbf{E} \frac{\cos 2\theta_0 \cos^2 \theta_0}{\sin \theta_0} \phi \quad (3.1)$$

subject to

$$\theta = \theta_w \text{ on } x = 0 \text{ and } x = w$$

where

$$Q = \sqrt{\frac{2D^2 \sin^6 \theta_0 \cos^2 \theta_0}{\cos^2 \theta_0}} \quad (3.2)$$

Here, $D^2(\propto w^2)$ is numerical factor related to the elastic constant, and ϕ represents the molecular twist angle. From the Eq. (3.1), the θ is there significant in determining an applied electric field (\mathbf{E}) and x . Taking into account the molecular tilt along the x-axis by the component of Qx , it found good agreement between their experimental observation of Fig. 3.2(c) and theoretical predictions for the confined configuration. While the δ decreased, the θ increased as distance from the lateral wall increased as shown in Fig. 3.4. Also, the smaller width of confine channels structure is, the more deformation occurs because of the large volume-surface ratio in the smectic layer [64]. In general, smectic layers tend to keep their thickness so that the dilative strain is induced along the direction normal to the smectic layer and it develops the layer modulation. This phenomenon is similar to the layer buckling in other layered systems [65]. This localized layer buckling tends to distort the un-buckled area in the operating region and induce a kind of mechanical instability as described previous research [66]. Note that, if this localized buckling is intensified further, continuum of the smectic layer between the buckled region and un-buckled region would not be sustained

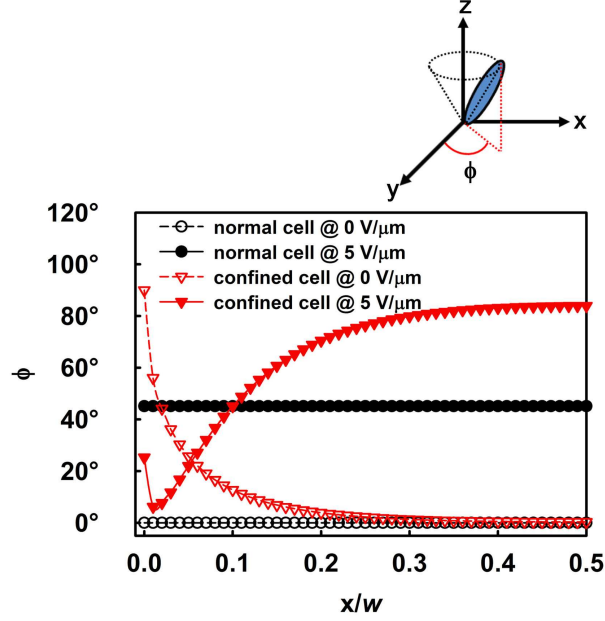


Figure 3.6: Profiles of molecular twist (ϕ) depend on the confined structure.

any longer. Moreover, according to Fig. 3.5, the light transmission near the lateral wall occurs by layer deformation ($\xi \sim 0.1w=3 \mu\text{m}$). This is consistent with the CCD images of light intensity profile in Fig. 3.2(c). These results demonstrate that deformation of smectic layer (near the lateral walls) could propagate across the x-axis and it affects the orientation of FLC molecules in a bulk region.

Next, we consider a ϕ that is the important factor of EO properties in FLC phase. The ϕ in the deformed layer can be expressed as

$$\phi = \cos^{-1}\left(-\frac{\tan \delta}{\tan \theta}\right) + \frac{1}{2} \frac{P_s \cdot \mathbf{E}}{\sin \theta_0} \left[\frac{(\theta - \theta_0)}{\cos \theta_0} - \frac{\sin \theta_0}{\cos \theta_0} \right] \quad (3.3)$$

For the profiles of the ϕ considered here it is reasonable to assume that these angles depend on δ , θ and \mathbf{E} from Eq. (3.3). Figure 3.6 describe

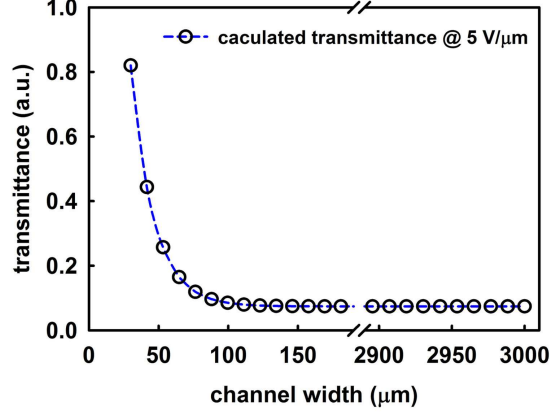


Figure 3.7: Variation of the transmission under a bipolar electric field of square wave form at 240 Hz as a function of channel width.

calculated profiles of the ϕ of the FLC with applied electric field at 0 and 5 $V/\mu\text{m}$. Although, the ϕ of normal (unconfined) cell remains uniform over the whole area regardless of the \mathbf{E} , the trend of confined ($w=30 \mu\text{m}$) cell changes according to the \mathbf{E} except in the vicinity of the lateral wall. This corresponds to the condition that the horizontal anchorage is preponderance than vertical anchorage at the boundary as shown in Fig. 3.3. Note that, if the anchoring strength of the lateral wall assumed to be infinite, ϕ is not going to change that but it is deemed to be physically unrealistic, therefore, weak anchoring ($W \sim 1 \pm 0.5 \times 10^{-6} J \cdot m^{-2}$) [67] could be introduced, possibly via a Rapini-Papoular type energy. Also, it was found that the tilted smectic layer near the lateral walls affect the Freedericksz transition voltage in the confined geometry. Clearly, the calculated transmittance with the contribution of smectic layer deformation was found to agree well with the width (w) of confined channel as shown in Fig. 3.7. This means that the ratio of ξ/w by confinement plays an important role on the EO properties

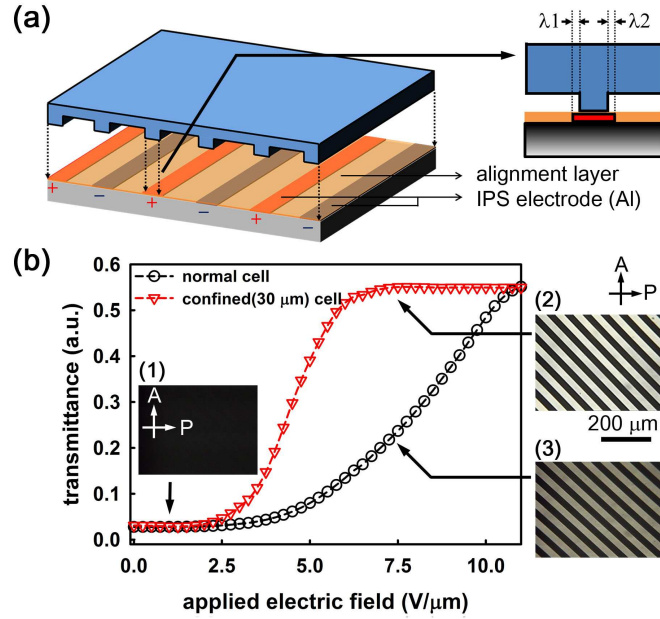


Figure 3.8: (a) Schematic diagram of confined VA-DHFLC cell. (b) The transmitted intensity under a bipolar electric field of square wave form at 240 Hz. The inset microphotographs, taken under crossed polarizers, correspond to the 0 and 7 V/ μm .

of FLCs.

3.1.4 Electro-optic properties

Within the framework of the above unique smectic layer deformation in the confined geometry, our confined cell is demonstrated in Fig. 3.8. The schematic diagram of the confined VA-DHFLC cell is depicted in Fig. 3.8(a). The rectangular channel structure of the PDMS is used as the top substrate as described above. The bottom substrate consists of a patterned

in-plane aluminum electrode and a homeotropic alignment layer. The periodic array of the PDMS walls perched on top side of in-plane electrodes as shown in right of Fig. 3.8(a). Here, λ_1 and λ_2 ($\sim 0.5 \mu\text{m}$) denote the left and right margin of the electrodes, respectively. Figures 3.8(b) shows the transmittance of the confined VA-DHFLC cell according to existence of the confined channel. A bipolar electric field of a square waveform at 240 Hz was applied to the cell under crossed polarizers. The confined VA-DHFLC cell has a high transmission at low electric field as compared with the normal cell as shown in Fig. 3.8(b). Moreover, high subthreshold slope was obtained and high contrast ratio of about 250:1 was achieved without any additional optical compensation. In addition, it may be interesting to note that the phenomenon in the unintended alignment breaking [68] of smectic layers, due to the vertical electric field, which occurs along the edge of the electrode was prevented by wall structures on the electrode. Because wall structures on in-plane electrodes were relieved vertical electric field. Each insets of Fig. 3.8(b) shows the microscopic image of the confined VA-DHFLC cell and normal cell under crossed polarizers at 0 and 7 V/ μm . We also measured the dynamic response to an unipolar electric field of a square waveform at 240 Hz [69]. It was found that the rising time $\tau_{on} = 185 \pm 5 \mu\text{s}$ and the falling time $\tau_{off} = 76 \pm 5 \mu\text{s}$ in the confined VA-DHFLC cell. These response times (of the order of 100 μs) are suitable for high-speed EO devices. It may be interesting to note that the reorientation of the FLC molecules from the unwound state to the helical state depends only on the helical power. However, the falling time is relatively faster than the rising time. This maybe shows that deformed smectic layers were helped that the unwounded FLC molecules back to the original helical state.

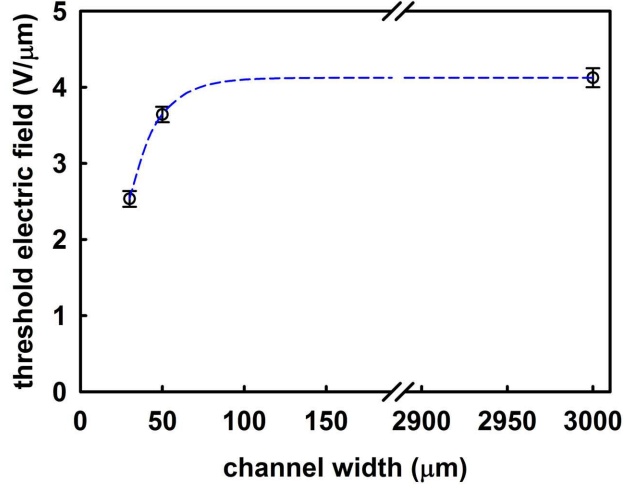


Figure 3.9: The threshold electric field as a function of the confined channel width.

Finally, Fig. 3.9 depicted that the variation of threshold electric field as a function of channel width. It was found that the layer deformation near the lateral walls affect the Freedericksz transition of the confined VA-DHFLC cell as mentioned above. The threshold electric field saturated at the channel width about $100 \mu\text{m}$. So, when the channel width larger than $100 \mu\text{m}$, EO properties of the confined FLC cell becomes to normal cell, in terms of threshold electric field. As well as surface-to-volume ratio is important, threshold electric field will be changed by cell thickness.

3.1.5 Summary

The propagation of smectic layer tilting and molecular ordering at lateral walls presented herein provides unique ordering mechanism within the confined geometry. We show that this topographic confined geometry occur orthogonal anchoring forces and it is cause of structural instability in the

smectic layer. Thus, it was found that orthogonal anchoring forces compete with each other and these play a primary role in the smectic layer deformation. Moreover, using a deformed smectic layer in the confined geometry, VA-DHFLC with high subthreshold slope and low driving voltage was designed.

3.2 Symmetric-viewing Liquid Crystal Display with Alternating Alignment Layers

3.2.1 Introduction

Liquid crystal displays (LCDs) based on the twisted-nematic (TN) mode have been widely used for flat panels in portable TVs and laptop computers due to their relatively simple and cost-effective manufacturing. The conventional TN mode resulting from the positive dielectric coupling of a nematic LC (NLC), however, has several disadvantages such as a limited contrast ratio, wavelength dependence, and narrow viewing characteristics. It is known that an inverse TN (ITN) mode [70, 71] shows high contrast because of the complete extinction under crossed polarizers, giving a dark state, in the initial homeotropic alignment of the LC molecules. Moreover, the ITN mode exhibits wavelength independence in the white state, but still suffers from asymmetric-viewing properties. Therefore, a new symmetric-viewing technology applicable for the ITN mode needs to be developed for high-performance LCDs.

In this section, a stamping-assisted rubbing (SAR) method [41, 72] of producing alternating alignment layers for a symmetric-viewing ITN-LCD with multidomains was developed. A patterned protective layer of a fluorinated acrylate polymer was transferred onto the first rubbed alignment layer prepared on a substrate by stamping. The fluorinated acrylate polymer covered the first alignment layer during the second rubbing process, which promoted the vertical alignment of the LC molecules. The regions

covered with the patterns of the protective polymer layer preserved the initial alignment generated through the first rubbing process. As shown in Fig. 3.10, the LC cell was assembled such that the rubbing directions on the two substrates were perpendicular to each other, so that four different ITN domains corresponding to two clockwise and two counterclockwise directions were produced. Both splay and twist deformations were involved in the four domains (4Ds). As a consequence, the twist directors of two adjacent domains were different from each other [73].

3.2.2 Schematic and operation principles

The basic structure and operation principles of the developed 4D ITN-LC cell are shown in Fig. 3.10. The inner surfaces of the two substrates were treated to promote the initially homeotropic alignment of the LC molecules [74]. An NLC material with a negative dielectric anisotropy was placed between the two rubbed substrates. Note that a certain amount of molecular chirality was introduced to generate a desirable amount of natural twist in the presence of an applied voltage (V). In the dark state, the homeotropically aligned NLC cell blocked the incident light under crossed polarizers. When a voltage above the Fredericks threshold (V_{th}) was applied, the LC molecules tended to orient along the direction perpendicular to the applied electric field, and twist distortions of the LC occurred in an activated bright state along different directions in the alternating rubbed domains. For $V > V_{th}$, the incident light passed through the crossed polarizers, and the resultant light transmission varied with the magnitude of the applied voltage. The directions of the LC molecules in the dark and bright

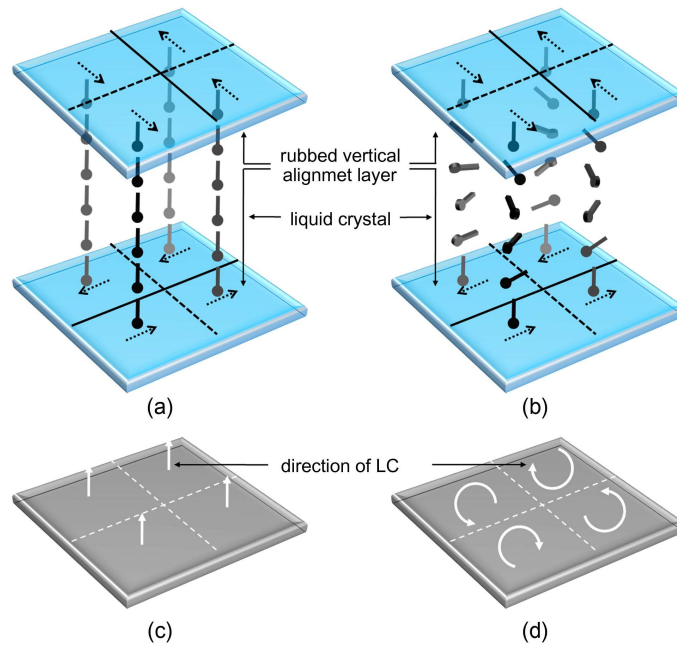


Figure 3.10: Schematic diagram and operation principle of the 4D ITN-LC cell: the alternating rubbing directions and the LC alignment (a) under no applied voltage (a dark state) and (b) in the presence of an applied voltage (a bright state) and the directions of the LC molecules (c) in the dark state and (d) in the bright state.

states are schematically shown in Fig. 3.10(c) and (d), respectively.

3.2.3 Fabrication process of alternating alignment layers

The SAR method of producing alternating alignment is shown in Fig. 3.11. The vertical-alignment layer of polyimide (PI) (AL60702, Japan Synthetic Rubber) was first spin-coated onto a substrate and then rubbed uni-

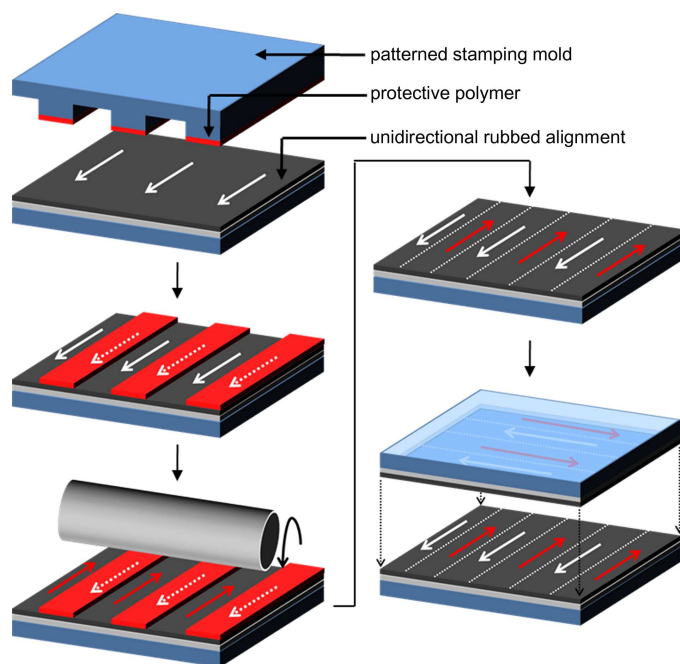


Figure 3.11: SAR technique for achieving the alternating alignment of LC: a stamping process involving transferring the protective layer of a fluorinated acrylate polymer onto the first rubbed alignment layer, the substrate with the protective layer on top of the first alignment layer, the second rubbing process on the first alignment regions that are not covered with the protective layer, the fabricated bidirectional alignment layer, and two substrates assembled such that the rubbing directions are perpendicular to each other.

directionally to promote the vertical alignment with a uniform pre-tilt of the LC molecules. For the second rubbing process along the direction opposite to the first rubbing direction, a protective layer (Novec EGC-1700, Sumitomo 3M) prepared on a patterned stamping mold of polydimethylsiloxane (PDMS, GE silicones) was transferred onto the first rubbed PI by stamping and was subsequently cured at room temperature. Note that

EGC-1700, a fluorinated acrylate polymer dissolved in a hydrofluoroether solvent, did not chemically affect the alignment layer. The second rubbing process was then performed on the regions that were not covered with the protective layer along the direction opposite to the first rubbing direction. The substrate was rubbed five times to ensure the saturation of the tilt bias angle [45]. The protective layer was finally dissolved in the hydrofluoroether solvent (Novec HFE-7100, Sumitomo 3M), and alternating alignment was readily achieved. For the fabrication of the ITN-LC cell, two substrates with an alternating alignment layer were assembled such that the rubbing directions on the two substrates were perpendicular to each other. The cell thickness was maintained using 5 μm thick glass spacers. The LC (MLC-6608, Merck Ltd) with a negative dielectric anisotropy was injected into the cell by capillary action at room temperature. The birefringence and the dielectric anisotropy of MLC-6608 were $\Delta n = 0.083$ and $\Delta\epsilon = -4.2$, respectively. A square-wave voltage at a frequency of 1 kHz was applied to the ITN-LC cell to measure the electro-optical (EO) transmission and the response times. The measurements were carried out using a digitizing oscilloscope (WaveRunner 6030, Lecory) and a light source of a He-Ne laser with the wavelength of 632.8 nm at room temperature.

3.2.4 Electro-optic properties

The microscopic textures of the ITN-LC cell with 4Ds due to the alternating alignment in Fig. 3.12 were observed with a polarizing optical microscope (Optiphot2-pol, Nikon) under crossed polarizers at different applied voltages. In the absence of an applied voltage, the LC molecules were

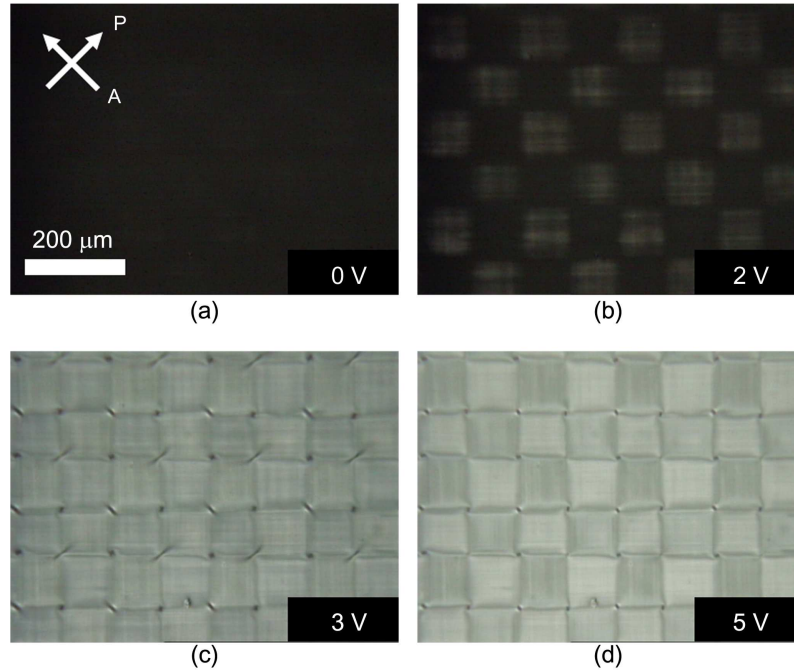


Figure 3.12: Microscopic textures of the 4D ITN-LC cell with two alternating alignment layers observed under crossed polarizers at different voltages: (a) 0V; (b) 2V; (c) 3V; and (d) 5V.

vertically aligned, as shown in Fig. 3.12(a). Thus, under crossed polarizers, no light propagated, and a completely dark state was obtained. At 2V, which was above V_{th} , the transmission slightly increased, as shown in Fig. 3.12(b). At 3V, the LC molecules were partially twisted, and the transmission further increased, as shown in Fig. 3.12(c). At a relatively high voltage of 5V, the LC molecules were mostly twisted in the plane of the substrate, and a bright state was obtained, as shown in Fig. 3.12(d). It should be noted that four disclination lines enclosing each square pattern separated the four different domains. The adjacent domains were the oppositely twisted do-

mains. This can be well understood from Fig. 3.12(d). The small difference in brightness observed in Fig. 3.12(d) indicates that the first and second rubbing processes were not identical. Due to the physicochemical nature of the PI that was used, the LC alignment after the first rubbing seemed dominant over that after the second rubbing. Meanwhile, as the thickness of the fluorinated acrylate polymer was at most 100 nm (much less than the cell thickness of 5 μm and the wavelength of visual light, typically 500 nm), it is negligible for the brightness difference arising from the cell thickness difference. As a consequence, a difference in brightness was observed. Moreover, non-uniformity in a single domain often appeared.

Figure 3.13 shows the normalized EO transmission and the dynamic response of the 4D ITN-LC cell in the presence of a bipolar voltage in a square-wave form at 1 kHz. The EO properties were measured as a function of the applied voltage under crossed polarizers. Irrespective of the small difference in brightness among the 4Ds, as shown in Fig. 3.13(a), the EO curve shows continuous gray scales, and the contrast ratio was found to be about 50:1. In Fig. 3.13(b), the black and gray curves represent the EO response of the ITN-LC cell and the applied voltage, respectively. It was found that the rising time was $\tau_r = 28 \pm 2$ ms and that the falling time was $\tau_f = 25 \pm 2$ ms at an applied voltage of 4V, without any driving compensation. This switching speed range will be further improved using a fast-response LC material for high-speed applications.

The viewing angle characteristics of the ITN-LC cell, measured at 4V using a spatial photometer (EZ contrast 160R, ELDIM), are shown in Fig. 3.14. A conventional ITN-LC cell with a single domain exhibits asymmetric and relatively narrow viewing properties, as shown in Fig. 3.14(a).

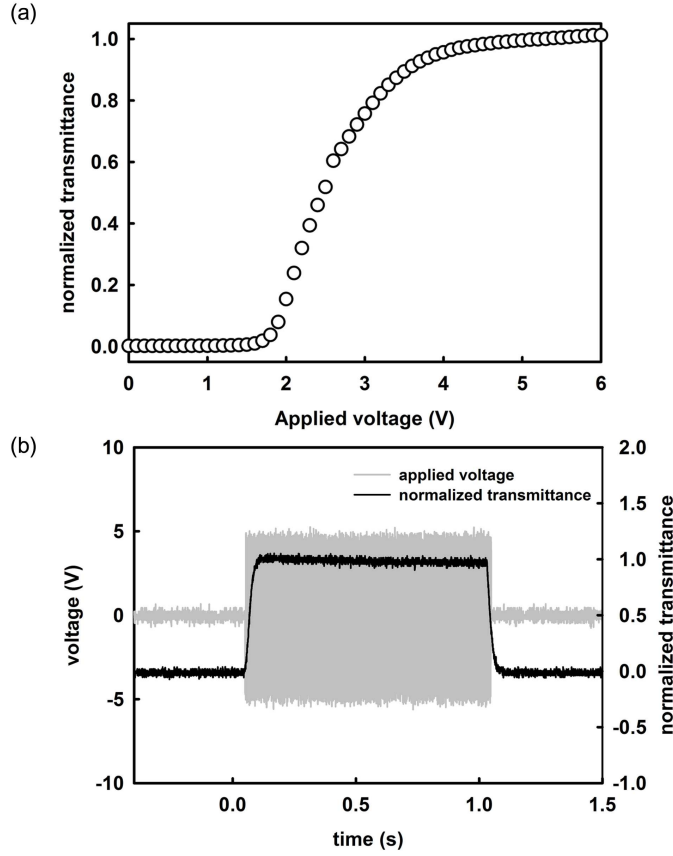


Figure 3.13: EO characteristics of the 4D ITN-LC cell: (a)EO transmittance and (b) dynamic response as a function of the applied voltage in the square-wave form. The rising and falling times ($\tau_r = 28$ ms and $\tau_f = 25$ ms) were measured at 4V. The dark and gray curves represent the dynamic response and the applied voltage, respectively.

In contrast, the 4D ITN cell without any compensation film showed quite symmetric-viewing properties with respect to the axes of the polarizers in the vertical and horizontal directions. This is attributed to the optical compensation among the four differently twisted domains produced by the

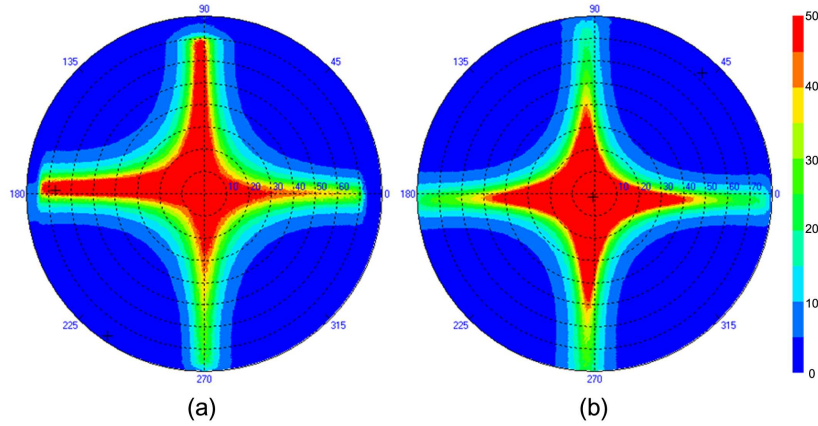


Figure 3.14: Iso-contrast contours: (a) a conventional ITN-LC cell and (b) the 4D ITN-LC cell with two alternating alignment layers.

alternating alignment in the ITN geometry, as shown in Fig. 3.10(d).

3.2.5 Summary

Demonstrated herein was a symmetric-viewing ITN-LCD with 4Ds due to two alternating alignment layers produced via SAR. With the help of an inert protective layer of a fluorinated acrylate polymer, the second rubbing process was successfully employed without causing any mechanical and chemical damage to the first rubbed alignment layer. The ITN-LC cell with 4Ds presented here showed continuous gray scales with good linearity as well as the symmetric-viewing characteristics that are needed for high image quality. The SAR approach is basically mask-free and has a potential for the simple and cost-effective fabrication of large ITN-LCDs.

3.3 2D/3D Convertible Display with In-cell Undulated Electrode

3.3.1 Introduction

Among a variety of electrically tunable lenses based on an LC, spherical LC lens structures are most extensively studied [75–78]. Of particular interest is a convertible lenticular LC array which serves as one of the essential components for realizing 2-dimensional (2D)/3-dimensional (3D) convertible displays [79–81]. In order to obtain the characteristic of the flat-to-lens conversion, either a homogeneous electric field in the LC layer with a nonuniform cell gap [82] or an inhomogeneous electric field in the LC layer with the uniform cell gap [83], for example, the in-plane switching (IPS) method [80] is necessarily employed. The IPS approach allows, in principle, a simple scheme of modulating the EO effect of the LC but it suffers intrinsically from the existence of inactive regions of the LC layer on the electrodes and in the vicinity of the substrate with no electrodes. In another case, the use of an extra solid lens involves a complex fabrication process and a bulky structure of an LC lens array [84]. Note that the resolution format of a lenticular LC array will govern primarily the image quality of the 2D/3D display.

3.3.2 Schematic and operation principles

In this section, we demonstrated a convertible lenticular LC array using an index-matched planarization layer on a periodically undulated electrode allowing the flat-to-lens conversion over the entire area of the LC cell through the electric field modulation. It was found that the in-plane component of the modulated electric field plays a primary role in the flat-to-lens effect while the out-of-plane component contributes to the anchoring enhancement of the LC molecules in the surface layer. The contribution of the out-of-plane electric component to the focusing effect in a lenticular LC array has not been described previously in the case of an inhomogeneous electric field. The periodically modulated electric field produces the periodic LC distortions on a planar surface along the direction perpendicular to the electrode undulation. As a result, our LC device gives rise to the flat-to-lens capability over the whole region in contrast to the IPS case. Numerical simulation results, obtained using a relaxation method [85] within the framework of the elasticity formalism [86], agree well with the experimental results.

The schematic diagram of our convertible lenticular LC array is depicted in Fig. 3.15. An indium-tin-oxide (ITO) coated glass substrate is used as the top substrate. The bottom substrate consists of a planarization material (PM), an undulated ITO electrode, and a lenticular cast on a glass substrate. The key requirement is that the refractive index of the PM should be equal to that of the lenticular cast for index matching. The inner surfaces of the two substrates are spin-coated with polyimide (PI), baked, and rubbed unidirectionally to promote the planar alignment of the LC.

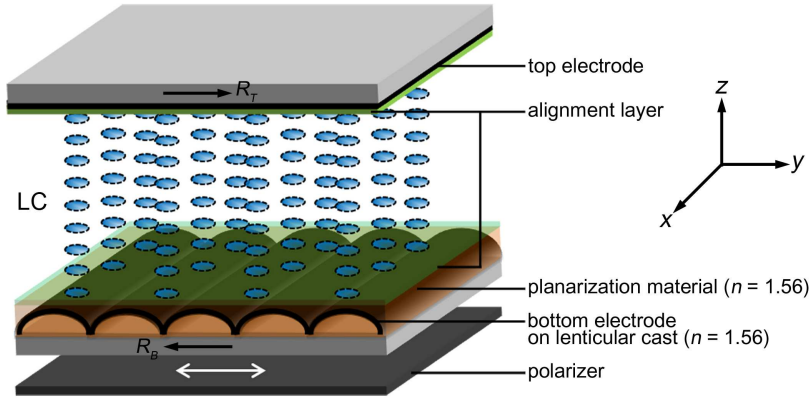


Figure 3.15: The schematic diagram of convertible lenticular LC lens structure with a undulated electrode, giving the lenticular lens effect, in a planar configuration. Here, R_T and R_B denote the rubbing direction on the top substrate and that on the bottom substrate, respectively.

The surface pretilt angle at the rubbed substrate was measured to be about 2° , eliminating the reverse-tilt at the boundary. The rubbing direction on the top substrate and that on the bottom substrate are denoted as R_T and R_B , respectively.

Figures 3.16(a) and 3.16(b) represent the operational principles of our lenticular LC array. When the optic axis of the LC layer coincides with the polarization of an input beam through a linear polarizer (see, the white arrow in Fig. 3.15), the field-off state corresponds to an optically uniform state with no LC distortions as indicated by the thick red arrows in Fig. 3.16(b). In the field-on state, the LC distortions are periodically modulated along the y -axis due to the undulated electrode. This means that the effective refractive index (n_{eff}) becomes periodically modulated and the lenticular lens effect is produced. Note that in contrast to the IPS case, there are no inactive regions of the LC layer for the optical modulation in

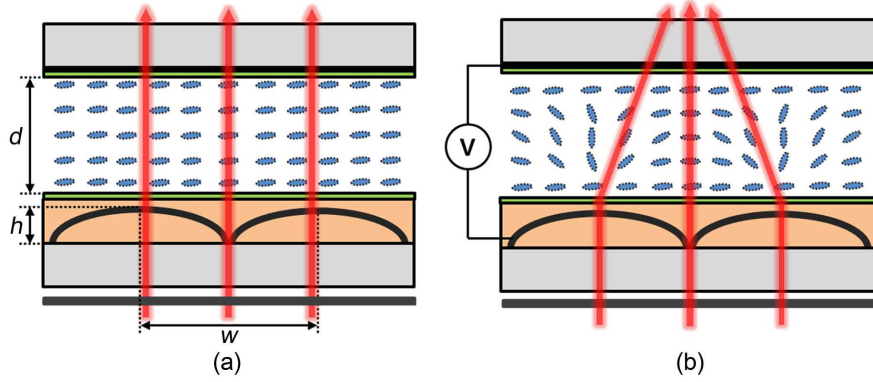


Figure 3.16: Schematic diagrams showing the operational principles of our lenticular LC lens: the optical states under (a) no applied voltage and (b) an applied voltage. Here, w and h denote the width and height of a lenticular cast, respectively. The cell gap is d .

our case.

3.3.3 Fabrication process of convertible lenticular LC lens

For buried electrode in bottom substrate, as shown in Figs. 3.17(a)-(d), a lenticular cast of a ultraviolet (UV) curable polymer (NOA65, Norland Products Inc.) was produced on a glass substrate using a mold of poly(dimethylsiloxane) (PDMS, GE silciones) and irradiated with UV light for 10 minutes [78,82]. Subsequently, a 100 nm-thick ITO electrode was deposited onto the lenticular cast by thermal evaporation. The width (w) and the height (h) of the lenticular cast were 25 and 7.2 μm , respectively. The PM was finally spin-coated on the undulated electrode for planarization.

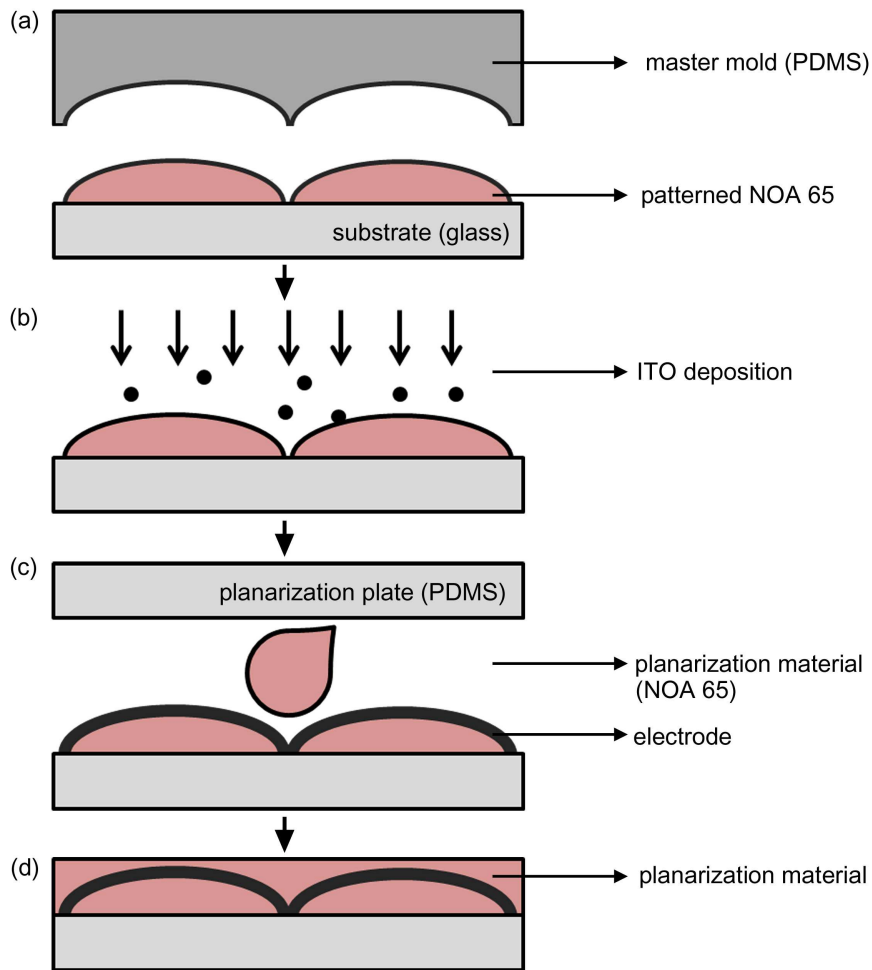


Figure 3.17: The fabrication process for the undulated electrodes: (a) an imprinting process of producing periodic lenticular casts of a UV curable polymer (NOA65) on a glass substrate, (b) ITO electrode deposition onto the lenticular patterns of NOA65, (c) coating of the PM (NOA65) on the undulated electrodes for planarization, and (d) the fabricated substrate with the buried electrode.

An image of a scanning electron microscope (SEM) and the surface profile of the undulated electrode on the lenticular cast are shown in Fig. 3.18(a).

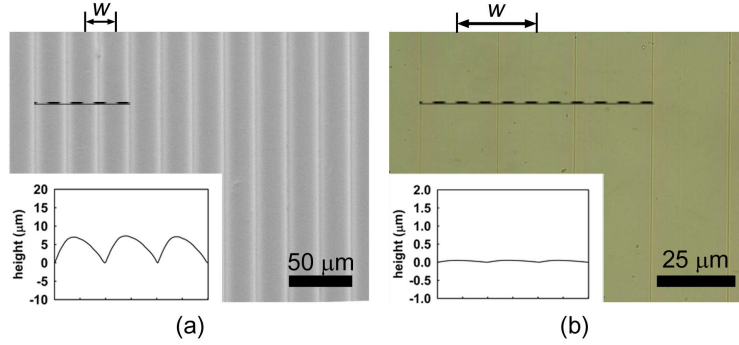


Figure 3.18: (a) The SEM image of an undulated electrode, (b) the microscopic image of the substrate with the undulated electrode, and the insets in (a) and (b) correspond to the surface profiles before and after planarization. Here, w denotes period of lenticular cast on the bottom substrate.

Due to index matching of the lenticular cast with the planarization layer, the bottom substrate is optically uniform as shown in Fig. 3.18(b). A commercial PI (RN-1199A, Nissan Chemical Industries, Ltd.) for the homogeneous alignment and a nematic LC (ZLI-4151-000, Merck Ltd.) with a positive dielectric anisotropy were used. The material parameters [87] of ZLI-4151-000 are three elastic constants, $k_1 = 1.15 \times 10^{-11}$ N, $k_3/k_1 = 1.62$, $k_3/k_2 = 2.90$, and the dielectric anisotropy $\Delta\epsilon = 10.6$ ($\epsilon_{\parallel} = 15.0$). The ordinary and extraordinary refractive indices are $n_o = 1.51$ and $n_e = 1.66$, respectively. The cell gap (d) was maintained using 20 μm -thick glass spacers and the LC was injected by capillary action. Figures 3.19(a) and 3.19(b) show the microscopic images of the lenticular LC cell observed when the crossed polarizers (A and P) make an angle of 45° and 0° with respect to the rubbing direction (R), respectively. Clearly, the LC was well aligned homogeneously on the substrate with the undulated electrode after planarization. A square-wave

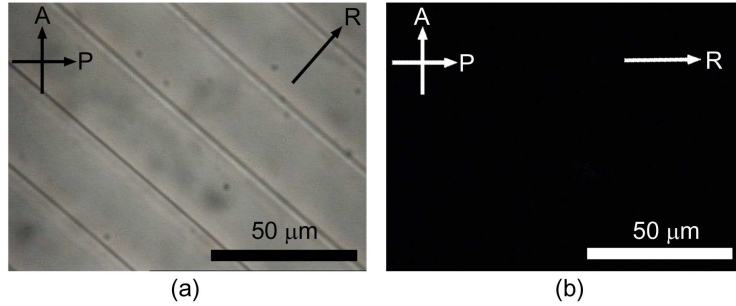


Figure 3.19: The microscopic textures of the lenticular LC cell observed when the crossed polarizers (A and P) make an angle of (a) 45° and (b) 0° with respect to the rubbing direction (R). Here, A and P denote the crossed polarizers.

voltage at the frequency of 1 kHz was applied to the our lenticular LC lens to measure the EO properties. The measurements were carried out using a polarizing optical microscope (Optiphot2-Pol, Nikon) and a light source of a He-Ne laser with the wavelength of 543.5 nm at room temperature.

3.3.4 Electro-optic properties

The graded index (GRIN) effect of our lenticular LC cell observed from microscopic textures at several different voltages is shown in Fig. 3.20. The applied voltage was varied from 5 V to 25 V at an interval of 5 V. The microscopic textures were observed when one of the crossed polarizers makes an angle of 45° with respect to the rubbing direction. Under no applied voltage, a uniform state is obtained. As the applied voltage increases, the LC molecules are reoriented according to the electric field gradient generated by the undulated electrodes as shown in Fig. 3.16(b) and the retardation

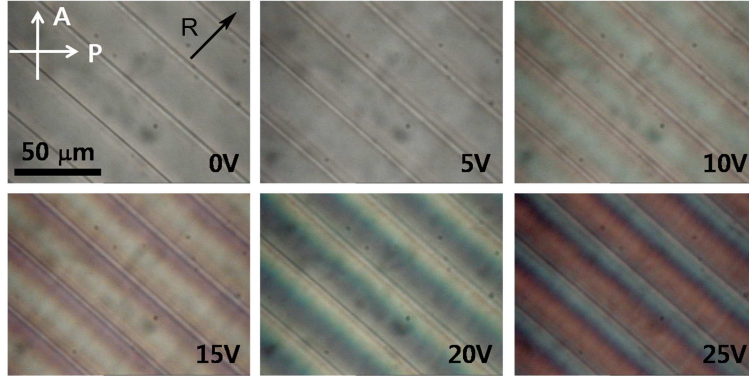


Figure 3.20: The microscopic textures showing the GRIN effect of our lenticular LC cell under crossed polarizers at several different bipolar voltages at 1 kHz in square wave form. The symbols of P and A are the polarization directions of the polarizer and the analyzer, respectively.

difference across each lenticular structure increases. This is what we observed in Fig. 3.20 at different applied voltages. As shown in Fig. 3.20, the changes of both the focusing behavior and the color were appeared due to the spatial variations of the effective refractive index n_{eff} (or the phase retardation) with increasing the applied voltage above 10 V in the range of the applied voltage we studied. We first examine the tunable focusing properties of our lenticular LC lens using an array of 2D circular ($10 \mu\text{m}$ in diameter) patterns as an input image. The schematic diagram for the experiment was depicted in Fig. 3.21(a). The measurements were carried out at room temperature using a polarizing optical microscope (Optiphot2-Pol, Nikon) and a He-Ne laser with the wavelength (λ) of 543.5 nm. The input beam was linearly polarized along the rubbing direction. As shown in Fig. 3.21(b), under no applied voltage, the image of the circular pattern observed with with a charge-coupled device (CCD) is the same as the original

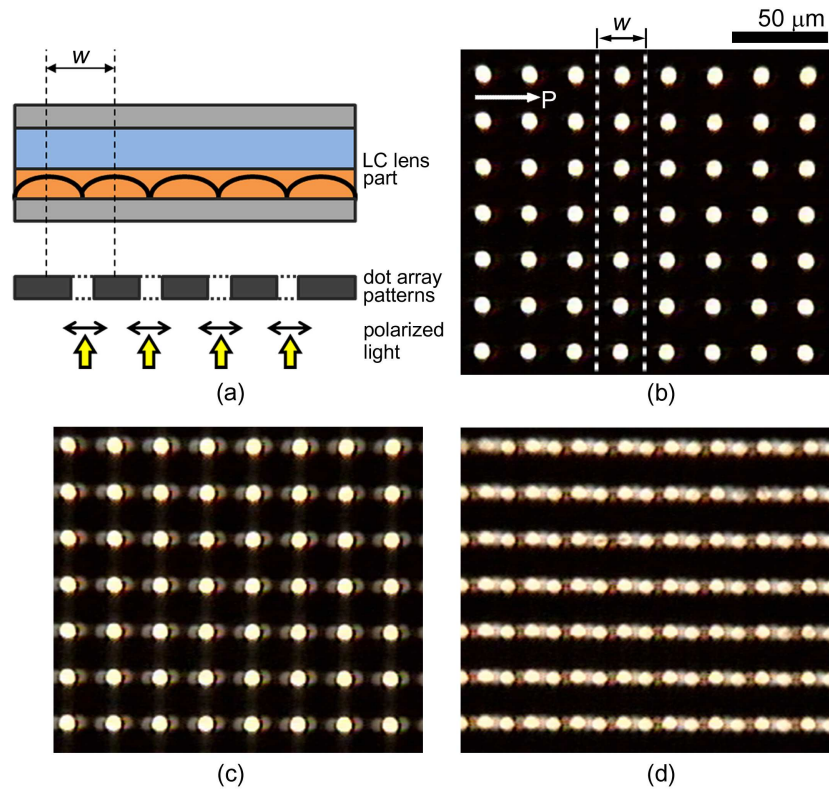


Figure 3.21: The tunable focusing capability of the lenticular LC lens: (a) the schematic diagram of the experiment using an array of circular patterns as an input image and the microscopic images of the circular patterns observed through the lenticular LC array at an applied voltage of (b) 0 V, (c) 5 V, and (d) 10 V, respectively.

pattern whose diameter is $10 \mu\text{m}$. This means that the LC cell behaves as an optically uniform plate and no lens effect occurs. At the applied voltage of 5 V, the image of the circular pattern was blurred as seen in Fig. 3.21(c) due to the GRIN effect resulting from the periodic distortions of the LC by the undulated electric field. At 10 V, two images (or two viewing points) were observed in Fig. 3.21(d) since the focal length was increased. A simple

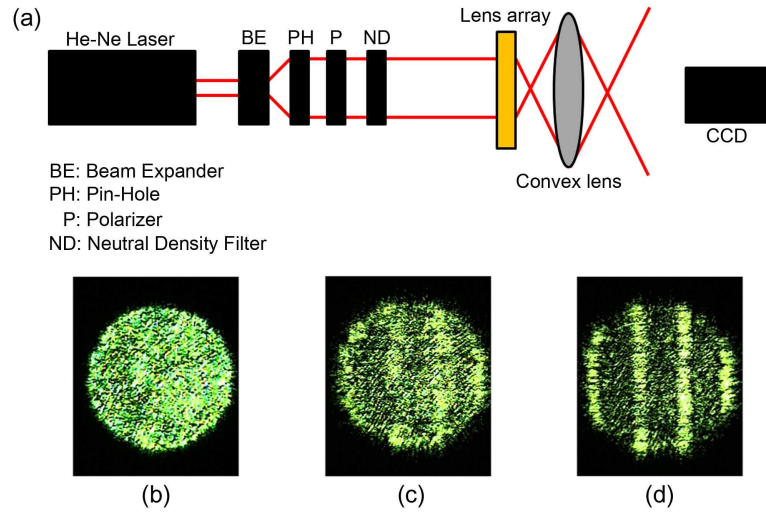


Figure 3.22: The tunable focusing capability of the lenticular LC lens: (a) an optical setup for measuring the ray focusing properties of our lenticular LC lens and the CCD images of a collimated laser beam in the focal plane at an applied voltage of (b) 0 V, (c) 5 V, and 10 V, respectively.

optical setup for measuring the ray focusing properties of the input through the our lenticular LC lens is illustrated in Fig. 3.22(a). The ray focusing properties of the lenticular LC lens under different applied voltages were seen from the images [Figs. 3.22(b)-(d)] of a collimated laser beam in the focal plane. The electrically tunable focal length of the lenticular LC array was measured as a function of the applied voltage by focusing the blurred image. The experimental results will be discussed together with numerical simulations below.

Using the material constants of the LC and the geometrical parameters such as the width and height of the lenticular cast given above, we carried out numerical simulations of the spatial variations of n_{eff} and the resultant

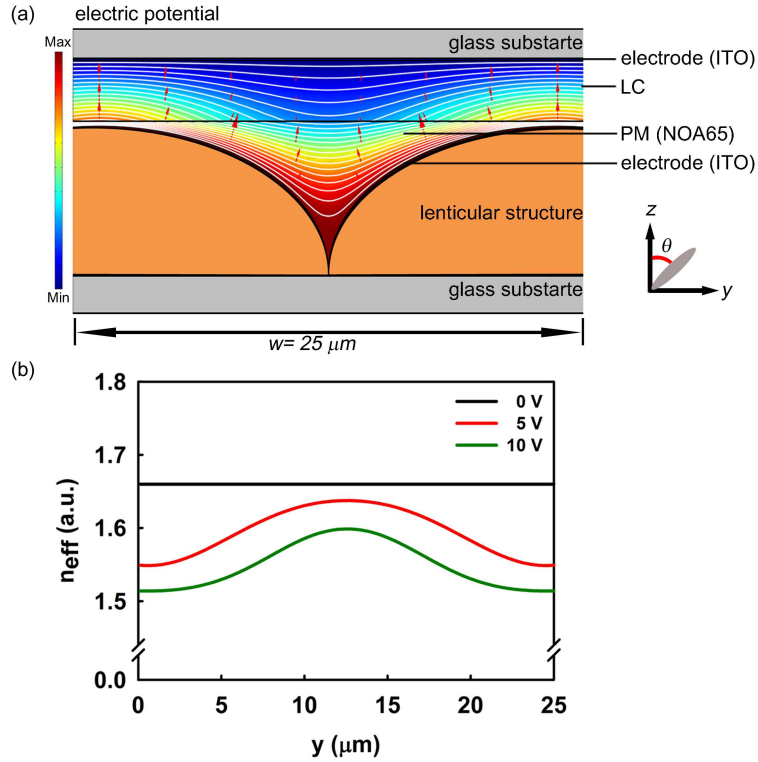


Figure 3.23: Numerical simulations of (a) the equipotential lines, (b) the spatial variations of the effective refractive index at 5 V and 10 V with E_y (solid lines) and without E_y (dashed lines).

focal length variations of our convertible lenticular LC array by employing both a relaxation method [85] in the elasticity theory and a commercial program, FemLabTM (COMSOL). A typical example of the equipotential lines at 7 V obtained using the COMSOL program was shown in Fig. 3.23(a). The white lines and red arrows represent the equipotential lines and the electric field directions, respectively. It should be noted that in the case of an inhomogeneous (or non-uniform) electric field, either the transverse component or the longitudinal component contributes to the suppression of the LC

distortions as if it would enhance the LC anchoring in the surface layer [88]. In our lenticular LC array with the undulated electrode, the y -component of the electric field (E_y) is expected to enhance the LC anchoring in the surface layer, meaning that there exists the interplay between the z -component of the electric field (E_z) and E_y in the LC distortions. More specifically, denoting the LC director as $(0, \sin \theta, \cos \theta)$, the dielectric energy density can be then written as $-\Delta\epsilon E^2(\sin \theta \sin ky + \cos \theta \cos ky)^2$ provided that $E_y = E \sin ky$ and $E_z = E \cos ky$. Here, θ represents the tilt angle of the LC director with respect to the z -axis and the undulation period of the electrode $k = 2\pi/w$. The term of $-\Delta\epsilon E^2(\sin^2 \theta \sin^2 ky + 2 \sin \theta \cos \theta \cos ky \sin ky)$ resulting from non-zero E_y component was found to suppress the director distortions in the out-of-plane. Such contribution has not been considered previously in a uniform LC layer under the undulated electric field.

The effect of E_y on n_{eff} is shown in Fig. 3.23(b). The variations of n_{eff} along the y -axis become much enhanced by E_y , particularly, in the high-field regime. Under no applied voltage, n_{eff} remains uniform over the entire LC cell in a planar configuration. In the presence of an applied voltage, n_{eff} becomes modulated in the symmetry which reflects the shape of the lenticular cast. This is consistent with the CCD images shown in Fig. 3.22. Figure 3.24 shows both the experimental and simulation results for the focal length variations of our lenticular LC array with the applied voltage. Clearly, the calculated focal length with the contribution of E_y was found to agree well with the experimental results. This means that the anchoring enhancement by the E_y component plays an important role on the EO properties of the LC. In our simulations, the anchoring energy of the PI alignment layer alone was treated as a parameter to be determined from

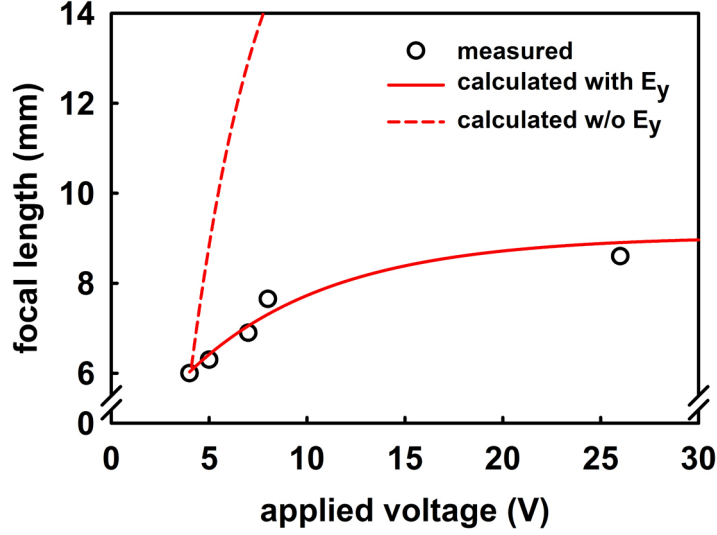


Figure 3.24: The focal length variations of our lenticular LC array with the applied voltage. The experimental results were represented the circles. The solid and dashed lines denote the calculated focal lengths with and without the contribution of E_y , respectively.

the best fit of the experimental data to the calculated focal length in Fig. 3.24. The anchoring energy was determined to be $6.6 \times 10^{-6} J/m^2$, which is consistent with the previous result [53]. Our LC lens cell is convertible from an optically uniform plate (a flat surface) to a lenticular array with the focal length ranging from about 5 mm to 10 mm in the presence of an applied voltage. In general, both the in-plane and the out-of-plane components of an external electric field should be taken into account for the reorientation of the LC director in the case of an inhomogeneous electric field.

3.3.5 Summary

We demonstrated that a delicate interplay between the in-plane and out-of-plane components of an inhomogeneous electric field plays a critical role on the flat-to-lenticular lens conversion in a homogeneously aligned LC cell. The framework of the refractive index-matching between the lenticular cast and the PM layer provides a practical route to construction of a variety of electrically tunable, convertible LC devices in a planar geometry. Finally, our concept of using the electric field modulation on a flat surface should be directly applicable for constructing 2D/3D convertible displays and optical focusing elements in photonics. Moreover, the fine pitch of $25\ \mu\text{m}$ in our lenticular LC array is suitable for the high-resolution image in 3D displays.

Chapter 4

Biomimetic Application

4.1 Concept of Artificial Iris

The colored part (the iris) of the human eye is very important part and it regulates the amount of light, like that of a camera's shutter through the control of aperture ratio, which the pupil lets in the eye. However, iris defects resulting from damage to the iris or congenital defects, such as aniridia (or partial aniridia) and albinism, can compromise visual quality, with severe glare and loss of contrast sensitivity. Moreover, partial or total loss of the eyes in a human being have trouble with not only the functional loss of sight, but also his/her self-esteem and social intercourse. Recently, the surgical implantation of artificial iris in patients with anatomic or functional iris deficiencies is nearly mature and successful. These technologies have also been developed for the surgical management of aniridia [89–92]. These artificial irises are limited by the immobility of the pupil, whereas these are similar to the real human iris apparently. Hence their help to

anatomic patients is limited. In order to obtain the characteristic of regulation of the incident light, either polymer-dispersed liquid crystal [93] or liquid crystal cell [94] is necessarily employed. These approaches allow, in principle, a good controllability of amount of incident light but it suffers intrinsically from the use of an extra control circuits involves a complex fabrication process and a bulky structure.

In this chapter, we present novel concept of artificial iris that provides a self-regulation of light intensity without peripheral devices. And spoke pattern formation like radial muscles of human eye where a liquid crystalline polymer (LCP) is used as an anisotropic (radially) patterned material. In addition, this biomimetic artificial iris is anatomically as well as functionally close to human eyes with unique regulation mechanism. This photoreaction-based approach allows analogy and concurrent control of the amount of light by ambient light intensity. The amount of light to retina (self-regulation of light intensity) is reversibly controlled through molecular bond reformation with irradiation of light source.

Our concept of light intensity regulation of artificial iris is illustrated in Fig. 4.1. The iris of the human eyes is a contractile structure, consisting of two layers such as the front pigmented fibrovascular tissue known as a stroma and pigmented epithelial cells under the stroma [95,96]. The stroma connects to a circular muscles group called the sphincter muscle, which contracts the pupil in a circular motion, and a set of radial muscles called the dilator pupillae which pull the iris radially to enlarge the pupil, pulling it in folds. This anterior surface projects as the radial muscles as shown in Fig. 4.1(a). The high pigment content blocks light from passing through the iris to the retina. Fig. 4.1(b) shows the operation principle of human

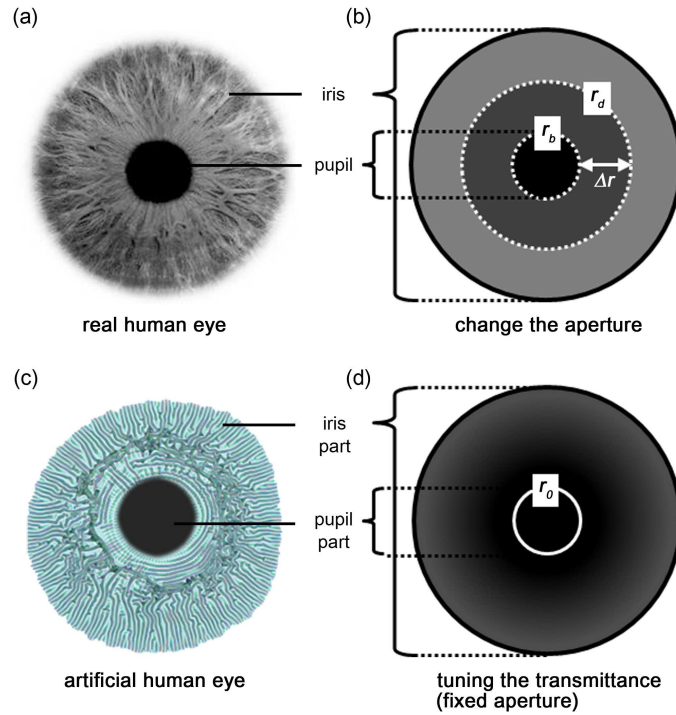


Figure 4.1: Anatomical comparisons between a real human eye and proposed artificial eye described from the plane view. (a) An optical micrograph of real human eye. (b) An operation principle of human eye. Human eye change the aperture so that regulate the amount of light incident to the retina. Here, radius of pupil is r_d at the dark state and one is r_b at the bright state, this state can be changed, reversibly. (c) An optical micrograph of proposed artificial eye. The artificial eye consists of pupil part and iris part as real human eye. (d) The iris part of artificial eye can be self-regulation of the transmittance by photoreaction and radius of pupil r_0 is fixed.

eye [97]. If the ambient light intensity is high, the iris reduced their aperture to r_b so that reduce the amount of light incident to the retina. On the other hand, the iris enlarges their aperture as r_d if the ambient light intensity is

low. Thus, the iris regulates the amount of light by controlling the radius (Δr) of the pupil. The proposed artificial iris is depicted in Fig. 4.1(c). The proposed artificial iris consists of two concentric circles like a donut shape and it has spoke pattern between two concentric circles as radial muscles of human eye. Although proposed artificial eye fixed (r_0) pupil part, iris part itself can be changed transmittance to regulate the amount of light incident using a photo-reactive material as shown in Fig. 4.1(d). Moreover, there is no need additional control circuit, such as an optical sensor and battery.

4.2 Photoreaction Process of Photochromic Dyes

As mentioned above, proposed artificial iris achieves the regulation of light incident through the change in the transmission of the photo-reactive materials. In our case, families of the spiropyrans were used as the photo-reactive dyes [98, 99]. The spiro form of an oxazine is a colorless dye. The conjugated system of the oxazine and another aromatic part of the molecule is separated by a sp^3 hybridized spiro carbon. After light irradiation, the bond between the spiro carbon and the oxazine breaks which eventually lead to sp^2 hybridization and its π -orbitals with the rest of the molecule, and a conjugated system forms with ability to absorb photons of visible light, and therefore appear color. When the light source is removed, the molecules relax to their ground state, the carbon-oxygen bond reforms, the spiro carbon becomes sp^3 hybridized again, and the molecule returns to its colorless state. Figures 4.2(a)-(c) show the UV/visible absorption of

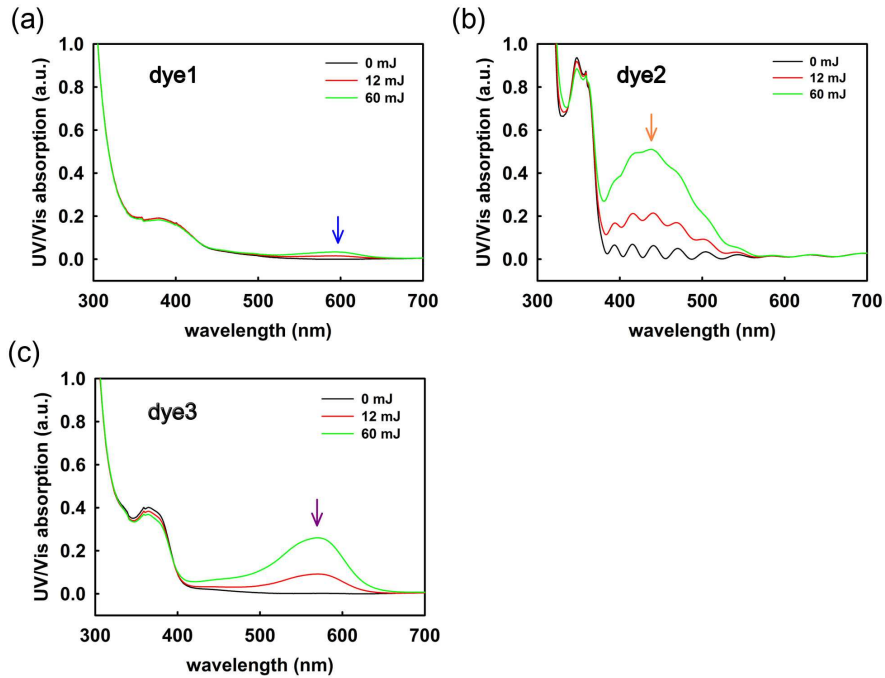


Figure 4.2: The UV/visible absorption spectra of the photo-reactive dyes for transmittance tuning. (a)-(c) The absorption properties of three different dye doped PMMA films with amount of incident light.

the different (dye1-3) photo-reactive dye doped poly(methyl methacrylate) (PMMA) films as a function of the light incident. These dye doped PMMA films were coated onto glass substrates. Each of the dyes used in the experiments was dissolved in PMMA at 6 % by weight. Note that the PMMA was chosen for its biocompatibility and optical transparency in the visible spectrum [100, 101]. The dye1 having an absorbance maximum at 595 nm (Fig. 4.2(a)), while the dye2 and the dye3 have an absorbance maximum at 455 nm (Fig. 4.2(b)) and 580 nm (Fig. 4.2(c)), respectively. Since the iris of human eye is blocked the light over a wide range of wavelength, these dyes cannot solely adopt the required properties of light blocking in our

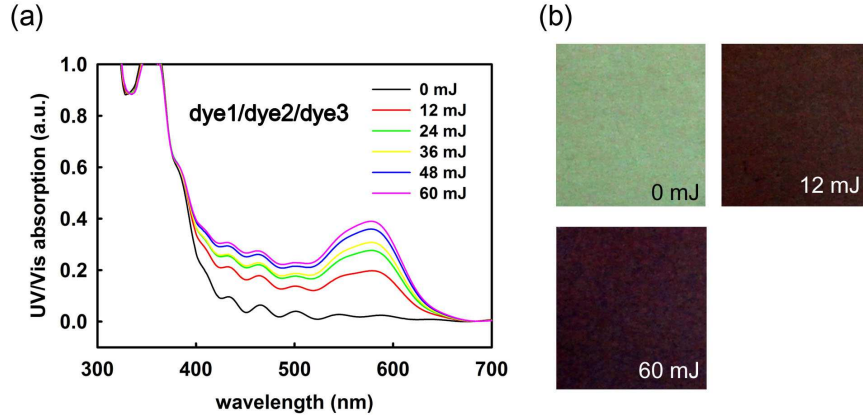


Figure 4.3: The UV/visible absorption spectra of the photo-reactive dyes for transmittance tuning. (a) The absorbance and (b) optical images of the blended dye composed of dye1, dye2, and dye3 in PMMA at 6 % by weight. artificial iris.

Figure 4.3(a) shows the the absorbance of the blended dye composed of dye1, dye2, and dye3 with ratio of 1 : 2 : 1 in PMMA at 6 % by weight. The blended dye blocked wider range of wavelength than each dye. Also, its absorption spectra can be changed by energy of incident light. Figure 4.3(b) show the microscopic images of the different (0, 12, and 60 mJ) light energy. As shown in images, transmittance of dye doped PMMA film resulted in decrease of incident light energy.

We now describe that the transmittance of the blended dye compared to those of human eye as shown in Fig. 4.4. The profiles of transmittance were determined using sigmaplot, by fitting the transmittance to the following equation $T_n \sim e^{-kx}$, where T_n is the normalized transmittance $((T - T_0)/\Delta T)$, k is the constant of transmission rate and x is the light intensity. Here, T_0 denote the transmittance at 0 mW/cm² of incident light intensity.

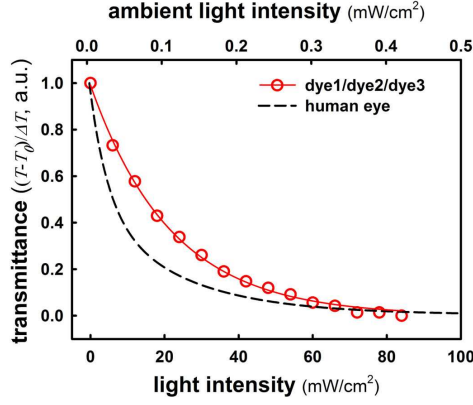


Figure 4.4: The normalized transmittance $((T - T_0)/\Delta T)$ of human eye and proposed material for artificial iris (blended dye doped PMMA film).

From the characterization of profiles, the k of human iris and photo-reactive dye are 0.248 and 0.137, respectively. Although there are differences of k , blended dye has similar transmission trend with human eye. Moreover, this little difference should be complemented by optimization of the material properties.

4.3 Fabrication Process of Spoke Pattern Formations

In light of the above idea, artificial iris is created in flexible substrate by a selective wetting inscription (SWI) process [102,103]. Fabrication process of proposed artificial iris is shown in Fig. 4.5. A commanding layer (CL) of a hydrophobic material (DS-1120F; Harves Co., Ltd.) is first formed on a substrate. Selective-wetting regions are generated through a predefined

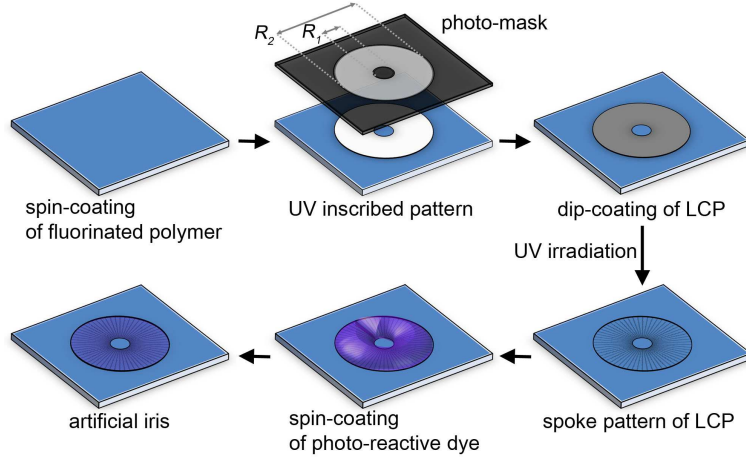


Figure 4.5: Schematic illustration of each step of the fabrication process of proposed artificial iris using UV inscription.

photo-mask by the UV assisted SWI on the CL. Here, R_1 and R_2 are 4 mm and 11 mm for simulate pupil and iris of human eye, respectively. The donut shape (concentric circles) pattern of the LCP is then spontaneously formed only in the wetting regions on the inscribed CL by simple dip-coating in solution of the LCP. The selective wetted LCP subsequently irradiated with the UV light. Note that, the spoke pattern of the interior of the LCP, consisting mainly of the radial wrinkles, correlated with the circular edges of initial wetting regions after dip-coating of LCP [104]. After spoke pattern forming, the dye doped PMMA is spin-coated on the substrate, followed by the thermal treatment (10 min. at 100 °C) for curing of the PMMA layer. Figure 4.6(a) shows the condition of the UV intensity and exposure time for the wrinkling pattern formation. The critical intensity and exposure time of UV is denoted by region of red color at which a wrinkling pattern formation. Microscopic images are correspond to Fig. 4.6(b) the wrinkled surface

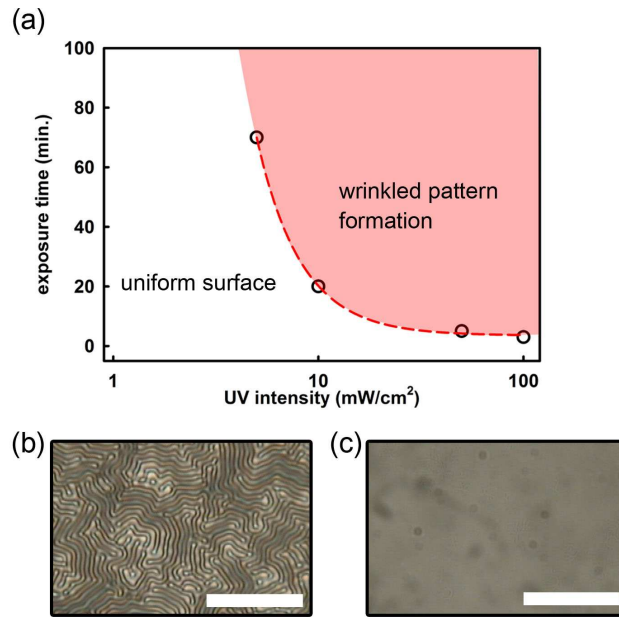


Figure 4.6: (a) The condition of the UV intensity and exposure time for the wrinkling pattern formation. The critical intensity and exposure time of UV is denoted by region of red color at which a wrinkling pattern formation. Microscopic images of right side correspond to (b) the wrinkled surface and (c) the uniform surface. The scale bar is $30 \mu\text{m}$.

(50 mW/cm^2 in 3 min.) and Fig. 4.6(c) the uniform surface (5 mW/cm^2 in 30 min.). We used the liquefied LCP (RMS03-001C, Merck Ltd.) based on multifunctional acrylate monomers for spoke pattern formation. Unsaturated bonds of the multifunctional acrylate monomers are activated by the photo-initiator of the LCP solution under the UV exposure [105, 106]. Upon curing, the liquid LCP layer develops a depth-wise gradient in degree of cross-linking or solidification, and in physical properties, such as diffusivity, modulus. The LCP film starts developing a modulus. The top LCP layer being most cured develops a modulus first and behaves like a solid skin,

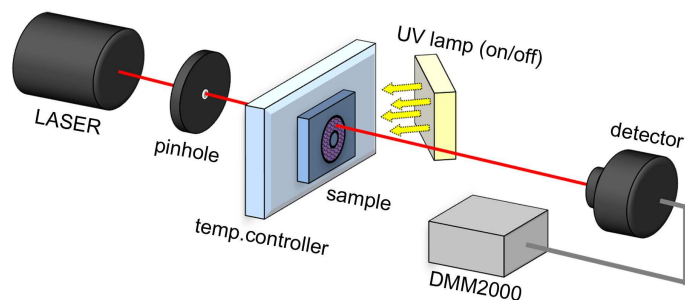


Figure 4.7: The experimental setup to measure the transmittance of the artificial iris using a controllable UV lamp. The artificial iris sample is placed in a temperature control system.

which is capable of supporting stresses. Moreover, the edges of the LCP film appear to solidify first and thereby anchor the skin to the substrate. The strength and thickness of the skin depends on curing conditions. Finally, when the film is not able to withstand the stress, the skin relieves stresses by out of plane deformation to produce wrinkles. Note that, intensity of UV light gets attenuated with thickness due to absorption of the LCP film. Reduced radiation level decreases the photo-initiator activation in the LCP film near the substrate, causing the LCP film near the substrate to cure at a slower rate compared to the top surface. Moreover, in the liquid LCP containing solvents, solvent depletion near the surface increases the reactant concentration there, and thereby enhances the rate of cure and promotes the depth-wise gradient in solidification further [105].

4.4 Self-Regulation of Light Intensity

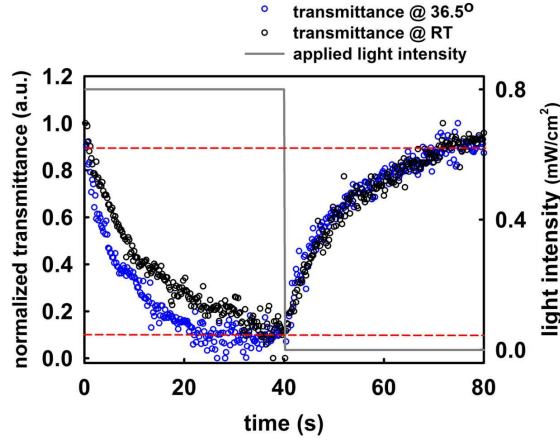


Figure 4.8: The dynamic response of our artificial iris under a UV light exposure at 0.8 mW/cm^2 .

We now discuss the optical properties of the artificial iris in the presence of light exposure. A simple optical setup for measuring the transmittance through the artificial iris is illustrated in Fig. 4.7. The rate of change in light intensity of artificial iris was performed by using the light source of UV lamp ($\lambda=365 \text{ nm}$) and it is examined with a He-Ne laser of 632.8 nm through the pinhole. Also, the sample of artificial iris was mounted on a temperature controller (central processor of Mettler Toledo FP90 with hot stage of FP82HT) to examine the temperature dependence.

First of all, the modulated transmittance in response to the light source intensity is shown in Fig. 4.8. The gray solid line and opened circles represent the applied light source and the dynamic light response of artificial iris, respectively. It was found that the response of dark-to-bright (r_b) and the response of bright-to-dark (r_d) are 25 ± 5 and 35 ± 5 s, respectively. Accordingly, the artificial iris regulates the light by itself within few ten

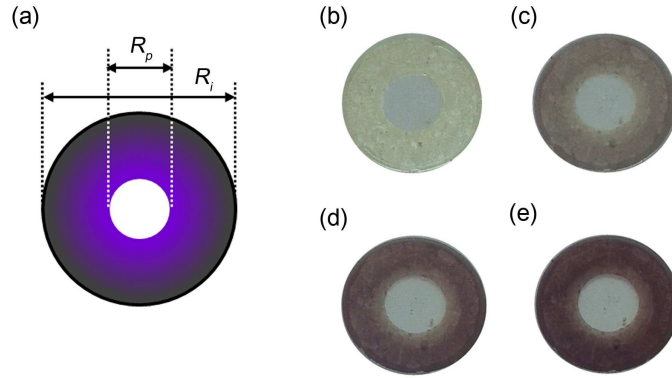


Figure 4.9: (a) Schematic diagram of fabricated artificial iris. Here, R_i and R_p represented diameter of iris and that of pupil, respectively. (b)-(e) Photographic images of artificial iris in the presence of an applied UV light of 0, 5, 30, and 60 mJ, respectively.

seconds. It should be noted that a few ten seconds of the measured switching speed are not suitable for replacement of human iris at this point in time. However, responsiveness of photo-reactive dyes will be improved by material optimization [107]. It may be interesting to note that spiro carbon also excite thermally and thus the r_b at body temperature (36.5°C) is relatively faster than at room temperature. Figure 4.9(a) depicts the structure of fabricated artificial eye and R_p (~ 4 mm) and R_i (~ 11 mm) represent radius of pupil and iris. Particularly, R_p reflected in pupil size of human eye in bright. Photographic images of the artificial iris in Figs. 4.9(b)-(e) were observed at different intensity of radiation. In the absence (0 mJ) of a light source, the photo-reactive dye remained optically transparent state. Thus, almost light propagate to retina. At 10 mJ, the transmission slightly reduced due to the increasing of absorption of photo-reactive dye. At 20 mJ, the transmission further reduced. At a relatively high energy of 40 mJ,

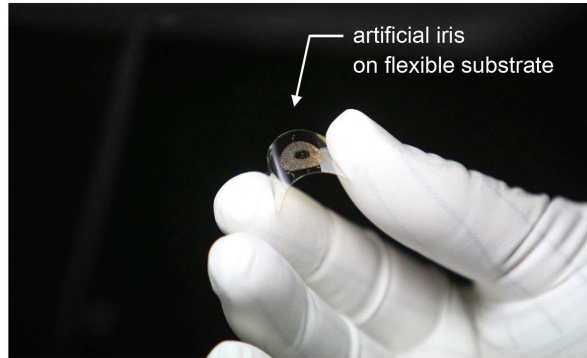


Figure 4.10: A photographic image of artificial iris fabricated on a flexible substrate.

most of visible light is absorbed into the layer of dye doped PMMA layer and a bright state (low transmittance) was obtained.

Finally, we now describe the applicability of the artificial iris on plastic substrates such as polyethersulphone (PES) for prosthetic iris implantation. The artificial iris was fabricated on the PES substrate by simultaneously forming all the polymer layers produced through the UV assisted SWI technique as mentioned above. The artificial iris has the dimension that of the radius of pupil (R_p) and the radius of pupil (R_i) are 4 mm and 11 mm, respectively. Figure 4.10 shows a photographic image of artificial iris fabricated on the PES substrate (2 cm \times 3 cm in size) in bent environment. Neither delamination of spoke pattern of the LCP and/or dye doped PMMA layers nor deterioration of the light responsiveness of the artificial iris was observed under a bent state with the curvature radius of a few centimeters.

4.5 Summary

In conclusion, the photoreaction approach presented herein provides a unique concept to design self-regulation artificial iris with a pseudo spoke pattern formation. This approach within the framework of transmission modulation of photo-reactive polymer requires neither additional operation circuit nor complicated fabrication process. It should be directly applicable for prosthetic iris implantation [89–92] or humanoid robotics.

Chapter 5

Concluding Remarks

In this thesis, electro-optic device based on polymeric materials with ordered interfaces produced by the surface treatments are studied in the viewpoints of the scientific researches and devices applications. The surface-induced ordering effects of the polymeric materials are numerically and analytically investigated. Also, the novel concepts of the artificial human iris and their application proposed and practically demonstrated. In Chap. 1, the various functional polymer and their physicochemical properties and patterning techniques for polymer materials were briefly introduced. Especially, the liquid crystalline polymer (LCP) is given a full explanation because it has unique physical and optical properties such as amphiphilic and birefringence. The motivation, patterning problem of functional polymer for application, of this research was also introduced in this chapter. In Chap. 2, the novel concepts of spontaneous pattern formation processes in liquid crystalline polymer (LCP) films through utilizing surface modifications such as a plasma treatment and an UV irradiation was introduced. The proposed methods enable the spontaneous pattern formation of well aligned one- or

two- dimensionally periodic micro-structures over large area, without additional template or patterning steps.

For advanced electro-optic (EO) applications, we demonstrated three types of novel EO devices using functional polymers, including ferroelectric liquid crystal (FLC) device with confined structure, symmetric-viewing display with alternating alignment layer, and convertible LC lens for 2D/3D convertible display in Chap. 3. In case of confined FLC, we report a continuous linear electro-optic effect associated with the smectic layer tilt and molecular order in a tight-pitch FLC confined between lateral walls in a vertically aligned configuration. In the topographic confinement by the lateral walls, two orthogonal anchoring forces exerted on the FLC result in the continuity of the smectic layer tilt as well as the molecular order without defects. The observed electro-optic effect should be directly applicable for fast electro-optic devices with a high subthreshold slope and a low operation voltage. Next, we demonstrated a symmetric-viewing inverse twisted nematic LCD (ITN-LCD) with four domains due to two alternating alignment layers produced via stamping assisted rubbing (SAR). With the help of an inert protective layer of a fluorinated acrylate polymer, the second rubbing process was successfully employed without causing any mechanical and chemical damage to the first rubbed alignment layer. The ITN-LC cell with four domains presented here showed continuous gray scales with good linearity as well as the symmetric-viewing characteristics that are needed for high image quality. Third, we demonstrated that a delicate interplay between the in-plane and out-of plane components of an inhomogeneous electric field plays a critical role on the flat-to-lenticular lens conversion in a homogeneously aligned LC cell. The framework of the refractive index-

matching between the lenticular cast and the planarization material layer provides a practical route to construction of a variety of electrically tunable, convertible LC devices in a planar geometry. Finally, our concept of using the electric field modulation on a flat surface should be directly applicable for constructing 2D/3D convertible displays and optical focusing elements in photonics.

In Chap. 4, biomimetic application of artificial iris was demonstrated. We present a concept of artificial iris that provides a self-regulation of light intensity without peripheral devices. Also, spoke pattern formation like radial muscles of human eye where an LCP is used as an anisotropic (radially) patterned material. The artificial iris is anatomically as well as functionally close to human eyes with unique regulation mechanism. This mechanism achieved analogy and concurrent control of the amount of light. The amount of light to the retina, associated with the photoreaction, is reversibly controlled through molecular bond reformation with irradiation of light source.

In conclusion, throughout this thesis, advanced EO devices and biomimetic application using various functional polymers have been explored from the viewpoints of scientific researches and practical applications. Especially, micro wrinkling pattern formation which is a matter of concern in biomimetic application was achieved by depth-wise gradient in solidification of liquid crystalline polymer. This wrinkling pattern formation is expected to have significant impact on micro patterning technique and surface modification areas. Moreover, researches on the new functional polymers and new device geometries are highly expected to provide a foundation for realizing the electro-optic applications.

Bibliography

- [1] D. J. Broer, J. Boven, G. N. Mol, and G. Challa, *Makromol. Chem.*, **190**, 2255 (1989).
- [2] D. J. Broer, R. A. M. Hikmet, and G. Challa, *Makromol. Chem.*, **190**, 3201 (1989).
- [3] J. Lub, D. J. Broer, R. A. M. Hikmet, and K. G. J. Nierop, *Liq. Cryst.*, **18**, 319 (1995).
- [4] D. J. Broer, G. P. Crawford, and S. Zumer, *Cross-Linked Liquid Crystalline Systems*, CRC Press, New York (2011).
- [5] K. K. Kobayashi, *J. Phys. Soc. Jpn.*, **29**, 101 (1970).
- [6] P. J. Collings, *Liquid Crystals*, IOP Publishing Ltd., (1990).
- [7] C. B. McArdle, *Side Chain Liquid Crystal Polymers*, Chapman and Hall, New York (1989).
- [8] V. Shibaev, *Polymers as Electrooptical and Photooptical Active Media*, Springer, Heidelberg (1996).
- [9] J.-H. Na, S. C. Park, S.-U. Kim, Y. Choi, and S.-D. Lee, *Opt. Express*, **20**, 864 (2012).

- [10] J.-H. Na, H. Li, S. C. Park, and S.-D. Lee, *Journal of Information Display*, **12**, 191 (2011).
- [11] J.-H. Na, S.-M. Cho, S.-D. Lee, and Y.-W. Lim, *Journal of Information Display*, **12**, 11 (2011).
- [12] Data sheet of NOA65 provided by Norland Products (<https://www.norlandprod.com>).
- [13] R. J. Plunkett, U.S. Pat. US 2230654.
- [14] R. E. Johnson Jr. and R. H. Dettre, and J. C. Berg, *Wettability*, Marcel Dekker, New York (1993).
- [15] W. A. Zisman, *Advances in Chemistry Series 43*, Am. Chem. Soc., Washington DC (1964).
- [16] J. Genzer, E. Sivaniah, E. J. Kramer, J. Wang, H. Korner, M. Xiang, K. Char, C. K. Ober, B. M. DeKoven, R. A. Bubeck, M. K. Chaudhury, S. Sambasivan, and D. A. Fischer, *Macromolecules*, **33**, 1882 (2000).
- [17] S. Y. Chou, P. R. Krauss, P. J. Renstrom, *Science*, **272**, 85 (1996).
- [18] J.-H. Choi, K.-H. Kim, S.-J. Choi, and H. H. Lee, *Nanotechnology*, **17**, 2246 (2006).
- [19] Y. Xia and G. M. Whitesides, *Annu. Rev. Mater. Sci.*, **28**, 153 (1998).
- [20] E. Cerda and L. Mahadevan, *Phys. Rev. Lett.*, **90**, 074302 (2003).
- [21] J. Genzer and J. Groenewold, *Soft Matter*, **2**, 310 (2006).

- [22] A. Schweikart and A. Fery, *Microchim. Acta*, **165**, 249 (2009).
- [23] X. Chen and J. Yin, *Soft Matter*, **6**, 5667 (2010).
- [24] Y. Sun, W. M. Choi, H. Jiang, and J. A. Rogers, *Nat. Nanotechnol.*, **1**, 201 (2006).
- [25] E. P. Chan, E. Smith, R. Hayward, and A. J. Crosby, *Adv. Mater.*, **20**, 711 (2008).
- [26] B. Kolaric, K. Branko, H. Vandeparre, S. Desprez, R. A. L. Vallee, and P. Damman, *Appl. Phys. Lett.*, **96**,043119 (2010).
- [27] W. H. Koo, S. M. Jeong, F. Araoka, K. Ishikawa, S. Nishimura, T. Toyooka, and H. Takezoe, *Nat. Photon.*, **4**, 222 (2010).
- [28] P. C. Lin and S. Yang, *Soft Matter*, **5**, 1011 (2009).
- [29] A. D. Stroock and G. M. Whitesides, *Acc. Chem. Res.*, **36**, 597 (2003).
- [30] M. T. Lam, W. C. Clem, and S. Takayama, *Biomaterials*, **29**, 1705 (2008).
- [31] C. M. Stafford, *Nat. Mater.*, **3**, 545 (2004).
- [32] N. Bowden, W. T. S. Huck, K. E. Paul, and G. M. Whitesides, *Appl. Phys. Lett.*, **75**, 2557 (1999).
- [33] D. K. Yi, M. J. Kim, L. Turner, K. S. Breuer, and D. Y. Kim, *Biotechnol. Lett.*, **28**, 169 (2006).
- [34] D. K. Yi, M. J. Kim, and D.-Y. Kim, *Langmuir*, **18**, 2019 (2002).

- [35] S. Patel, K. Kurpinski, R. Quigley, H. Gao, B. S. Hsiao, M. M. Poo, and S. Li, *Nano Lett.*, **7**, 2122 (2007).
- [36] K. Lee, S. Park, C. Mirkin, J. Smith, and M. Mrksich, *Science*, **295**, 1702 (2002).
- [37] E. K. Yim, R. M. Reano, S. W. Pang, A. F. Yee, C. S. Chen, and K. W. Leong, *Biomaterials*, **26**, 5405 (2005).
- [38] C.-J. Baek, S.-H. Hyun, S.-K. Lee, H.-J. Seol, H.-I. Kim, and Y. H. Kwon *Dent. Mater. J.*, **27**, 523 (2008).
- [39] H. Lei, L. F. Francis, W. W. Gerberich, L. E. Scriyen, *AIChE J.*, **48**, 437 (2002).
- [40] Data sheet of RMS03-001C provided by Merck Ltd.
- [41] K. Koo, J.-H. Na, Y.-T. Kim, H. Li, and S.-D. Lee, *Journal of Information Display*, **10**, 180 (2009).
- [42] S. Wu *Polymer Interface and Adhesion*, Marcel Dekker, Boca Raton, pp 96-104 (1982).
- [43] Z. Wang, J. Zhang, R. Xing, J. Yuan, D. Yan, and Y Han, *J. Am. Chem. Soc.*, **125**, 15278 (2003).
- [44] W. Choi, Ph.D Thesis (2011).
- [45] M. E. Becker, R. A. Kilian, B. Kosmowski, and D. A. Mlynski, *Mol. Cryst. Liq. Cryst.*, **132**, 167 (1986).
- [46] F. C. Franck, *Discuss. Faraday Soc.*, **25**, 19 (1958).

- [47] J. Nehring and A. Saupe, *J. Chem. Soc., Faraday Trans. 2*, **68**, 1 (1972).
- [48] B. A. Wood and E. L. Thomas, *Nature*, **324**, 655 (1986).
- [49] S. Zhang, E. M. Terentjev, and A. M. Donald, *J. Phys. Chem. B*, **109**, 13195 (2005).
- [50] P. G. De Gennes and P. Prost, *The Physics of Liquid Crystals*, Oxford (1993).
- [51] W. H. Song, I. A. Kinlock, and A. H. Windle, *Science*, **302**, 1363 (2003).
- [52] K. Dholakia and T. Cizmar, *Nat. Photon.* **5**, 335 (2011).
- [53] J.-H. Na, H. Pae, J. Kim, C.-J. Yu, and S.-D. Lee, *Jpn. J. Appl. Phys.*, **50**, 034101 (2011).
- [54] M. C. Choi, T. Pfohl, Z. Wen, Y. Li, M. W. Kim, J. N. Israelachvili, and C. R. Safinya, *Proc. Natl Acad. Sci. USA*, **101**, 17340 (2004).
- [55] D. K. Yoon, M. C. Choi, Y. H. Kim, M. W. Kim, O. D. Lavrentovich, and H.-T. Jung, *Nat. Mater.*, **6**, 866 (2007).
- [56] G. McKay, *J. Non-Newtonian Fluid Mech.*, **119**, 115 (2002).
- [57] Y. Xia and G. M. Whitesides, *Angew. Chem., Int. Ed.*, **37**, 550 (1998).
- [58] Y.-T. Kim, J.-H. Hong, T.-Y. Yoon, and S.-D. Lee, *Appl. Phys. Lett.*, **88**, 263501 (2006).

- [59] Data sheet of FLC-10855 provided by Rolic Technologies Ltd. (Allschwil, Switzerland).
- [60] D. K. Yoon, M. C. Choi, Y. H. Kim, M. W. Kim, O. D. Lavrentovich, and H.-T. Jung, *Nat. Mater.*, **6**, 866 (2007).
- [61] P. Rudquist, J. P. F. Lagerwall, M. Buivydas, F. Gouda, S. T. Lagerwall, N. A. Clark, J. E. Maclennan, R. Shao, D. A. Coleman, S. Bardon, T. Bellini, D. R. Link, G. Natale, M. A. Glaser, D. M. Walba, M. D. Wand, and X.-H. Chen, *J. Mater. Chem.*, **9**, 1257 (1999).
- [62] H. Yokoyama, S. Kobayashi, and H. Kamei, *Appl. Phys. Lett.* **41**, 438 (1982).
- [63] G. McKay and K. R. MacKenzie, *Ferroelectrics*, **277**, 107 (2002).
- [64] K. Kaneko, *J. Membrane Sci.*, **96**, 59 (1994).
- [65] R. E. Geer, S. J. Singer, J. V. Selinger, B. R. Ratna, and R. Shashidhar, *Phys. Rev. E.*, **57**, 3059 (1998).
- [66] P. J. Barratt and B. R. Duffy, *Liq. Cryst.*, **23**, 525 (1997).
- [67] A. M. Lowe, B. H. Ozer, Y. Bai, P. J. Bertics, and N. L. Abbott, *ACS Appl. Mater. Interfaces.*, **2**, 722 (2010).
- [68] J.-H. Lee, D.-W. Kim, Y.-H. Wu, C.-J. Yu, S.-D. Lee, and S.-T. Wu, *Opt. Express*, **13**, 7732 (2005).
- [69] D.-W. Kim, C.-J. Yu, Y.-W. Lim, J.-H. Na, and S.-D. Lee, *Appl. Phys. Lett.*, **87**, 051917 (2005).

- [70] S.-W. Suh, S.T. Shin, and S.-D. Lee, *Mol. Cryst. Liq. Cryst.*, **302**, 163 (1997).
- [71] S.-W. Suh, S.T. Shin, and S.-D. Lee, *Appl. Phys. Lett.*, **68**, 2819 (1996).
- [72] Y.-J. Na, S.-W. Lee, W. Choi, S.-J. Kim, and S.-D. Lee, *Adv. Mater.*, **21**, 537 (2009).
- [73] M. Schadt, H. Seiberle, and A. Schuster, *Nature*, **381**, 212 (1996).
- [74] J. Cognard, *Alignment of Nematic Liquid Crystals and Their Mixtures*, Gordon and Breach, London, (1982).
- [75] B. Wang, M. Ye, M. Honma, T. Nose, and S. Sato, *Jpn. J. Appl. Phys.*, **41**, L1232 (2002).
- [76] H. Ren, Y.-H. Fan, S. Gauza, and S.T. Wu, *Appl. Phys. Lett.*, **84**, 4789 (2004).
- [77] B. Wang, M. Ye, and S. Sato, *Mol. Cryst. Liq. Cryst.*, **413**, 423 (2004).
- [78] W. Choi, D.-W. Kim, and S.-D. Lee, *Mol. Cryst. Liq. Cryst.*, **508**, 397 (2009).
- [79] Y.-Y. Kao, Y.-P. Huang, K.-X. Yang, P. C.-P. Chao, C.-C. Tsai, and C.-N. Mo, in *Proceedings of SID Symp. Dig.*, **40**, 111 (2009).
- [80] M. Sluijter, A. Herzog, D. K. G. de Boer, M. P. C. M Krijn, and H. P. Urbach, *J. Opt. Soc. Am. B*, **26**, 2035 (2009).

- [81] J.-H. Na, S. C. Park, S.-U. Kim, and S.-D. Lee, in Proceedings of SID Symp. Dig., **42**, 1584 (2011).
- [82] Y. Choi, J.-H. Park, J.-H. Kim, and S.-D. Lee, Opt. Mater., **21**, 643 (2002).
- [83] Y.-H. Lin, H. Ren, K.-H. Fan-Chiang, W.-K. Choi, S. Gauza, X. Zhu, and S.-T. Wu, Jpn. J. Appl. Phys., **44**, 243 (2005).
- [84] Y. Choi, H.-R. Kim, K.-H. Lee, Y.-M. Lee, and J.-H. Kim, Appl. Phys. Lett., **91**, 221113 (2007).
- [85] J. Lee, S.-W. Suh, K. Lee, and S.-D. Lee, Phys. Rev. E, **49**, 923 (1994).
- [86] P. G. deGennes and J. Prost, *The Physics of Liquid Crystals, 2nd ed.*, Oxford University Press, New York, (1993).
- [87] Data sheet of ZLI-4151-000 provided by Merck Ltd.
- [88] G. Barero, L. R. Evangelista, and N. V Madhusudana, Eur. Phys. J. B, **1**, 327 (1998).
- [89] D. Sakellaris, C. Goossens, M. J. Tassignon, Eur. J. Ophthalmol., **19**, 1084 (2009).
- [90] C. Abela-Formanek, M. Amon, G. Kahraman, J. Schauersberger, R. Dunavoelgyi, J. Cataract. Refract. Surg., **37**, 104 (2011).
- [91] W. E. Sponsel, Clin. Exp. Ophthalmol., **37**, 831 (2009).
- [92] W. Ayliffe, S. L. Groth and W. E. Sponsel, J. Cataract. Refract. Surg., **38**, 362 (2012).

- [93] T.-C. Hsu, C.-H. Lu, Y.-T. Huang, W.-P. Shih, and W.-S. Chen, *Sens. Actuators A: Phys.*, **169**, 341 (2011).
- [94] J. Lapointe, J.-F. Durette, A. Harhira, A. Shaat, P. R. Boulos, and R. Kashyap, *Eye*, **24**, 1716 (2010).
- [95] C. W. Oyster, *The human eye: structure and function*, Sinauer Associates Inc., Sunderland MA (1999).
- [96] L. A. Remington, *Clinical anatomy and physiology of the visual system*, Elsevier Inc., St. Louis MO (2012).
- [97] D. A. Atchison and G. Smith, *Optics of the human eye*, Elsevier Science Ltd., Edinbergh (2003).
- [98] G. K. Such, R. A. Evans, and T. P. Davis, *Macromolecules*, **39**, 1391 (2006).
- [99] B. Seefeldt, R. Kasper, M. Beining, J. Mattay, J. Arden-Jacob, N. Kemnitzer, K. H. Drexhage, M. Heilemanna, and M. Sauer, *Photochem. Photobiol. Sci.*, **9**, 213 (2010).
- [100] K. Pal, A. K. Banthia, and D. K. Majumdar, *Designed Monomers Polymers*, **12**, 197 (2009).
- [101] L. Billon, M. Manguian, V. Pellerin, M. Joubert, O. Eterradosi, and H. Garay, *Macromolecules*, **42**, 345 (2009).
- [102] Y.-J. Na, S.-W. Lee, W. Choi, S.-J. Kim, and S.-D. Lee, *Adv. Mater.*, **21**, 537 (2009).

- [103] J.-H. Hong, J.-H. Na, H. Li, and S.-D. Lee, *Journal of Information Display*, **11**, 140 (2010).
- [104] K.-H. Lee, S.-M. Kim, H. Jeong, and G.-Y. Jung, *Soft Matter*, **8**, 465 (2012).
- [105] J. A. Payne, L. F. Francis, and A. V. McCormick, *J. Appl. Polym. Sci*, **66**, 1267 (1997).
- [106] S. K. Basu, L. E. Scriven, L. F. Francis, and A. V. McCormick, *Prog. Org. Coat.*, **53**, 1 (2005).
- [107] R. A. Evans, T. L. Hanley, M. A. Skidmore, T. P. Davis, G. K. Such, L. H. Yee, G. E. Ball, and D. A. Lewis, *Nat. Mater.*, **4**, 249 (2005).

Publication

[1] International Papers

1. **J.-H. Na**, S. C. Park, and S.-D. Lee, "Biologically inspired artificial iris with self-regulation of light intensity by reversible photoreaction", *Soft Matter* (to be submitted).
2. **J.-H. Na**, Y. Choi, and S.-D. Lee, "Lateral wall-induced electro-optic effect from smectic layer tilt and molecular order in a tight-pitch ferroelectric liquid crystal", *Opt. Express* (to be submitted).
3. S. C. Park, **J.-H. Na**, and S.-D. Lee, "Colloidal particle-based surface nanotopography with high mechanical stability by thermal fixation for liquid crystal devices", *J. Appl. Phys.* **112**, 023104 (2012).
4. S. H. Kang, **J.-H. Na**, S. N. Moon, W. I. Lee, P. J. Yoo, and S.-D. Lee, "Self-organized anisotropic wrinkling of molecularly aligned liquid crystalline polymer", *Langmuir* **28**, 3576 (2012).
5. J. Kim, **J.-H. Na**, and S.-D. Lee, "Fully continuous liquid crystal diffraction grating with alternating semi-circular alignment by imprinting", *Opt. Express* **20**, 3034 (2012).

6. **J.-H. Na**, S. C. Park, S.-U. Kim, Y. Choi, and S.-D. Lee, "Physical mechanism for flat-to-lenticular lens conversion in homogeneous liquid crystal cell with periodically undulated electrode", *Opt. Express* **20**, 864 (2012).
7. **J.-H. Na**, H. Li, S. C. Park, and S.-D. Lee, "Symmetric-viewing liquid crystal display with alternating alignment layers in an inverse-twisted-nematic configuration", *Journal of Information Display* **12**, 191 (2011).
8. **J.-H. Na**, S.-M. Cho, S.-D. Lee, and Y.-W. Lim, "High brightness and wide-view transfective liquid crystal display with two in-cell imprinted optical films in an inverse-twisted-nematic geometry", *Journal of Information Display* **12**, 11 (2011).
9. **J.-H. Na**, H. Pae, J. Kim, C.-J. Yu, and S.-D. Lee, "A mean-field photoreaction model for the pretilt generation of a liquid crystal on photopolymer layers upon ultraviolet exposure", *Jap. J. Appl. Phys.* **50**, 34101 (2011).
10. J.-H. Hong, **J.-H. Na**, H. Li, and S.-D. Lee, "Fabrication of lateral and stacked color patterns through selective wettability for display applications", *Journal of Information Display* **11**, 140 (2010).
11. K. Koo, **J.-H. Na**, Y.-T. Kim, H. Li, and S.-D. Lee, "Stamping-assisted fabrication technique of the bidirectional alignment layer for wide-viewing twisted-nematic liquid crystal displays", *Journal of Information Display* **10**, 180 (2009).

12. D.-W. Kim, **J.-H. Na**, J.-H. Hong, and S.-D. Lee, "A fast transreflective ferroelectric liquid crystal display with gray scales in a single gap geometry with dual transverse electric field", *Jap. J. Appl. Phys.* **48**, 90204 (2009).
13. J.-H. Bae, W.-H. Kim, **J.-H. Na**, and S.-D. Lee, "Enhanced electrical properties of organic thin film transistors by the pentacene order on a photo-aligned polymeric insulator", *Mol. Cryst. Liq. Cryst.* **476**, 141 (2007).
14. **J.-H. Na**, J. Kim, W. Choi, J.-H. Bae, and S.-D. Lee, "Reduction in the threshold voltage of a polymer light-emitting diode by high molecular density on a photo-crosslinking layer", *Mol. Cryst. Liq. Cryst.* **476**, 125 (2007).
15. S. Baek, S. Roh, **J.-H. Na**, Y. Jeong, C. Jeong, S.-D. Lee, and B. Lee, "Liquid-crystal-cladding fiber bragg gratings with electrically controllable polarization-dependent characteristics", *Jap. J. Appl. Phys.* **45**, 4044 (2006).
16. D.-W. Kim, C.-J. Yu, Y.-W. Lim, **J.-H. Na**, and S.-D. Lee, "Mechanical stability of a flexible ferroelectric liquid crystal display with a periodic array of columnar spacers", *Appl. Phys. Lett.* **87**, 051917 (2005).

[2] Domestic Papers

1. S. Baek, S. Roh, **J.-H. Na**, J. Kwon, I. Yoon, S. Chung, C. Jeong, S.-D. Lee, and B. Lee, "Electrically controllable fiber bragg gratings with liquid crystal cladding", *J. Opt. Soc. Korea* **9**, 123 (2005).

[3] International Proceedings

1. J. Kim, **J.-H. Na**, and S.-D. Lee, "Continuous diffraction grating based on a nematic liquid crystal with semi-radial alignment for display applications" Proc. 11th Int'l Meeting Inf. Disp. (Korea Inf. Disp. Soc., Seoul, 2011) p. 786.
2. S. C. Park, **J.-H. Na**, and S.-D. Lee, "Wide-viewing vertically-aligned liquid crystal displays with surface microstructure formation using colloidal particles" Proc. 11th Int'l Meeting Inf. Disp. (Korea Inf. Disp. Soc., Seoul, 2011) p. 644.
3. J. Kim, **J.-H. Na**, and S.-D. Lee, "Graded-subdomain diffraction grating based on a nematic liquid crystal with semi-radial alignment", SPIE Optics and Photonics (SPIE, San Diego, 2011) 8114-08.
4. S. C. Park, **J.-H. Na**, and S.-D. Lee, "Immobilization of nanoparticles for fabrication of surface microstructures for wide-viewing liquid crystal displays", MRS Spring Meeting (Mater. Res. Soc., San Francisco, 2011) O9.6.
5. **J.-H. Na**, S. C. Park, S.-U. Kim, and S.-D. Lee, "Tunable lenticular lens array using liquid crystal on periodically undulated electrodes for autostereoscopic 2D/3D convertible displays", Tech. Digest 42th Soc. Inf. Display Int'l Sym. (Soc. Inf. Disp., Los Angeles, 2011) p. 1584.
6. **J.-H. Na**, J.-H. Hong, and S.-D. Lee, "Viewing angle enhancement of inverse twisted nematic liquid crystal Displays with four domains by alternating alignment technique", SPIE Photonic West (SPIE, San Francisco, 2011) 7955-29.

7. **J.-H. Na**, J.-H. Hong, and S.-D. Lee, "High speed displays with low operation voltage using pixel- confinement of a deformed helix ferroelectric liquid crystal in the vertically aligned geometry", SPIE Photonic West (SPIE, San Francisco, 2011) 7956B-23.
8. H. Li, **J.-H. Na**, and S.-D. Lee, "Wide-viewing liquid crystal display with imprinted alignment layer in a homeotropic configuration", KJF Int'l Conf. (Poly. Soc. Korea, Fukuoka, 2010) PB024.
9. Y.-T. Kim, J.-H. Hong, **J.-H. Na**, Y. Kim, B. Lee, and S.-D. Lee, "A Monolithic Elastomer Substrate with Lens Array for Three-Dimensional Liquid Crystal Displays", Tech. Digest 41th Soc. Inf. Display Int'l Sym. (Soc. Inf. Disp., Seattle, 2010) p. 946.
10. **J.-H. Na**, Y.-T. Kim, J.-H. Hong, K. Koo, and S.-D. Lee, "Wide-viewing twisted-nematic liquid crystal display using a stamping assisted rubbing process", Tech. Digest 41th Soc. Inf. Display Int'l Sym. (Soc. Inf. Disp., Seattle, 2010) p. 1735.
11. Y.-W. Lim, S.-M. Cho, **J.-H. Na**, and S.-D. Lee, "Wide-viewing transfective liquid crystal display with in-cell binary optical layer in an inverse twisted nematic geometry", The 14th Int'l Sym. Adv. Disp. Mater. Dev. (ADMRC, Daegu, 2010) Plenary Lecture.
12. **J.-H. Na**, C. Keum, Y.-J. Na, and S.-D. Lee, "A ferroelectric liquid crystal display with low operation voltage in a pixel-confined geometry", The 16th Int'l Disp. Workshop (Soc. Inf. Disp., Miyazaki, 2009) p. 1209.

13. **J.-H. Na**, D.-W. Kim, and S.-D. Lee, "High speed transfective ferroelectric liquid crystal display with gray scales in a vertically aligned configuration", Int'l Sym. Liq. Cryst. Sci. Tech. (Liq. Crys. Br. Chinese Phys. Soc., Kunming, 2009) ID063.

[4] **Domestic Proceedings**

1. S. H. Kang, **J.-H. Na**, S. N. Moon, and W. I. Lee, "Self-organized anisotropic wrinkle structures by plasma treatment of an aligned liquid crystalline polymer" 2010 Fall Conf. KSME (Korean Soc. Mech. Eng., 2010) p. 4236.
2. E. Jang, **J.-H. Na**, S.-M. Cho, and S.-D. Lee, "Polymer heterojunction photovoltaic device with a diffusive region by selective interpenetration", The 16th Korean Conf. Semicon. (Korean Phys. Soc., Daejeon, 2009) TF4-2.

국문 초록

고분자 물질과 이를 이용한 응용 소자들은 분자 공학의 발전과 다양한 표면 처리 기술의 진보에 힘입어 최근 많은 연구 분야에서 각광을 받고 있다. 고분자 물질은 기존의 무기성 물질에 비해 변형이 자유롭고, 공정이 단순하다. 또한 기능성 그룹과의 조합이 가능할 뿐만 아니라, 필름, 섬유 그리고 박막의 형태를 다양한 기판 위에 구현할 수 있는 장점을 지닌다.

본 논문에서는 이러한 기능성 고분자를 분자 단위로 정렬할 수 있는 다양한 표면 처리 기술을 바탕으로 분자 정렬의 물리적 해석뿐만 아니라 새로운 개념의 전기광학 및 생체 모방 소자로의 응용에 대해 고찰해 보고자 한다. 특히 비 등방성 고분자인 액정 고분자의 양친성과 자외선 및 플라즈마를 이용한 경화 공정을 이용하여 액정 분자의 정렬에 관하여 수치 해석 및 실험적으로 살펴보았다.

그 응용의 예로, 우선 3차원적으로 갇힌계에서 층상 구조를 갖는 강 유전성 액정의 거동에 대해서 살펴보았다. 일반적으로 강 유전성 액정의 층상 구조는 층간의 높이를 일정하게 유지하려는 경향을 갖는다. 하지만 본 연구에서처럼 구조적으로 갇힌계를 구현하였을 때, 강 유전성 액정은 갇힌계의 상/하 기판뿐만 아니라 측면에서 발생하는 표면 에너지에 의해서 층상 구조가 변형됨을 모델을 통해 관찰하였다. 또한 이렇게 변형된 강 유전성 액정은 높은 구동 전압이 요구되는 짧은 피치를 갖은 수직 배향 구

조임에도 불구하고, 낮은 구동 전압과 높은 광 효율 특성을 관찰할 수 있었다. 이는 고속의 응답 특성이 요구되는 전기 광학 소자 및 디스플레이에 응용될 수 있을 것으로 예상된다. 두 번째 전기광학 소자의 응용으로 균일한 시야 특성을 갖는 액정 디스플레이를 도장 배향 기술을 통해 구현하였다. 이 경우 시야각 향상을 위해 별도의 전극 패턴 및 돌기 형성이 필요 없이 넓은 시야 특성을 구현할 수 있다. 기본적으로 액정 디스플레이는 대비비가 우수한 인버스 트위스티드 네마틱 모드에 적용하였으며, 서로 다른 배향 방향을 교대로 한 기관에 구현함으로써 다중 배향 액정 도메인을 실현하였다. 즉, 우수한 시야 특성을 갖는 액정 디스플레이를 단순한 선택적 배향 공정을 통해 구현할 수 있었다. 마지막 전기 광학 소자의 응용의 예로 최근 각광을 받고 있는 3차원 디스플레이에 적용 가능한 초점 거리 변환 액정 렌즈를 구현하였다. 본 연구에서는 가변 액정 렌즈를 통해 2차원/3차원 영상을 필요에 따라 선택적으로 구현이 가능하도록 굴절률 매칭 기술을 도입하여, 인가전압 유/무에 따라 액정 방향자를 변환할 수 있도록 하였다. 이 때 기존의 수직 전기장 모드에서 간과되었던, 수평 전기장에 대한 물리적 고찰을 통해 수평 전기장이 유효 표면 에너지에 영향을 미친다는 점을 수치해석과 실험을 고찰해 보았다.

다음으로 액정 고분자의 비등방성 정렬 특성을 응용한 생체모방 소자의 응용에서 대해서 살펴보았다. 본 연구에서는 인간의 눈에서 입사 광량을 조절해 주는 홍채에 대해서 고찰해 보았다. 인간의 홍채는 홍채 주름으로 명명된 고유의 미세 패턴이 존재하는데, 이를 액정 고분자의 비 등방성 정렬 성질과 기관의 선택적 젖음성을 이용하여 구현하였다. 아울러 외부 광원에 따라 입사 광량 조절이 가능한 변색성 고분자를 함께 도입하여 기존의 물리적으로 입사 광량을 조절했던 방식과는 다르게 홍채 부분의 투과도를 조절하면서 광량을 조절하는 새로운 개념의 인공 홍채를 제안하였다.

결과적으로, 본 논문에서는 기능성 고분자를 바탕으로 이에 응용 가능한 표면 처리 기술을 적용하여 전기광학 및 생체모방 소자의 응용에 관한 연구를 진행하였다. 특히 기존에 구현이 어려웠던 고분자의 미세 패턴 형성을 비 등방성 고분자와 표면 처리 기술을 통해 다양한 형태로 구현할 수 있는 기술을 개발하였다. 또한 새로운 구조의 전기 공학 소자를 제안함으로써 고분자 기반의 전기광학분야에 초석을 제공할 수 있을 것으로 기대된다.

주요어: 기능성 고분자, 액정, 표면 주름, 표면 에너지, 배향 공정, 액정 렌즈, 인공홍채.

학 번: 2008-30873